Carbonatitic magma fractionation and contamination generate rare earth element enrichment and mineralization in the Maoniuping giant REE deposit, SW China

Xu Zheng[1,2], Yan Liu[2*], Martin P. Smith[3], Jindřich Kynický[4], Zengqian Hou[2]

1. State Key Laboratory of Geological Processes and Mineral Resources, China University of Geosciences, Beijing 100083, PR China

2. Institute of Geology, Chinese Academy of Geological Sciences, Beijing 100037, PR China

3. School of Environment and Technology, University of Brighton, Brighton BN24GJ, UK

4. Department of Geology and Pedology, Mendel University, Brno 361300, Czech Republic

Corresponding author: Yan Liu E-mail address: ly@cags.ac.cn

Submit to: Journal of Petrology

ABSTRACT

Carbonatite intrusions host the world's most important light rare earth element (LREE) deposits, and their formation generally requires extraordinary fertile sources, magmatic evolution, and hydrothermal events. However, carbonatitic magma evolution, particularly the role of fractional crystallization and contamination from silicate rocks in REE enrichment, remains enigmatic. The Maoniuping world-class REE deposit in southwestern China, is an ideal target to decipher magmatic evolution and related REE enrichment as it shows continuous textual evolution from medium- to coarse-grained calcite carbonatite (carbonatite I) at depth, to progressively pegmatoidal calcite carbonatite (carbonatite II) at shallow levels. In both types of calcite carbonatites, four generations of calcite can be classified according to petrographic and geochemical characteristics. Early-crystalizing calcite (Cal-I and Cal-II) are found in carbonatite I and exhibit equigranular and a polygonal mosaic textures, while late calcites (Cal-III and Cal-IV) in carbonatite II are large-size oikocrysts (>0.5 mm in length) with strain-induced undulatory extinction and bent twinning lamellae. All these generations of calcite yield similar, near-chondritic, Y/Ho ratios (26.6−28.1) and are inferred to be of magmatic origin. Remarkably, gradual enrichment of MgO, FeO and MnO from Cal-I to Cal-IV is coupled with a significant increase in REE contents (~800 to 2000 ppm), with LREE-rich and gentle-to-steep chondrite-normalized REE patterns ($(La/Yb)_N$ = 3.1–26.8 and $(La/Sm)_N$ = 0.9–3.9, respectively). Such significant REE enrichment is ascribed to protracted magma

fractional crystallization with initial low degree of fractional crystallization (fraction of melt remining (F) = ~0.95) evolving to late stage (F = 0.5–0.6) by formation of abundant calcite cumulates. Differential LREE and HREE behavior during magma evolution largely depend on separation of phlogopite, amphibole, and clinopyroxene from the carbonatitic melt, which is indicated by progressively elevated $(La/Yb)_N$ ratios ranging from 3.1 to 26.8. The four generations of calcite have significantly different C and Sr isotopic compositions with $\delta^{13}C_{V\text{-}PDB}$ decreasing from –3.28 to –9.97 ‰ and $^{87}Sr/^{86}Sr$ increasing from 0.70613 to 0.70670. According to spatial relations and petrographic observations, the relative enrichment of $\delta^{13}C$ and depletion in $^{87}Sr/^{86}Sr$ ratios of Cal-I and Cal-II show primary isotopic characteristics inherited from initial carbonatitic magma. By contrast, the variable Sr and C isotopic compositions of Cal-III and Cal-IV are interpreted as the results of contamination by components derived from silicate wall rocks and loss of CO_2 by decarbonation reactions. To model such contamination processes, Raleigh volatilization and Monte Carlo simulation have been invoked and the model results reveal that carbonatitic melt-wall rock interaction requires 40% radiogenic Sr contamination from silicate rocks and 35% CO_2 degassing from carbonatitic melt. Moreover, positive correlations between decreasing $\delta^{13}C$ values and increasing REE contents, together with bastnäsite-(Ce) precipitation, indicate further REE accumulation during the contamination processes. In summary, alongside REE-rich magma sources, the extent of fractional crystallization and contamination during carbonatitic magma evolution

are inferred to be important mechanisms in terms of REE enrichment and mineralization in carbonatite-related REE deposits worldwide.

Keywords: calcite carbonatite; fractional crystallization of carbonatitic magma; wall-rock contamination; Sr-C isotopic decoupling; REE enrichment and mineralization

INTRODUCTION

Rare earth elements (REEs) are essential raw materials for aerospace, permanent magnets, electric vehicles and renewable energy generation as part of the group of so-called critical metals (Chakhmouradian & Wall, 2012; Linnen et al., 2014; Wall &Pell, 2020). Carbonatite-related REE deposits are the world's most important source of LREEs and host approximately 51.4% of global rare earth oxides (REO) resources (Weng et al., 2015). An increasing body of research indicates that the genesis of carbonatite-related REE deposits is not the product of a simple one-stage process, but involved a sequence of extraordinary REE enrichment in metasomatic mantle sources followed by magmatic to hydrothermal evolution (e.g., Bayan Obo, China, Smith & Henderson, 2000; Smith et al., 2007, 2015; Yang et al., 2019; Wei et al., 2022; Mountain Pass, USA, Castor, 2008; Poletti et al., 2016; Maoniuping, China, Hou et al., 2006, 2015; Liu et al., 2019a, b; Zheng & Liu, 2019; Bear Lodge, USA, Moore et al., 2015; Andersen et al., 2016); or external hydrothermal alteration and/or supergene weathering events (e.g., Mount Weld, Australia, Jaireth et al., 2014; Zandkopsdrift, South Africa, Venter et al., 2010; Harper et al., 2015). Thus, deciphering the formation

processes of carbonatite-related REE deposits is challenging, which requires integrated studies of geochemistry of the principle host-rocks and, textural and compositional variations of their constituent minerals (Chakhmouradian & Zaitsev, 2012; Goodenough et al., 2021; Anenburg et al., 2022).

Rare earth element behavior in carbonatite magma sources, magma evolution and hydrothermal modification is relatively poorly constrained by limited numbers of experiments, modeling studies and relatively few natural case studies (Veksler et al, 1998; Bühn, 2008; Chakhmouradian et al., 2015, 2016a, b; Chebotarev et al., 2019, 2022; Yang et al., 2019; Anenburg et al., 2020b; Nably et al., 2020; Walter et al., 2022, 2023). The study of these processes is hindered by the fact that carbonatites are easily modified by hydrothermal reworking, structural events or multiple overlapping processes, resulting in difficulty in recognizing the effects of magmatic processes (Chakhmouradian et al., 2016b; Yaxley et al., 2022). Magmatic evolution processes responsible for REE enrichment are commonly complicated and in many systems may be unique due to extensive crystallization and contamination in carbonatite systems (Bühn et al., 2001; Chen & Simonetti, 2013; Giebel et al., 2019a, b; Anenburg et al., 2020a, b; Fomina & Kozlov, 2021; Bouabdellan et al., 2022; Chmyz et al., 2022; Walter et al., 2022, 2023). For instance, REE accumulation in the world's largest REE deposit at Bayan Obo has been inferred to be controlled by an unusual magmatic evolution history from ferroan-, followed by magnesian- and finally calcio-carbonatite varieties (Yang et al., 2011, 2019). However, this evolutionary sequence is not

representative for most known carbonatite intrusions which typically evolved from calcio-, through magnesian- to ferroan-carbonatite series (Anenburg et al., 2022). Over 60% carbonatites worldwide are predominantly calcite and most economic REE mineralization is associated with Ca-rich carbonatites (Woolley & Kjarsgaard, 2008; Chakhmouradian & Zaitsev, 2012; Smith et al., 2016). However, recent studies indicate high REE concentrations in residual ferroan dolomite carbonatite melt (Anenburg et al., 2022). Given that REE redistribution in the latter processes is results of back reaction with precursor alkali-REE-carbonates (e.g., burbankite and carbocernaite) by hydrothermal fluids expelled from the brine-melt stage (Prokopyev et al., 2016; Anenburg et al., 2022), primary REE enrichment in calciocarbonatitic melt may be a prerequisite. Thus, detailed studies on the evolutionary history of calcio-carbonatitic melt and its relationship to REE enrichment are necessary. In addition, contamination via reaction with silicate rocks during carbonatitic magma ascent is considered to influence REE mineralization by a series of interactions between carbonatite melt and silicate rocks (Anenburg & Mavrogenes, 2018; Giebel et al., 2019a, b; Walter et al., 2021). Generally, this process cannot be easily identified by bulk analyses of radiogenic Sr, Nd and Pb isotopic compositions because these element concentrations in carbonatites are enriched by several orders of magnitude compared to those in associated silicate counterparts (Bell &Tilton, 2002). Equally contamination is limited by the rapid ascent of carbonatite magma, owing to their low density and extremely low viscosity (Jones et al., 2013; Kono et al., 2014).

Identification of contamination processes and their relationship to REE enrichment during carbonatitic magma ascent from integrated petrographic studies and isotopic measurement of Sr, Nd and C could be critical in determining genetic models for REE mineralization systems, but such studies are very sparse (e.g., Giebel et al., 2019b; Fomina & Kozlov, 2021).

Calcite is the crucial magmatic carbonate mineral that accounts for the bulk of the main constituents in most carbonatites. Owing to the fact REE can be incorporated into calcite by coupled substitution with Na, calcite is an important REE carrier in carbonatite and it's textural and REE budget can serve as a monitor for carbonatitic magma evolution (Chakhmouradian & Zaitsev, 2012; Chakhmouradian et al., 2016b). On the one hand, textural and compositional signatures of calcite, especially REE contents and patterns, can be used to trace evolution of carbonatite magma (Chen & Simonetti, 2013; Milani et al., 2017; Ying et al., 2020; Zeng et al., 2022), and ratios of Ce/Ce^{*} and Eu/Eu^{*} are able to indicate their redox state (Chakhmouradian et al., 2016a, b; Chmyz et al., 2022). On the other hand, the in-situ Sr and C isotopic composition of calcite, coupled with mineralogy and mineral chemistry of other proxy minerals (e.g., apatite, mica, amphibole and clinopyroxene) are beneficial for investigating contamination by silicate rocks, and their roles in REE enrichment during carbonatitic magma evolution (e.g., Reguir et al., 2009, 2012; Chakhmouradian et al., 2017; Anenburg & Mavrogenes, 2018; Giebel et al., 2019a, b; Walter et al., 2022, 2023).

Carbonatites from the Maoniuping word-class REE deposit (southwestern China) have been investigated previously to determine the origin of carbonatite, fluid evolution, and REE mineralization (Yuan et al., 1995; Wang et al., 2001; Xu et al., 2003; Hou et al., 2006, 2015; Xie et al., 2009; Liu et al., 2015, 2019a, b; Zheng & Liu, 2019; Weng et al., 2021, 2022a, b). Here, we provide new findings on the integrated petrology, mineralogy, mineral chemistry, and in situ Sr and C isotopic composition of calcite and silicate minerals in different types of calcite carbonatites from a new 1100m drill core. These geochemical features and field observations outline a conceptual model for REE enrichment and mineralization based on magma fractionation and wall-rock contamination. Furthermore, through crystallization modeling, calculations of Raleigh volatilization, and Monte Carlo simulations of contamination, we infer in detail the processes of fractional crystallization and contamination-induced interaction between carbonatitic melt and silicate rocks and assess how the both key processes identified at Maoniuping may have influenced REE-rich carbonatite generation globally.

GEOLOGICAL SETTING

The 270-km-long Mianning-Dechang (MD) belt in eastern Tibetan hosts a total resource of more than 3.2 Mt of REOs and comprise the Maoniuping, Dalucao, Muluozhai and Lizhuang REE deposits (Fig. 1a and b, Yin & Harrison, 2000; Shu & Liu, 2019; Shu et al., 2020; Zhang et al., 2022). This economic metallogenic belt

formed during the late stage of Indian-Asian continental collision (40−24 Ma, Hou & Cook, 2009; Liu & Hou, 2017) and is related to regionally structural activities involving N−S-trending strike-slip movement, ductile shear and transpressional deformation (Fig. 1b; Yin & Harrison, 2000; Deng et al., 2014, 2021; Zeng & Liu, 2022). Carbonatites in the MD belt occur as stocks, dykes, and sills associated with nordmarkite that is a variety of quartz-bearing alkali feldspar syenite (Yuan et al., 1995). Petrological studies suggest that carbonatites and nordmarkite originate by liquid immiscibility of CO_2-rich silicate melt (Hou et al., 2006), and their sources are related to the sub-continental lithospheric mantle (SCLM) that had been previously metasomatized by high-fluxing elements and CO_2-rich fluids from subducted marine sediments (Hou et al., 2015).

The Maoniuping carbonatite-related REE deposit is located at the north part of the MD belt and close to the Yalongjiang strike-slip fault (Fig. 1b). The currently explored resources at Maoniuping comprise more than 3.17 Mt REO at an average grade of 2.95 wt.%, and accessory products of 0.6 Mt Pb (average grade = 0.44 wt.%), 19.67 Mt baryte (average grade = 8.03 wt.%), 13.24 Mt fluorite (average grade = 6.70 wt.%), and 0.83 Mt celestine (average grade = 1.03 wt.%) (Yuan et al., 1995). The host rock geology at Maoniuping includes five main lithological units (Fig. 1c, Yuan et al., 1995; Liu and Hou, 2017): (1) a series of N−S-trending granitic plutons, composed of pink alkalic granite, light gray alkalic granite, and graphic granite; (2) an approximately 1100-m-thick sequence of metamorphic Devonian-Permian clastic

rocks, limestone, and flood basalts intruded by Mesozoic granite; (3) a Paleozoic rhyolite dated at 600–750 Ma; (4) a 700-m-thick coal-bearing Triassic sedimentary sequence overlying the metamorphic basement; and (5) a NE−SW-trending carbonatite-nordmarkite complex, 1400 m long and 260–350 m wide. The distribution and orientation of all the units is controlled by the Haha strike-slip fault (Fig. 1c). At Maoniuping, the carbonatite intruded the cogenetic nordmarkite or Mesozoic alkalic granite as stocks, dykes, and sills. Sensitive high-resolution ion microprobe zircon U-Pb age of 26.6 ± 0.3 Ma (Ling et al., 2016) and arfvedsonite/biotite ^{40}Ar-^{39}Ar age of carbonatite of 27.6 ± 2.0 Ma (Liu & Hou, 2017), have been reported for the nordmarkite and carbonatite, respectively. These ages correspond within error to the SIMS (secondary ion mass spectrometry) U-Th-Pb age of 26.8 ± 0.7 Ma for bastnäsite-(Ce) from carbonatite (Weng et al., 2022a), indicating contemporaneous carbonatite genesis and REE mineralization around 26 Ma at Maoniuping. Previous studies show that most carbonatites are located in the north of the deposit (Guangtoushan section) and are characterized by coarse-grained calcite (50–90 vol.%) with a subordinary mineral paragenesis of aegirine/aegirine-augite, arfvedsonite, fluorite, baryte, and minor bastnäsite-(Ce) in outcrop (Zheng & Liu, 2019).

REE mineralization at Maoniuping is hosted inside carbonatites or carbonatite-derived veins that crosscut nordmarkite as REE mineralized ore veins that show “S”-like outline (Fig. 1c; Yuan et al., 1995; Liu & Hou, 2017). Such REE mineralized ore veins are well developed in the Dagudao section, which is currently

the main open pit, and are composed of low-grade stockworks of multiple veinlets in the lower part of the orebody, grading upwards into progressively thicker veins (Liu et al., 2019a). In the top unit, ore veins can be categorized into four different types based on mineral assemblages and texture (Liu et al., 2019a). The dominant types of ore veins are calcite veins that are typically zoned and comprise K-feldspar (microcline and orthoclase), micas (phlogopite), amphibole (arfvedsonite), pyroxene (aegirine to aegirine-augite), calcite, fluorite, baryte, and bastnäsite-(Ce) (Zheng & Liu, 2019). Previous studies propose that carbonatitic fluids are responsible for the main REE mineralization as most fluid inclusions in bastnäsite-(Ce) are characterized by meteoric water-rich, carbonate-bearing fluids and have homogenization temperatures below 240 ℃ (Xie et al., 2015; Guo & Liu, 2019; Zheng & Liu, 2019). However, recent research has argued that a portion of bastnäsite-(Ce) in carbonatites is of magmatic origin based on their contained melt inclusions and discriminably magmatic-like low U contents (<70 ppm), low $(La/Yb)_n$ ratios (<~30000) and Eu deficiency (δEu = 0.67–0.98) compared to hydrothermal bastnäsite-(Ce) (Weng et al., 2022a).

SAMPLING AND ANALYTICAL METHODS

A total of 44 samples were collected from the first 1100 m of the HZKS drill core (Figs. 1c and 2). Petrographic studies were conduct using a Zeiss Axioskop 40 optical microscope and backscattered electron (BSE) imaging were acquired using

FEI Quanta 450 SEM with an accelerating voltage of 20 kV and a beam current of 30 nA. Representative samples were selected for optical microscope cathodoluminescence (OP-CL) characterization using a Leica DM2700P microscope coupled with a Cambridge Image Technology LTD (CITL) MK 5-2 system at 12 kV accelerating voltage and 350 mA current in China University of Geosciences (CUG), Wuhan, China.

Whole-rock chemical analyses of major and trace elements were carried out at ALS Chemex (Guangzhou) Co., Ltd., China, by X-ray fluorescence (XRF) spectrometry (Fluorine mode) on lithium tetraborate-lithium metaborate flux fused glass disks. Certified reference material (CRM) TDB-1 served as external standard for Cl and multiple reference materials (GBW07241, GBW07237, GBW07211) (Table S1) served as external standards for major and trace elements. Analytical precision was better than ± 2% for major element oxides (SiO_2, Al_2O_3, $Fe_2O_3^T$, CaO, Na_2O, K_2O, MgO, MnO, TiO_2). To obtain Fe^{2+} and Fe^{3+} contents, more than 200 mg of powder, separated from the same disks, was digested with a mixture of H_2SO_4-HF, and was then titrated in a beaker using $K_2Cr_2O_7$ to obtain Fe^{2+} concentration. For trace elements, powders of each sample were accurately weighed to 0.100 g and then mixed with $Li_2B_4O_7$ or $LiBO_2$ (specifically for analyses of REE concentrations) in a Savillex Teflon beaker. The mixture was heated for 24 h at 80 °C and then dissolved in an acid mixture of 1.5 ml HNO_3, 1.5 ml HF, and 0.5 ml $HClO_4$ for digestion in a high-temperature oven at 180 °C for 72 h. After cooling, the sample solution was

transferred to a plastic bottle and diluted with 1% HNO_3 to 50 ml. The trace element concentrations were analyzed using an Agilent 7700x quadrupole inductively coupled plasma mass spectrometer (ICP-MS). Multiple reference materials (OGGeo08, MRGeo08, OREAS-120, OREAE-45e, GBM908-10, STSD-1) (Table S1) served as external standards, and analytical precision was better than 10%.

The carbon and oxygen isotopic composition of calcite from carbonatites was determined at CAGS. The selected samples were washed with distilled water and dried at room temperature. Samples were then crushed to less than 200 mesh in an agate mortar. Each powder was treated with 100% anhydrous H_3PO_4 at 50 ℃ to generate CO_2 that was subsequently purified, and then C and O isotopic compositions were measured using a Finnigan MAT-251 isotope ratio mass spectrometer. The analytical uncertainty is better than 0.15‰ and 0.020‰ (2σ) for C and O isotope ratios, respectively. Isotopic compositions reported here are normalized to the Vienna Pee Dee Belemnite standard (V-PDB) for $\delta^{13}C$ and Vienna Standard Mean Ocean Water (V-SMOW) for $\delta^{18}O$.

The major element compositions of silicate minerals and calcite were determined using a JXA-iHP200F electron microprobe at the Institute of Mineral Resources, CAGS. Accelerating voltage was 15 kV using a beam current of 10 nA (for carbonates) and 20 nA (for other minerals). The beam diameter was 5 μm for silicates and 10 μm for calcite. All elements were measured by peak mode and the peak counting times for F was 40s; for all the other elements it was set to 20 s on peak and 10 s on background.

Natural and synthetic standards were used for calibration (Table S1) and raw data were corrected using ZAF procedures. The elements Al, Ba, F, Fe, K, Mg, Mn, Na, Si, and Ti were mapped for phlogopite using the same instrument at an accelerating voltage of 15 kV and a beam current of 10 nA. A total of 602 × 476 points were gathered for each element map with dwell time of 50 ms for each point and a probe diameter of 5 μm.

The in-situ trace element analyses of minerals were conducted using a RESOlution 193 nm laser ablation (LA) system coupled to a Thermo iCAP-RQ ICP-MS in the State Key Laboratory of Geological Process and Mineral Resources (GPMR), CUG. Laser ablation spots were located on the same crystals analyzed by EPMA, with energy density of 2.8–3.5 J/cm^2 at a repetition rate of 8–10 Hz and a beam diameter of 33–50 μm depending on the size of mineral grains. Multiple reference materials (NIST 610, NIST 612, BIR-1G, BCR-2G and BHVO-2G, Jochum et al., 2005) served as external standards (Table S1), which together with Ca from EPMA, were used for concentration calibration (Liu et al., 2008). The precision and accuracy are better than 5% for REEs and 10% for all other trace elements (1σ RSD; Chen et al., 2011). Data were processed using an Excel-based software ICPMSDataCal 12.2 via off-line selection and integration of background and analytical signals, and time drift correction and quantitative calibration (Liu et al., 2008; Lin et al., 2016). Time resolved mass spectra were checked to identify and exclude analyses affected by mineral micro-inclusions.

295 The in-situ carbon isotope composition of calcites from selected carbonatite
296 intrusions was determined on a RESOlution 193 nm laser ablation system coupled to
297 a Nu Plasma II multicollector (MC)-ICP-MS at GPMR, CUG. ^{13}C and ^{12}C were
298 measured simultaneously in Faraday cups H3 and L4, and the $^{25}Mg^{2+}$ ion signal was
299 acquired in the central cup (Lu et al., 2022). All measurements were performed in low
300 mass resolution mode of ~400, whereas medium mass resolution (~4000) was adopted
301 to resolve spectral interferences (Lu et al., 2022). The samples were ablated in a
302 helium atmosphere (0.3–0.4 L min^{-1}) mixed with 4 mL min^{-1} N_2, which was then
303 combined with argon gas (~0.6 L min^{-1}) before entering the plasma torch (Chen et al.,
304 2017). Analyses were performed using a laser beam diameter of 193 μm with energy
305 density of 3 J/cm^2 and repetition rate of 12 Hz. Each analysis consists of 30 s of
306 background measurement, 40 s of ablation, and 50 s of washout. A standard-sample
307 bracketing (SSB) method was adopted to correct for instrumental mass bias with the
308 external standard SXD8 calcite (Table S1). Every 5 analyses were bracketed by an
309 analysis of an obtained Oka153 calcite (Chen et al., 2017) as the monitor standard to
310 determine the accuracy and precision. The analytical $\delta^{13}C$ values were calibrated
311 using Iso-Compass software (Zhang et al., 2020) for spectral interferences from
312 doubly charged ions (i.e., $^{24}Mg^{2+}$ for $^{12}C^{+}$ and $^{26}Mg^{2+}$ for $^{13}C^{+}$) and analytical
313 uncertainty is better than 0.25‰ (1σ) for C isotopes based on repeated measurement
314 of the SXD8 calcites (Lu et al., 2022).

In-situ Sr isotopic measurements of calcites were conducted on the same LA-(MC)-ICP-MS instrument configuration at GPMR. Laser ablation spots for Sr isotopic measurement were carried out on the same calcite grains analyzed for in-situ C isotope compositions. All analyses were conducted with a laser beam diameter of 75 μm with an energy density of 3 J/cm^2 and repetition rate of 10 Hz. Every 4–6 sample analyses were bracketed by analysis of an in-house coral (Qingdao) as external standard to check the analytical reliability and stability. The average $^{87}Sr/^{86}Sr$ ratio obtained for the coral standard was 0.70918 ± 0.00004 (2σ, n = 65, Table S1), corresponding to the values of 0.70910 ± 0.00002 to 0.70923 ± 0.00002 reported by ID-TIMS (Bizzarro et al., 2003; Chen et al., 2018). Double-charged ions of $^{167}Er^{2+}$, $^{171}Yb^{2+}$, $^{173}Yb^{2+}$ were monitored based on the method of Ramos et al. (2004). To exclude the interferences of Kr and Rb, the interferences of ^{84}Kr on ^{84}Sr, ^{86}Kr on ^{86}Sr, and ^{85}Rb on ^{87}Sr were corrected based on the isotopic ratios of $^{83}Kr/^{84}Kr$ = 0.20175, $^{83}Kr/^{86}Kr$ = 0.66474, and $^{85}Rb/^{87}Rb$ = 2.5926, respectively. The $^{87}Sr/^{86}Sr$ ratios were calculated and calibrated from the interference-corrected $^{86}Sr/^{88}Sr$ using the exponential law method described by Yang et al. (2014).

PETROGRAPHY AND MINERALOGY

A simplified log that illustrates the lithological variations in the HZKS-1 drill core is shown in Figure 2. A rock paragenesis of alkaline granite, nordmarkite, and

carbonatite was determined from the studied drill core. Representative petrographic and mineralogical characteristics are shown in Figures 3–6.

Alkaline granite

The alkaline granite is found throughout the drill core, down to 950 m (Fig. 2) and is gray in color and mostly medium- to fine grained with equigranular texture. It is characterized by the presence of alkali feldspar and quartz with minor biotite, zircon, and apatite (Fig. 3c). The principal minerals in fresh alkaline granite are microcline (~30 vol.%), perthite (~20 vol.%), orthoclase (~15 vol.%), albite (~10 vol.%) and quartz (20–25 vol.%). Tabular microcline crystals are 0.5 to 2 mm in size and share planar contacts with lath-shaped perthite. Albite grains are 50–100 μm in size and primary quartz occurs as subhedral to anhedral crystals interstitial to perthite and microcline (Fig. 3c).

In the top ~ 100 m of the drill core, alkaline granite is weathered, appears leached, and has a loose or porous texture (Fig. 3e). In proximity to carbonatite II, the alkaline granite exhibits carbonation and REE mineralization, which is distinct from fresh granite. The altered granite is reddish in color; contains platy fluorite, baryte, and bastnäsite-(Ce); and hosts comb-like aggregates of amphibole and clinopyroxene at the contact with carbonatite (Fig. 3e).

354 **Nordmarkite**

355 Nordmarkite spatially occupies in the drill core at 190–550, 890–908, 924–933,
356 and 845–1100 m. In hand specimen, fresh nordmarkite is gray- to white (Fig. 3a) and
357 consists of alkali feldspar, quartz, pyroxene, and phlogopite with accessory zircon,
358 apatite, magnetite, pyrite, and magnetite. Alkali feldspar accounts for over 70 vol.%
359 of the rock and can be subdivided into microcline (30 vol.%), orthoclase (30 vol.%)
360 and albite (10 vol.%) (Fig. S1a and b). Albite occurs along the cleavage of orthoclase
361 grains as irregularly perthitic crystals (Fig. S1a). In some places, feldspar crystals are
362 partly altered to sericite, which increases appreciably with proximity to the contact
363 with carbonatite II (Fig. S1c and e). Quartz occurs interstitially to microcline and
364 orthoclase (Fig. S1d). Pyroxene occurs as skeletal crystals or aggregates that usually
365 contain elongated or isometric apatite, euhedral titanite and bastnäsite-(Ce) (Fig. S1b,
366 d and f).
367

368 **Calcite carbonatite**

369 Based on textural characteristics and mineral assemblages, two varieties of
370 carbonatites are recognized, including medium- to coarse-grained carbonatite
371 (carbonatite I, Fig. 3g–i) and super coarse-grained carbonatite (carbonatite II, Fig. 3j–
372 k). Generally, carbonatite I is found at greater depths and gradually coarsens upward
373 into carbonatite II that contains numerous centimeter-scale grain size intervals and

374 REE minerals (Fig. 3k). Both varieties are predominantly composed of calcite, but
375 can be distinguished by variable proportions of silicate minerals (e.g., phlogopite,
376 riebeckite-arfvedsonite, aegirine-augite), fluorite, and baryte. Additional details that
377 distinguish carbonatite I and II are presented below:

378 **The medium- to coarse-grained calcite carbonatite (carbonatite I)**

379 The carbonatite I mainly occurs from 953 to 730 m in the deep drill core (Fig. 2)
380 and intrudes nordmarkite and alkaline granite as veins, dykes and plugs (Figs. 2 and
381 3d, f and j) less than 1 m in width. This variety exhibits gray to white color,
382 equigranular texture and is comprised of overwhelmingly fine-grained calcite (<500
383 μm in diameter and 85 to 90 vol.%), ferromagnesian silicates (phlogopite and
384 riebeckite, 5–10 vol.%), and a handful of magnetite and molybdenite grains (total <1
385 vol.%) (Fig. 4a–d). Euhedral- to subhedral calcite crystals are equant, and oval, or
386 lobate in shape and 100 to 500 μm in size (Fig. 4a). The fine grains, which are
387 transparent, show colorful extinction and weak twinning in cross-polarized light (Fig.
388 4c) and mid-gray color in BSE images (Fig. 4e). Under OP-CL imaging, calcite
389 displays bright orange to blood-red grains that have slight core to rim zonation (Fig.
390 4i). The boundary between calcite crystals is usually planar, which, combined with the
391 lack of mechanical twinning, shows that they have not undergone textural
392 re-equilibration. Phlogopite in carbonatite I is 0.2 to 0.5 mm in size and occurs
393 interstitially to calcite with the same planar contacts (Fig. 4b). Most phlogopite grains
394 display dark-green color in plane-polarized light and are disseminated in carbonatite I

(Figs. 3g–h and 4b). Riebeckite is euhedral prismatic or needle-like crystals enclosed in phlogopite as compact inclusions (<50 μm across) (Fig. 4b and f). Accessory minerals include magnetite and molybdenite that form aggregates or clusters in local parts of carbonatite I (Fig. 4d).

Characteristics of carbonatite I can vary over short distances, on the order of tens of meters (Fig. 4g and h). These carbonatites are pink and show calcite oikocrysts containing tiny bastnäsite-(Ce) inclusions (Fig. 4g). In BSE images, the bastnäsite-(Ce) inclusions (commonly <10 μm in size) are orientated along calcite cleavages or occur as broken trails of elongated, spindle- or pill-like crystals (Fig. 4h), whose abundance ranges significantly from absent to as much as 1–2 vol.%.

The super coarse-grained calcite carbonatite (carbonatite II)

The carbonatite II occupies sections at 800–895 m, 730–760 m, 650–680 m, and 280–300 m throughout the HZKS-1 drill core (Figs. 2 and 5). These samples commonly exhibit inequigranular and sometimes pegmatoidal texture (Figs. 5d), and are typically represented by large calcite crystals range from commonly 2–5 millimeters (Fig. 5) to locally several centimeters in size (Fig. 3k). In some parts, closely anchimonomineralic calcite carbonatite can be found (Figs. 3j). Statistically, most carbonatite II is comprised of dominant calcite (60–70 vol.%), fluorite (~10 vol.%), and baryte (~10 vol.%) grains accompanied by variable amounts of phlogopite (~5 vol.%), magnesioarfvedsonite (~5 vol.%), aegirine (~5 vol.%), and minor microcline, quartz, pyrite, and galena (Fig. 5a–d, h–k). Bastnäsite-(Ce) is

widespread and volumetrically accounts for over 10% of carbonatite II in some cases (Fig. 5b, j). Calcite in carbonatite II is subhedral to anhedral, elongated or anhedral crystals (Fig. 5d) and shows complex optical characteristics with subtle undulatory extinction, thick twin lamellae in cross-polarized light (Fig. 5e), and flame-like cores fading to a dark orange rim under OP-CL images (Fig. 5k). Locally, misoriented microfractures show up and obliquely traverse the cleavage of calcite crystals, whose grain boundaries become serrated and bulging (Fig. 5f). These textual characteristics suggest a response to stress and ductile deformation of carbonatite II.

Fluorite in carbonatite II occurs as subhedral, elliptical to elongated aggregates disseminated in the calcite-dominant matrix (Figs. 3k and 5h–k), and is dark blue in CL images (Fig. 5k). Boundaries between fluorite and calcite are planar contacts without crosscutting or intersection, representing equilibrium crystallization. Baryte exhibits patchy texture and commonly occurs as anhedral aggregates along calcite fractures (Fig. 5i–j), whereas quartz, which is absent in carbonatite I, is 0.5 to 1 mm in size and occurs interstitially to calcite with dark gray color in BSE images (Fig. 5i). Arfvedsonite (or riebeckite) shows compact, comb-like, euhedral configuration (Fig. 5c). The REE minerals in carbonatite II are mainly bastnäsite-(Ce), showing large, lath-shaped, and euhedral crystals (>500 μm) that syntactically intergrow with parisite-(Ce) (Fig. 5j).

Distribution and character of REE mineralization

In general, REE mineralization in the drill core can be mainly found inside carbonatite II and at the contact zone between carbonatite and wall rocks. As described above, REE minerals in carbonatite II are dominantly bastnäsite-(Ce) with lesser amounts of parisite-(Ce), both of which exhibit patchy zoning (Fig. 5j) and have rosette-like shape alongside fluorite, calcite, and in some places baryte (Fig. 5b and i). In contrast, REE mineralization in the contact zone is characterized by the following three key features that are distinct from those in carbonatite II: (1) REE minerals: bastnäsite-(Ce) is abundant (over 10 vol.% in some parts) and occurs interstitially to calcite, with which it shares planar contacts (Figs. 3d and 6a); (2) in BSE images most bastnäsite-(Ce) is unzoned and shows lath-shape, euhedral crystal, or random aggregates with 0.2–0.5 cm in length (Fig. 6e–g); (3) a high abundance of silicates, including phlogopite, aegirine or aegirine-augite, riebeckite or arfvedsonite and microcline, which are intergrowth with bastnäsite-(Ce) and exhibit core to-rim texture (Fig. 6a–d).

RESULTS

Whole-rock chemistry

The whole-rock geochemical results are provided in Table 1, normalized REE patterns are illustrated in Figure 7, and major and trace element discriminant diagrams are shown in Figures S2–S3. Of all the analyzed samples, the fresh nordmarkite

456 commonly comprises SiO_2 contents of 68.05–70.09 wt.%, the highest concentrations
457 of Na_2O + K_2O (means = 11.09 wt.%) (Fig. S2a and b), but relatively low REE
458 contents and low LREE/HREE ratios (208–455 ppm and <87.4, respectively, Figs. 7b,
459 S2e and f). In comparison, nordmarkite samples in contact zones have lower Na_2O +
460 K_2O contents (6.50 wt.%), but higher contents of SO_3 (1.27 wt.%), F (2.1 wt.%) and
461 REE (2603 ppm) (Fig. S2e and f). For alkali granite, the fresh alkali granite is
462 characterized by high contents of SiO_2 (66.87–76.01 wt.%) and $(La/Yb)_N$ ratios
463 (27.0–306), but low contents of CaO, SO_3, F, Nb, REE (431–3202 ppm), and ratios of
464 Zr/Hf and Nb/Ta (27.34–33.65 and 35.19–87.39, respectively) (Fig. S2d). In contrast,
465 the altered variety has variable contents of SiO_2 (38.21–73.40 wt.%), CaO (0.13–
466 16.30 wt.%), higher contents of F (up to 3.10 wt.%), HREE (30.9–1310 ppm), Nb
467 (125–1925 ppm), and low $(La/Yb)_N$ ratios (1.52–67.7; Figs. S4c, f, and i). Moreover,
468 the altered alkali granite is further characterized by tetrad-effect-like REE patterns
469 with pronounced negative Eu anomalies (Fig. 7b), indicating that they were formed
470 from a more fractionated granitic system; the result of a magma-fluid system evolving
471 under open conditions; or the products of a separate magmatic event (Irber, 1999).
472 Both carbonatites I and carbonatite II are consistently calcium-rich (CaO = 41.62
473 to 52.73 wt.%) and exhibit high CaO/ (CaO+MgO+FeO) ratios of 0.96–0.98 (Table 1),
474 and are therefore classified as calcite carbonatites (Fig. S3). Basically, carbonatite I is
475 much lower in SiO_2, F, SO_3 and BaO than carbonatite II (Fig. S4b and e), and has
476 similar low MgO, FeO, MnO, P_2O_5 (<0.25 wt.%) contents (Fig. S4b, d, e). Their

trace-element budget is characterized by low REE contents (3098–3198 ppm), low ratios of LREE/HREE and $(La/Sm)_N$ (12.8–28.9 and 2.75–10, respectively) with slight Eu deficiency ($\delta Eu = Eu_N /(0.5Sm_N + 0.5Gd_N)$: 0.89–0.94), unity δCe ($\delta Ce = Ce_N /(0.5La_N + 0.5Pr_N)$: 1.00–1.04), and near-chondritic Y/Ho (22.8–25.8) and Th/U ratios (0.2–3.3). In comparison, the carbonatite samples in contact zones have a wide range of CaO and SiO_2 contents (Fig. S4a), and higher Al_2O_3, Na_2O, K_2O, F and SO_3 contents, but relative depletion in SrO and MnO (Fig. S4b–e).

Compared to carbonatite I, carbonatite II has variable SiO_2 contents (0.15–15.03 wt.%), evident by presence of large proportions of phlogopite, clinopyroxene amphibole, and quartz (Fig. 5c and i). Overall, they contain similarly low P_2O_5 contents (<0.11 wt.%), but are much enriched in BaO, SO_3 and F (up to 13.40 wt.%, 5.03 wt.% and 15.70 wt.%, respectively). Due to the large number of bastnäsite-(Ce) grains, carbonatite II hosts high levels of REE (2241–127,686 ppm) and exhibits steep chondrite-normalized REE patterns with over three orders of magnitude variation from La to Lu ($(La/Yb)_N$ = 247–2202; Fig, S4c and h). Moreover, carbonatite II is further discriminable in δCe (0.89–1.33) and δY ($\delta Y = Y_N / (0.25Dy_N + 0.75Ho_N)$: 0.72–1.30) from carbonatite I (δY = 0.77–0.86) (Fig, S4i).

Mineral composition

Calcite

The chemical compositions of calcite from carbonatite I to II, and contact zones are listed in Tables S2–S3. The formula calculations for calcite are based on one cation with CO_2 calculated from stoichiometry. Chemical variations of calcite are illustrated in Figures 8 to 10. In general, calcites in all carbonatite varieties contain Ca and small amounts of Fe and Mg with a mean formula of $(Ca_{0.966}Mg_{0.005}Fe_{0.008}Mn_{0.013}Sr_{0.007})CO_3$ All analyzed samples are characterized by discernible Sr (<0.014 in atoms per formula unit (a.p.f.u.)), limited S (<0.002 a.p.f.u.), and similar Y/Ho ratios (23.8–34.7) that plot within the CHArge-and-RAdius-Controlled (CHARAC) field (Fig. 10) where elements of similar charge and radius display extremely coherent behavior and retain their respective chondritic ratio (Bau, 1996). Combining specific textural, major and trace characteristics and mineral assemblages, four generations of calcite are identified, namely Calcite-I, Calcite-II, Calcite-III and Calcite-IV.

Calcite-I (Cal-I) is from carbonatite I and is characterized by low concentrations of Sr, Fe, Mg, and Mn (Fig. 8). This variety contains the lowest contents of Ba, Pb and ΣREE (6.55–241, 51.9–109, and 448–1221 ppm; on average 29.3, 70.8, and 876 ppm, respectively), but relatively high Y concentration of 92.5–281 ppm (mean = 206 ppm). The Zn, Th, As, and U abundances are low. The chondrite-normalized REE patterns of Cal-I exhibit a gentle negative slope with lower $(La/Yb)_N$ and $(La/Nd)_N$ ratios of 1.41–5.34 and 0.37–1.11, respectively (Fig. 10a). In addition, the δEu, δY

517 and Y/Ho ratios are consistently close to chondrite values (mean = 0.91, 0.89, 26.6,
518 respectively) (Fig. 10b) (Bau, 1996; Chakhmouradian et al., 2016b).

519 Calcite-II (Cal-II) occurs in carbonatite I, but differs from Cal-I in the presence
520 of baryte and bastnäsite-(Ce) inclusions (Fig. 4h). Compared to Cal-I, Cal-II contains
521 elevated Sr, Mg, Fe, Mn concentrations (mean = 0.009, 0.005, 0.007, and 0.011
522 a.p.f.u.; Table S2 and Fig. 8) but distinctly higher REE contents (747–2144 ppm;
523 mean = 1359 ppm) and LREE-rich chondrite-normalized REE patterns with higher
524 $(La/Yb)_N$ and $(La/Nd)_N$ values (4.72–35.9 and 0.5–2.2, respectively; Fig. 10a).

525 Calcite-III (Cal-III) is found in carbonatite II and exhibits variable, but generally
526 higher Sr concentrations (mean = 0.01 a.p.f.u.; Fig. 8) relative to Cal-I and Cal-II.
527 Y/Ho values of this variety (up to 34.7) are mostly within the CHARAC field and
528 only a few samples have higher, non-chondritic values (Fig. 10b). Cal-III is
529 characterized by the highest REE contents (1011–2720 ppm; mean = 1740 ppm) with
530 the chondrite-normalized REE patterns varying over two orders of magnitude from La
531 to Lu ($(La/Yb)_N$ = 6.52–61.5; avg. = 26.7) and $(La/Sm)_N$ ratios up to 8.30 (Fig. 10a).
532 In common with Cal-II, Cal-III hosts low concentrations of Y, Pb, Zn (mean = 119,
533 87.8, and 9.57 ppm, respectively), but slightly elevated Na content (mean = 265 ppm).

534 Calcite-IV (Cal-IV) samples from the contact zones are further divided into
535 calcites either from carbonatites or within carbonated nordmarkite and alkali granite.
536 Compared to other generations of calcite, Cal-IV has the lowest SO_3 and SrO contents,
537 but is more enriched in FeO, MgO, and especially MnO (Fig. 8). Moreover, this

variety has low levels of Ba, Pb and U (<155, <126, and <0.61 ppm, respectively), but much higher REE contents (818–2775 ppm; mean = 1350 ppm). Chondritic-normalized REE profiles of Cal-IV show LREE-rich patterns with respect to chondrite ($(La/Yb)_N$ ratios of 11.3), and chondritic Y/Ho and δEu values (27.6 and 0.87, respectively) (Fig. 10a).

The four generations of calcite exhibit continuous chemical variation, as shown in composition scatter diagrams between Ca and other major elements (Fig. 9). Strontium increases gradually from Cal-I to Cal-II and Cal-III (from 0.03 to 0.15 a.p.f.u.), but eventually drops in Cal-IV (0.941–0.978 a.p.f.u.) accompanied by more variable Ca concentrations (Fig. 9a). Magnesium is inversely correlated with Ca (R^2 = 0.615) where Mg concentrations steadily increase from Cal-I to Cal-IV (Fig. 9b); the same is true of Fe and Mn with respect to Ca (R^2 = 0.641 and 0.665, respectively; Fig. 9c and d).

Phlogopite

Representative analyses of the chemical compositions and site assignments of mica are listed in Table S4. Formula calculations for mica are based on an ideal trioctahedral formula ($XY_3[Z_4O_{10}][OH, F, Cl]_2$) and the results are normalized to 7 (tetrahedral [Z] plus octahedral [Y]) due to possible vacancies on interlayer sites [X]. All micas from the HZKS-1 drill core are classified into phlogopite ($[K_{0.954}(Al_{0.203}Mg_{2.332}Fe_{0.368}Ti_{0.021}Mn_{0.007})(Al_{0.466}Si_{3.534}O_{10})(F,OH)_2]$) based on high

559 Mg contents (1.991–2.750 a.p.f.u.) and low tetrahedral Fe^{3+} (<0.001 a.p.f.u.) (Foster,
560 1960). These phlogopites generally contain low Ba, Ca, and Na (<0.016, <0.009, and
561 <0.033 a.p.f.u., respectively), and high F and K (mean = 1.369 and 0.963 a.p.f.u.,
562 respectively), and low Na contents (0.009–0.033 a.p.f.u.). A strong negative
563 correlation between Mg and Si towards higher Al indicates the effect of the
564 phlogopite–eastonite substitution ($Mg^{2+} + Si^{4+} \leftrightarrow {}^{IV}Al^{3+} + {}^{VI}Al^{3+}$, Fig. 11a). In order
565 to investigate the degree of halogen enrichment, intercept values, IV(F), IV(Cl), and
566 IV(F/Cl), are calculated by equations: $IV(F) = 1.52X_{phl} + 0.42X_{ann} + 0.20X_{sid} -$
567 $\log(X_F/X_{OH})$; $IV(Cl) = -5.01 - 1.93X_{phl} - \log(X_{Cl}/X_{OH})$; and IV(F/Cl) = IV(F) – IV(Cl)
568 (Munoz, 1984). Three populations of phlogopite can be identified from major element
569 compositions and halogen intercept values: (1) One population in carbonatite I (Phl-I),
570 (2) a main core-rim population from contact zones (Phl-II), and (3) accessory phases
571 in nordmarkite (Phl-III).

572 Phl-I is discriminated by the lowest F contents (0.927–1.198 a.p.f.u.), with high
573 levels of Ti (up to 0.052 a.p.f.u., Fig. 11b and c), intermediate Mg# (88–95) and Na
574 (0.009–0.021 a.p.f.u.), and minor Mn (Fig. 11f). The intercept values of IV(F), IV(Cl)
575 and IV(F/Cl) of this group range from 1.85 to 2.10, –2.60 to –3.90, and 4.59 to 5.86,
576 respectively. In comparison, Phl-II hosts higher Na (up to 0.033 a.p.f.u.) and F
577 (1.013–1.717 a.p.f.u.) (Fig. 11g–i), and the lowest Mn and Ti contents (Fig. 11b–d).
578 Moreover, they are further distinct in having variable Mg# (85–97) with an
579 Mg-Si-rich core (Phl-IIC) and an Al-rich rim (Phl-IIR) (Fig. S5). Phl-III is

compositionally close to the ideal stoichiometry of phlogopite and can be discriminated from Phl-I and Phl-II in having much lower Al and Na contents (0.559 and 0.009 a.p.f.u., respectively), intermediate IV(F/Cl) (4.64–5.81), and the highest Mg# (94–98) and Mn contents (Fig. 11b–f).

Amphibole

The results of analyses of amphibole are summarized in Table S5. Formula calculations for amphibole are based on 24 oxygens and (O, OH, Cl) = 2 as $[K_{0.282}Na_{0.464}][Na_{1.503}Ca_{0.445}][Mn_{0.037}Mg_{2.799}Fe^{2+}_{1.161}Fe^{3+}_{0.629}][Al_{0.124}Ti_{0.008}Si_{7.925}]O_{22}(F, OH)_2$. In general, the chlorine content is minimal, but all amphiboles contain significant F, Fe, Mg, Na (0.46–1.73, 1.02–2.06, 1.47–2.21, and 2.63–3.80 a.p.f.u., respectively), and measurable K (0.09–0.37 a.p.f.u.) and Ca (0.13–1.91 a.p.f.u.) contents. Most amphiboles have high Mg/(Mg + Fe^{2+}) ratios (0.58–1.00) and octahedral Na contents (Na_B >1.50 a.p.f.u.), and are therefore classified as magnesioriebeckite-magnesioarfvedsonite (Leake et al., 1997). Classification diagrams show that amphibole in carbonatite I is mainly magnesioriebeckite, whereas those in carbonatite II and contact zones mainly belong to magnesioarfvedsonite (Fig. S6).

Clinopyroxene

Major compositions of clinopyroxenes are listed in Table S6. The measured compositions range from $Ae_{97}Di_3Hd_0$ to $Ae_{52}Di_{11}Hd_{37}$, where clinopyroxenes in contact zones are aegirine with some aegirine-augite, and the main Ca-rich aegirine-augite occurs in carbonatite II (Fig. S7). All samples have significant Mg (up to 0.322 a.p.f.u.) with minor Mn, Al and Ti contents (up to 0.026, 0.053, and 0.039 a.p.f.u., respectively).

C-O isotopic compositions of calcite in carbonatite

The C and O isotopic compositions of calcite separates from carbonatite I, II, and the contact zones are presented in Table 2. The results show that $\delta^{13}C_{VPDB}$ values range from –7.1 to –6.2 ‰ and $\delta^{18}O_{VSMOW}$ values are between 5.4 and 11.0‰, which mostly plot in the box of primary igneous carbonate (PIC, Taylor et al., 1967) (Fig. 12). A number of data from Cal-IV in carbonatite II samples are located to the right of the PIC field. The O isotope ratios show a progressive increasing trend from Cal-I to Cal-III with a range from 6.6 to 9.2‰ but, in turn, decrease to 8.1‰ in Cal-IV.

In-situ Sr-C isotopic compositions recorded in various calcites

The measured results of in-situ Sr–C isotopic analyses of calcites are listed in Tables 3 and 4. The low $^{87}Rb/^{86}Sr$ ratios (<0.00008) and high Sr contents (over 7000 ppm) of all varieties of calcite indicate that the measured $^{87}Sr/^{86}Sr$ ratios can

accurately record the initial Sr isotopic composition due to negligible effects from Rb decay. The radiogenic Sr isotopic compositions obtained in the earlier-crystallizing Cal-I and Cal-II are similar to those of carbonatites (0.70605–0.70632, mean = 0.70613, Wang et al., 2001; Xu et al., 2003), as expressed by $^{87}Sr/^{86}Sr$ ratios of 0.70605–0.70623 (mean = 0.70613) and 0.70605–0.70636 (mean = 0.70617), respectively (Fig. 13). In contrast, the Sr isotopic ratios of Cal-III and Cal-IV yield high and variable ranges from 0.70602 to 0.70670 (mean = 0.70629) and 0.70605 to 0.70660 (mean = 0.70626), respectively, indicating more radiogenic Sr characteristics (Fig. 13).

In addition to Sr isotopic composition, the four generations of calcite are further distinguished by their in-situ C isotopic compositions (Table 4). A progressive decrease in $\delta^{13}C_{V\text{-}PDB}$ occurs from a high-value $\delta^{13}C$ of Cal-I (mean = –5.55‰, n = 26) downward to relatively low $\delta^{13}C$ values (mean = –6.26‰, n = 24) in Cal-II, followed by more depletion in $\delta^{13}C$ in Cal-III and Cal-IV (up to –9.97 and –8.61‰, respectively), which slightly deviates from mantle values (Fig. 17d). This feature differs from the bulk C isotopic compositions analyzed for calcite (Niu et al., 2005; Xu et al., 2002; Hou et al., 2006, 2015) and carbonatites in previous studies (Hou et al., 2015).

DISCUSSION

Origins of calcite and silicate minerals in various carbonatites at Maoniuping

Most known carbonatites are derived from carbonate-silicate magma via liquid immiscibility or fractional crystallization (Wyllie, 1998) and have the ability to carry REE, Sr and Ba (Veksler et al., 1998; Song et al., 2016). Carbonatitic magmas are capable of rapid ascent owing to their low viscosity and density (Walter et al., 2021), and could intrude shallow crust as carbonate cumulates (Mitchell, 2005; Xu et al., 2010). Carbonatites from drill hole HZKS-1 at Maoniuping are carbonate cumulates and are similar to those that formed by carbonatitic melts (Xu et al., 2010; Chakhmouradian et al., 2016a) and are composed of large proportions of calcite and minor silicate minerals, such as mica, clinopyroxene and amphibole (Reguir et al., 2009, 2012). Textural and chemical evidence suggest that carbonatite I and II derived from different carbonatitic magma stages, and record the evolution of carbonatitic magma. Reliable interpretation of the evolution of carbonatitic magma and assessment of its relationship to REE enrichment and mineralization, requires discrimination of the origins of the different generations of calcite and silicate minerals in various calcite carbonatite stages.

Calcite is the principal constituent and accounts for more than 90 vol.% of carbonatite in some samples. Considering that calcite is easily amenable to textural re-equilibration and subsolidus hydrothermal overprinting at low temperature and pressure (Barker, 2001; Schultz et al., 2013; Chakhmouradian et al., 2016a),

660 determining the genesis of calcite requires an approach that combines petrographic
661 observations, mineral chemical and isotopic compositions. The four generations of
662 calcites show near-CHARAC Y/Ho ratios and PIC-like C-O compositions. These
663 characteristics clearly indicate magmatic origin of all generations of calcite, and
664 significantly differ from those of hydrothermal or metasomatic calcites, either of
665 which has wide Y/Ho ranges (15–55) and variable $\delta^{13}C$–$\delta^{18}O$ values completely
666 outside the PIC field (Figs. 8a and 11b; Bau, 1996; Taylor, 1967). Among four
667 generations, Cal-I is considered as the early-crystalizing product from initial
668 carbonatitic melt, owing to: (1) the lowest Sr, Na, Ba, Pb and REEs with relatively
669 high Y contents, similar with those of early-crystalizing calcite reported in literature
670 (Table S3) (Hornig-Kjarsgaard, 1998; Bühn et al., 2001; Chakhmouradian et al.,
671 2016b); (2) the gently sloping chondrite-normalized REE patterns with the lowest
672 $(La/Yb)_N$ and $(La/Nd)_N$ ratios (Fig. 11a); (3) the highest in-situ $\delta^{13}C$ values of –5.5‰,
673 indicating a lack of modification by fluid-rock interaction, Rayleigh isotopic
674 fractionation, or decarbonation (Fig. 12); (4) the limited carbonatite-like $^{87}Sr/^{86}Sr$
675 ratios; and (5) polygonal mosaic textures and near unity δCe values (0.98–1.04) and
676 slight Eu deficiency (δEu = 0.89–0.93) of their host carbonatite I (Fig. 4a and c).
677 These features are evidenced by Cal-I, and, as the early melt is expected to have the
678 lowest La, REE contents and low $(La/Yb)_N$, the later calcite generations (Cal-II,
679 Cal-III and Cal-IV) are inferred to have crystalized from more evolved carbonatite
680 magma.

Phlogopite is the essential K-bearing silicate mineral in calcite carbonatites and is enriched in Mg, Ti but poor in Fe^{2+} (Table S3 and Fig. 11). Strong textural and chemical evidence suggest that Phl-I is the primary magmatic phase that crystallized directly from carbonatitic melt (Reguir et al., 2009; Massuyeau et al., 2015). In contrast, Phl-II in contact zones cannot be ascribed to magmatic genesis owing to their high abundance and distribution alongside aegirine/aegirine-augite and microcline (Fig. 6a). These features reflect an increased Si activity in the carbonatite magma, which is opposite to the general trend of decreasing SiO_2 contents and silica activity during fractionation of carbonatitic magma (Barker, 2001; Krasnova et al., 2004; Lee et al., 2004; Reguir et al., 2012; Massuyeau et al., 2015; Weidendorfer et al., 2017; Giebel et al., 2019a, b and references therein). Thus, we infer that Phl-II is a metasomatic product due to interaction between carbonatite melt and silicate rocks (nordmarkite).

Amphibole (riebeckite and arfvedsonite) and clinopyroxene (aegirine-augite and aegirine) are important ferromagnesian silicates in carbonatites in the HZKS-1 drill core, and are chemically dominated by sodic and sodic-calcic varieties. As riebeckite occurs in carbonatite I and shows euhedral crystals enclosed in Phl-I, they are interpreted as primary silicates that crystallized from early carbonatitic melts (Reguir et al., 2012; Giebel et al., 2019a, b). Arfvedsonite, aegirine and aegirine-augite occur both inside carbonatite II and at contact zones (Figs. 5 and 6) as euhedral-subhedral crystals and are compositionally distinct from those found in nordmarkite (Figs. S5

and S6), suggesting that these three silicates are not entrained from surrounding nordmarkite. Thus, we suggest that these minerals formed similar to Phl-II (see above) by the interaction between carbonatitic melt and nordmarkite.

The Cal-I-, Phl-I- and riebeckite-bearing carbonatite I exhibits equiangular texture with the lowest REE contents, LREE/HREE ratios and near-chondritic Y/Ho values (Figs. 7 and 10). Both petrographic features and chemical compositions of carbonatite I samples are consistent with those in primary carbonatites that are confirmed to derive from early carbonatite melt, such as Kalkfeld, Namibia, Homa Moutain, Kenya and Lackner Lake, Canada (Bühn et al., 2001; Chakhmouradian et al., 2016a). Therefore, the carbonatite I from the deep drill core (Fig. 3g) could be the best representation of initial carbonatites at Maoniuping. Such carbonatites should inherit their compositional signatures from early magma, showing enrichment of alkalis, fluorine and REEs (>3000 ppm) but relatively poor in SiO_2 (<5 wt.%), MgO (<0.5 wt.%), FeO (<1.0 wt.%) and especially in P_2O_5 (<0.5 wt.%).

Fractional crystallization of carbonatitic magma leading to REE enrichment

As discussed above, the four calcite generations are inferred to be of magmatic origin and carbonatites lack hydrothermal modification. Hence, it is feasible to trace magma evolution using the chemical characteristics of calcite, fluorite, phlogopite, and amphibole combined with the bulk chemistry of carbonatites. Although the major and trace element compositions of investigated samples cannot be used to diagnose

723 the composition of the parental silicate-carbonate magma, they can be invoked to test
724 carbonatitic evolution and degree of magma fractionation (Horning-Kjarsgaard, 1998;
725 Bühn et al., 2001; Chen & Simonetti, 2013; Chakhmouradian et al., 2016b; Su et al.,
726 2019; Anenburg et al., 2020b, 2022; Gao et al., 2021). To interpret their degree of
727 evolution, equilibrium and fractional (Rayleigh) crystallization were modelled and
728 represented in terms of La and Ce concentrations owing to their overwhelming
729 abundances compared to the other REEs (Pr–Lu). In our model calculations, partition
730 coefficients for La and Ce between calcite/fluorite and carbonatitic melt ($D^{REE}_{calcite/melt}$
731 and $D^{REE}_{fluorite/melt}$) were obtained from Chebotarev et al. (2019, 2021), determined by
732 experiments at 650−900 °C, whereas those for amphibole and carbonatitic melt
733 ($D^{REE}_{amphibole/melt}$) are from Bottazzi et al. (1999) and Reguir et al. (2012). Fractional
734 crystallization increments from F = 1.0 to 0.1 were employed with initial whole rock
735 compositions based on carbonatite I and appropriate calcite:amphibole:fluorite ratios
736 ranging from 0.9:0.1:0 to 0.85:0.05:0.1 based on observed mineral proportion from
737 carbonatite I and II. Results of the modal calculation for equilibrium and fractional
738 crystallization are illustrated in Fig. 14. In general, both differentiation models can
739 effectively facilitate enrichment of REE due to $D^{REE}_{calcite/melt}$ values less than unity
740 (Chebotarev et al., 2019, 2021). However, calcite crystallized from equilibrium
741 crystallization would have a slow increase in La and Ce — that is, enrichment in
742 equivalent REE contents through equilibrium crystallization requires higher degrees
743 of magma fractionation compared to Rayleigh crystallization (Fig. 14a and b). In

addition, the equilibrium model does not reconcile adequately with the measured La and Ce concentrations, as a significantly higher degree of magma fractionation (F = ~0.1) could not produce compositions extending into the higher ranges of La and Ce concentrations (up to 300 and 1200 ppm, respectively) (Fig. 14a). Modifying the proportions of calcite, amphibole and fluorite would yield similar results (F >0.85 for enrichment in La and Ce in Cal-III), indicating crystallization of amphibole and fluorite have no prominent effect on LREE enrichment during carbonatitic magma differentiation. In contrast, the calculated results for the Rayleigh fractional crystallization model not only overlap the measured data well, but display a near-linear positive correlation in which Ce rapidly enriches with La contents with the degree of fractional crystallization ranging from F = 0.95 to 0.4 (Fig. 14c and d). Of note, the choice of modal ratio (calcite:amphibole:fluorite = 0.9:0.1:0 to 0.85:0.05:0.1) or increasing fractional crystallization increments (ΔF = 10%, 5%, and 1%) cannot change the modal tendency between La and Ce contents, except increasing the enrichment rate of REE concentrations in residual melts (Fig. 14b−d). For instance, enrichment to 1200 ppm Ce and 600 ppm La in crystallizing Cal-III requires a significant degree of fractionation (F = ~0.8, ΔF = 1%, Fig. 16b), which is much greater than that modelled for intense fractionation with F = 0.5 to 0.6 at ΔF = 5% to 10% (Fig. 14c and d).

In general, REE-rich carbonatites are seemingly derived from more evolved melts (Chamouradian & Zaitzev, 2012; Walter et al., 2021; Anenburg et al., 2022) and

765 this has been suggested not only by experiments (Anenburg et al., 2020b; Chebotarev
766 et al., 2019, 2022), but in natural cases involving several African carbonatite
767 complexes (Bühn et al., 2001), Bayan Obo and Huayangchuan, China (Yang et al.,
768 2019; Gao et al., 2021), Kaiserstuhl, German (Walter et al., 2018, 2020; Giebel et al.,
769 2019b) and elsewhere. Our modal calculations suggest that with equilibrium
770 crystallization it is much more difficult to produce the extremely high La and Ce
771 contents in Cal-III at Maoniuping. Fractional crystallization, instead, is not only more
772 suitable for explaining the measured trace element data, but also consistent with the
773 textural evolution of calcites. Early REE-bearing phases (i.e., Cal-I, La = 85 ppm, Ce
774 = 240 ppm, F = 0.95) crystallized at deep levels would drive the residual melts toward
775 a composition saturated with REE-bearing phases (Cal-II, La = 190 ppm, Ce = 580
776 ppm, F = ~0.8), and consequently evolve to REE-rich and super coarse-grained
777 products (Cal-III, La = 340 ppm, Ce = 830 ppm; F = 0.5 to 0.6). Thus, it is plausible
778 that carbonatite II derived from rather residual carbonatite melt, causing its pegmatoid
779 texture. Systematic and continuous variations in major compositions (Fig. 9) and
780 positive correlation between La and Ce, $(La/Yb)_N$ and REE, from Cal-I to Cal-IV (Fig.
781 15), clearly demonstrate that both chemical evolution and REE enrichment can be
782 attributed to protracted fractional crystallization in an individual melt pulse. This is in
783 part because neither mixing by carbonatitic melt batches with counterpart silicate
784 melts nor multiple carbonatitic melt pulses could provide progressive variations in
785 investigated REE data, resulting in scattered, extended and even uncertainly

786 link-absent trends, as reported by experimental results (Foley et al., 2009) and natural
787 cases in the Oka (Chen & Simonetti, 2013) and Aley carbonatites (Chakhmouradian
788 et al., 2015).

789 Although intense fractional crystallization is able to generate the observed REE
790 enrichment in calcites and host carbonatites, our modal calculations indicate that
791 progressive calcite accumulation from carbonatitic melt can only yield constant
792 $(La/Yb)_N$ ratios between 15 and 18, conflicting significantly with steepening of REE
793 profiles and high $(La/Yb)_N$ values from 3.09 to 26.8 (Fig. 10a). Given low
794 $D^{HREE}_{calcite/melt}$ values (Ho–Lu from 0.05 to 0.07, Chebotarev et al., 2019) and
795 abundant proportions of amphibole, phlogopite and clinopyroxene in carbonatite II,
796 we suggest that increased $(La/Yb)_N$ ratios observed from Cal-I to Cal-III resulted from
797 silicate crystallization. Owing to their high distribution coefficients for HREE
798 (Chebotarev et al., 2021), their crystallization in early carbonatite melt could
799 sequestrate HREE and lead to an increase of $(La/Yb)_N$ in residual melt and derived
800 calcites (e.g., Cal-II and Cal-III). As a result, the positive correlation between
801 $(La/Yb)_N$ and REE concentrations is controlled by the relative proportions of calcite
802 and silicates during fractional crystallization of carbonatitic magma (Fig. 15b). Such
803 increased correlation between LREE-HREE fractionation and REE contents probably
804 occurs in P-poor carbonatitic system like Maoniuping, because early-crystalizing
805 apatite/monazite in P-rich systems leads to REE depletion during fractional
806 crystallization, resulting in REE-poor later-stage carbonatites (i.e., Magnet Cove,

USA; Prairie Lake, Canada; and Kerimasi, Tanzania; Miaoya, China; Fig. 15; Chakhmouradian et al., 2016b). Additionally, the discernable relationship between redox-sensitive element pairs, including a decrease in δCe with constant unity of δEu from Cal-I to Cal-III, clearly supports an increase in O_2 fugacity (fO_2) during magma fractionation (Fig. 15a and d), similar to global carbonatites, such as Palabora (Horning-Kjarsgaard, 1988; Giebel et al., 2017) and Aley (Chakhmouradian et al., 2015).

Sr–C isotope decoupling and REE mineralization during contamination by silicate wall rocks

The Maoniuping carbonatites have been interpreted to originate from fertile sub-continental lithospheric mantle (SCLM, Hou et al., 2015), according to consistently high whole-rock $^{87}Sr/^{86}Sr$ ratios (>0.7055) and mantle-like $\delta^{13}C$–$\delta^{18}O$ values (–6.6‰ to –7.0‰ and 6.7‰ to 8.4‰) (Wang et al., 2001; Xu et al., 2003; Hou et al., 2006; Liu & Hou, 2017). However, our in-situ isotopic measurements for four generations of calcite from carbonatite I and carbonatite II provide different constraints on evolution, not only from radiogenic Sr, but from stable C isotopic composition. The in-situ Sr-C isotopic variations indicate that the earlier-crystalizing Cal-I and Cal-II have low $^{87}Sr/^{86}Sr$ ratios (mean = 0.70613 and 0.70617) but relatively high $\delta^{13}C$ values (mean = –5.55 ‰ and –6.26 ‰), whereas Cal-III and Cal-IV are enriched in $^{87}Sr/^{86}Sr$ ratios (up to 0.70670 and 0.70660) and have a greater depletion

828 in $\delta^{13}C$ (drop to –9.97 ‰ and –8.61 ‰) (Tables. 3 and 4). Theoretically, the variable
829 Sr isotopic composition in Cal-III and Cal-IV could be caused by either hydrothermal
830 reworking, external fluid addition, or contamination with wall-rock. However,
831 hydrothermal reworking can be ruled out as there is little compositional and
832 petrological evidence for fluid overprinting both in our observations and previous
833 studies at Maoniuping (see above and Xie et al., 2015, Liu & Hou, 2017; Zheng & Liu,
834 2019). External fluid addition (e.g., by meteoric water or subduction-related fluids)
835 could lead to Sr isotopic re-equilibration (Ying et al., 2020; Wei et al., 2022), but it is
836 also expected to cause textural re-equilibration of calcite grains and wide chemical
837 variation, especially in Y/Ho ratios (18.4–46.2), extreme depletion in Eu (δEu drops
838 to 0.3) and low Sr contents (Chakhmouradian, 2016b). However, none of these
839 features are observed in any of the studied calcite generations and hence, external
840 fluid addition is unlikely at Maoniuping. In contrast, contamination with silicate
841 wall-rock (nordmarkite) during carbonatitic magma ascent is most likely the essential
842 factor in variable Sr isotopic composition (Fig. 13). Under this scenario, the high
843 $^{87}Sr/^{86}Sr$ ratios in Cal-III and Cal-IV require a more radiogenic Sr source. Considering
844 that both nordmarkite counterparts and wall-rock feldspars are capable of
845 incorporating significant levels of radiogenic Sr ($^{87}Sr/^{86}Sr$ ratios = 0.70638–0.70686
846 and 0.70704, respectively, Xu et al., 2003; Hou et al., 2006; Liu & Hou, 2017) and
847 hence, they are likely contributors to the variable $^{87}Sr/^{86}Sr$ ratios. This is also
848 supported by petrographic evidence of metasomatic microcline in carbonatite II at the

849 contact zones (Fig. 6a), and is similar to the situation reported in some well-studied
850 carbonatites, such as Caotan in China (Wei et al., 2020), Nolans Bore in Australia
851 (Anenburg et al., 2020a), Blue River in Canada (Mitchell et al., 2017), Vuoriyarvi in
852 Russia (Fomina & Kozlov, 2021), Kaiserstuhl in Germany (Walter et al., 2018; Giebel
853 et al., 2019b), Kieshöhe and Gross Brukkaros in Namibia (Walter et al., 2022, 2023).
854 Contamination by nordmarkite cannot be identified easily by bulk Sr–Nd–Pb
855 isotopic compositions because their much higher elemental concentrations in
856 carbonatites would buffer against change in the isotope systems during contamination
857 with silicate rocks (Bell & Tilton, 2002). However, our in-situ Sr–C isotopic data can
858 be used to track the processes of contamination by more radiogenic Sr isotopic
859 composition in Cal-III and Cal-IV relative to early-crystalizing Cal-I and Cal-II. To
860 explain the level of contamination responsible for the mixed Sr isotopic compositions,
861 a Monte Carlo simulation has been conducted by assuming that initial $^{87}Sr/^{86}Sr$ ratios
862 are 0.70605 for carbonatite according to our analyses of Cal-I and 0.70686–0.70700
863 for nordmarkite (Xu et al., 2003; Hou et al., 2006). Based on whole-rock results of our
864 and previous studies, Sr contents are selected from 8000 to 25000 ppm for
865 carbonatites (Hou et al., 2015) and 500 to 3000 ppm for nordmarkite (Wang et al.,
866 2001), with initial REE contents of 1000 to 3000 ppm (Wang et al., 2001; Hou et al.,
867 2006) and 200 to 800 ppm (Xu et al., 2003; Hou et al., 2015) for carbonatite and
868 nordmarkite, respectively. A total of 4×10^8 simulations were performed by randomly
869 selecting input values from the defined parameters. In the modal calculation (Fig. 16),

a schematic trend in $^{87}Sr/^{86}Sr$ ratios relative to Sr and REE contents (Fig. 17a) illustrates that as much as 40% (± 10%) of the Sr isotopic budget of Cal-III- and Cal-IV-bearing carbonatite was contributed by wall-rock nordmarkite.

Coupled with increased $^{87}Sr/^{86}Sr$ ratios, in-situ C isotopic compositions display discriminable variation in which initial high $\delta^{13}C$ values of early-crystalizing Cal-I (~ 5.5‰) largely dropped to low $\delta^{13}C$ values in Cal-III and Cal-IV (up to –9.9‰ and –8.7‰, respectively, Fig. 17d). Theoretically, the excursion in in-situ C isotopic composition could be induced by fractional crystallization of magma, addition of sedimentary carbonate or meteoric fluids, or interaction between carbonatitic magma and wall rocks (Deines, 1992; Santos & Clayton, 1995; Ray et al., 1999). Since fractional crystallization of magma, addition of sedimentary carbonate or meteoric fluids would result in a positive shift in $\delta^{13}C$ (Santos & Clayton, 1995; Chazot et al., 2003; Ray & Ramesh, 2000), these three hypotheses do not reconcile the lowering of $\delta^{13}C$ values measured in Cal-III and Cal-IV (Fig. 17b). By contrast, contamination via interaction between carbonatitic melt and wall rocks is probably the reason for C isotope deficiency in Cal-III and Cal-IV, because C isotopic composition would change as a result of decarbonation reactions and re-equilibration between carbonatitic melt and CO_2 by the following reactions:

Carbonatite melt + Quartz (*nordmarkite*) → Aegirine + Calcite + CO_2 (*fluid/gas*)

$$CaFe(CO_3)_2 + 0.5Na_2CO_3 + 0.25O_2 + 2SiO_2 = NaFeSi_2O_6 + CaCO_3 + 1.5CO_2$$

(reaction 1)

Carbonatite melt + Quartz (*nordmarkite*) → Magnesioarfvedsonite + Calcite + CO_2 (*gas/fluid*) + O_2 (*gas*)

$5CaFe(CO_3)_2 + 4CaMg(CO_3)_2 + 1.5Na_2CO_3 + H_2O + 8SiO_2 = Na(Na,Ca)_2(Mg,Fe)_4FeSi_8O_{22}(OH)_2 + 7CaCO_3 + 12.5CO_2 + 2.75O_2$

(reaction 2)

Carbonatite melt + K-feldspar (*nordmarkite*) → Phlogopite + Calcite + CO_2 (*fluid/gas*)

$3Ca(Mg,Fe)(CO_3)_2 + H_2O + KAlSi_3O_8 = K(Mg, Fe)_3AlSi_3O_{10}(OH)_2 + 3CaCO_3 + 3CO_2$

(reaction 3)

Contamination-induced interaction between carbonatite melts and silicate rocks could trigger reactions 1–3. Similar modification of silicate rocks by carbonatitic melts has been referred as "antiskarn" metasomatism (Anenburg & Mavrogenes, 2018) and reflects mutual interaction during contamination. The Na_2CO_3 and H_2O components in carbonatite melt at Maoniuping are supported by sodium-carbonate and water-bearing melt and melt-fluid inclusions in calcite and fluorite (Xie et al., 2009; Zheng et al., 2019). Both soluble components, together with $CaFe(CO_3)_2$ and $Ca(Mg,Fe)(CO_3)_2$ in carbonatite melt, react with SiO_2 and $KAlSi_3O_8$ of silicate wall rocks to control the formation of aegirine and aegirine-augite, magnesioarfvedsonite, phlogopite, and calcite. The chemical classification of arfvedsonite, aegirine, and aegirine-augite show that they are similar to those of other carbonatites worldwide

912 (Smith, 2007; Reguir et al., 2012). Their compositional evolution exhibits
913 progressively enrichment in Ca and Mg from carbonatite I to contact zone and
914 carbonatite II (Figs. S6 and S7), indicating that prolonged contamination by silicate
915 wall rocks lead to removal of Ca and Mg from the carbonatite system by formation of
916 magnesioarfvedsonite, aegirine-augite, and calcite (reactions 1–2). Moreover,
917 carbonatite melt would obtain Si and Al from silicate wall rocks and further expel
918 soluble components of Na, K and F (reaction 3) as evident not only by higher Na and
919 IV (F) values (Fig. 11g and i) but K-rich core and Al-rich rim (Fig. S5) in Phl-II.
920 Previous experiments showed that alkalis and fluorine are crucial ligands that can
921 bond to REE as alkali-REE and fluorine-REE complexes and allow long-distances
922 mobilization in carbonatite systems (Song et al., 2016; Chebotarev et al., 2019;
923 Anenburg et al., 2020b); and the soluble alkali carbonate (Na_2CO_3) in carbonatite melt
924 can significantly promote REE solubility under magmatic-hydrothermal conditions
925 (Anenburg et al., 2020b). Thus, it is plausible that both Na_2CO_3 consumption and
926 formation of abundant aegirine, aegirine-augite, arfvedsonite and phlogopite by
927 reactions 1–3 at Maoniuping serve to scavenge Na, K, and F from carbonatite melt,
928 which could destabilize alkali-REE and fluorine-REE complexes and thus probably
929 inhibit REE mobility and lead to accumulation not only in produced calcite (Cal-III
930 and Cal-IV) coupled with $\delta^{13}C$ depletion (Fig. 17c), but also as bastnäsite-(Ce)
931 intergrown with fluorite and silicate minerals in carbonatite II and the contact zone
932 (Figs. 5 and 6).

In addition, reactions 1–3 would contemporaneously cause strong decarbonation, which would preferentially remove ^{13}C from carbonatitic melt by release of CO_2 (Chacko et al., 1991) and contribute to low $\delta^{13}C$ values in residual carbonatitic melts and their derived calcites (Fig. 17d). Therefore, the gradual depletion $\delta^{13}C$ values from Cal-I to Cal-III and Cal-IV, combined with increases of $^{87}Sr/^{86}Sr$ (Fig. 17b), robustly demonstrate protracted contamination by interaction with wall rocks during carbonatite melt ascent. The processes of decarbonation are delineated by experiments (Chacko et al., 2001; Anenburg & Mavrogenes, 2018) and can be quantified using the equation for Raleigh volatilization (Valley, 1986): $\delta_f = \delta_i + 1000 \times (F^{(\alpha-1)} - 1)$, where F is the C fraction remaining in the carbonatitic melt, and δ_f and δ_i are the final and initial $\delta^{13}C$ values. The fractionation factor α between calcite and CO_2 was calculated by the experimental equation of Scheele and Hoefs (1992): $10^3 \ln\alpha_{calcite\text{-}CO_2} = -3.46 \times 10^6/T^2 + 9.58 \times 10^3/T - 2.72$. Assuming that $\delta^{13}C$ values of –5.5‰ (Cal-I) and –7.5‰ (Cal-III) represent the initial and final C isotopic compositions, respectively, and reaction temperatures are estimated at 500–800 °C based on melt and fluid inclusion microthermometry, the fraction of carbon remaining in reaction zones (F) is calculated to be ~0.67 (Fig. 17f), indicating that as much as ~35% of initial CO_2 could be degassed in contact zones due to carbonatite melt-nordmakite interaction. As the degassed CO_2 would not readily disperse but could be retained in the magma (Harmer & Gittins; 1997; Russell et al., 2012), Walter et al. (2021) proposed the concept that CO_2 release from decompressive immiscibility

954 of carbonatitic fluids could promote fracturing and drive carbonatite magma ascent.
955 Equally, decarbonation of CO_2 by carbonatite melt-wall rock interaction and their
956 retention in carbonatite melt would act as a positive mechanism of increasing
957 buoyancy and drive magma rapid ascent. Contamination-induced CO_2 degassing
958 would also lead to volumetric expansion and fracturing through the generation of
959 over-pressures (Weidendorfer et al., 2019; Water et al., 2020, 2021). As a result,
960 continual contamination during carbonatite magma ascent is inferred to trigger
961 volumetric expansion, leading to fracturing and conduit formation for super
962 coarse-grained carbonatite II and simultaneously result in strain-induced, dynamic
963 decomposition of carbonatite II (e.g., miarolitic and porous textures with undulatory
964 extinction and elongated calcite crystals Figs. 3k and 5i) and brecciation events both
965 at Maoniuping (see Fig. 6 in Liu et al., 2019a) and in most carbonatites worldwide
966 (Smith et al., 2007; Elliott et al., 2018).
967
968 **A general model for REE enrichment and mineralization in carbonatites**
969 Most known carbonatite-related REE deposits are closely associated with
970 metasomatized mantle carbonatite sources, with influence on REE mineralization
971 from magmatic evolution, and hydrothermal activity (Chamouradian & Zaitzev, 2012;
972 Smith et al., 2016; Anenburg et al., 2022). Numerous studies have contended that
973 metasomatized carbonatite sources influenced by subducted slab and including
974 components of recycled sediments contribute to the generation of initial REE-fertile

carbonatites (Hou et al., 2015; Xu et al., 2017; Çimen et al., 2018; Yaxely et al., 2022). Subsequent late-stage hydrothermal reworking on such fertile carbonatites might be responsible for REE mineralization in a number of deposits, including the Miaoya, Cummins Range, and Bayan Obo carbonatites (Kynický et al. 2012; Smith et al., 2015; Downes et al., 2016; Ying et al., 2020; Anenburg et al., 2022). Nevertheless, in a global context, models for carbonatitic magma evolution and its impact on REE mineralization are rare (Smith et al., 2016). REE accumulation caused by fractional crystallization (Bayan Obo, China, Yang et al., 2019) and by contamination linked to occurrence of mica and apatite (Kaiserstuhl, Germany, Giebel et al., 2019b) have been inferred. However, the combination of different processes and their functions with regards to REE enrichment and mineralization for the formation of carbonatite-related REE deposits has not been examined in an integrated model.

In the case of Maoniuping, it is believed that mantle source became enriched in REE by recycling of Neoproterozoic subducted marine sediments (Hou et al., 2015). The Maoniuping carbonatites were likely derived from the fertile mantle source in the Cenozoic (Hou et al., 2015; Liu et al., 2019a; Weng et al., 2022b) and experienced further REE accumulation by magma evolution. Here, we reconcile petrographic and geochemical data to propose a conceptual model for the REE enrichment and mineralization during carbonatite magma evolution involving fractional crystallization and contamination by silicate rocks (Fig. 18).

995 Initially a fertile carbonatite melt was derived from carbonate-silicate magma by
996 liquid immiscibility which probably occurred at shallow-level crustal level as
997 evidenced by low MgO contents, low (Mg+Fe)/Ca and petrographic evidence of Cal-I
998 and carbonatite I. Extremely low viscosities of carbonatitic melts enable them to
999 ascend rapidly (Jones et al., 2013; Kono et al., 2014). Owing to the lower density of
1000 carbonatitic melt (<2400 kg/m^3, Jones et al., 2013; Massuyeau et al., 2023) than
1001 syenitic melts (~2500 kg/m^3, Semenov & Polyansky, 2017), the initial carbonatite
1002 melt may be suspended in or surrounded by silicate melts, which could prevent
1003 carbonatitic melt from reacting immediately with basement rocks (Fig. 18a). When
1004 reaching liquidus temperatures (e.g., >900°C, Panina, 2005; Guzmics et al., 2011), the
1005 first-order carbonate phases (e.g., Cal-I) began to crystallize, with precipitation of
1006 minor, primary phlogopite (Phl-I) and riebeckite at a low degree of fractional
1007 crystallization (F = ~ 0.95–0.90) of carbonatite melt. These phases are expected to
1008 inherit the compositional characteristics of the initial carbonatitic melt, as indicated by
1009 the lowest REE contents (~800 ppm), low (La/Yb) ratios (~3.1), and primary Sr–C
1010 isotopic composition ($^{87}Sr/^{86}Sr$ = 0.70613 and $\delta^{13}C$ = –5.5‰) (Fig. 18b1).
1011 Considering the high incompatibility of alkalis, REE and halogens (Chebotarev et al.,
1012 2019), calcite accumulation drove increased REE concentrations in residual melts and
1013 crystallization of alkali-bearing and REE-rich Cal-II and slightly enhanced formation
1014 of halogen-bearing phlogopite (Phl-I). The gradually increasing alkali and volatile
1015 contents and decompression, in turn, lowered the viscosities of carbonatitic melt

1016 which ascended faster relative to silicate counterparts (Walter et al., 2021; Massuyeau
1017 et al., 2023) as recorded by the low-strain texture in Cal-II (Fig. 18b2).

1018 While ascending to higher crustal levels, further fractional crystallization (F =
1019 0.7–0.8) of carbonatitic melt derived carbonate cumulates lead to enrichment of
1020 alkaline, volatile, and REE components in residual melts. At the same time,
1021 contamination with silicate rock via metasomatic "antiskarn" interactions between hot
1022 carbonatitic melt (>600 ℃, Xie et al., 2009) and silicate rocks occurred. Such
1023 interactions caused incorporation of more radiogenic Sr from host rocks, and lowered
1024 C isotopic ratios through decarbonation reactions. This triggered the formation of
1025 phlogopite, aegirine and aegirine-augite, and magnesioarfvedsonite inside
1026 carbonatites by a series of reactions between dissolved carbonates of Na_2CO_3, K_2CO_3,
1027 and $Ca(Mg,Fe)(CO_3)_2$ and SiO_2 and Al_2O_3 from silicate rocks (Fig. 18c). The CO_2
1028 generated by decarbonation reactions would not release instantaneously but be
1029 retained in carbonatitic melt, causing the development of overpressures, which drove
1030 a jet-like ascent (Fig. 18a; Walter et al., 2021). More importantly, wallrock
1031 contamination resulted in REE accumulation and mineralization, as evident by a
1032 significant proportion of bastnäsite-(Ce) with calcite (Cal-III and Cal-IV) that contain
1033 highest REE concentrations (Fig. 6). Magmatic and magmatic-hydrothermal transport
1034 of the REE has been demonstrated to be as complexes with a wide range of ligands
1035 including F^-, Cl^-, CO_3^{2-}, PO_4^{3-} and SO_4^{2-} (Migdisov et al., 2016), with F^- and PO_4^{3-}
1036 specifically acting as depositional ligands in hydrothermal systems (Williams-Jones et

al., 2012). Formation of fluorine-bearing silicates and fluorite could destabilize halogenated REE complexes in the melt, resulting in REE precipitation as bastnäsite-(Ce). Similarly, Anenburg et al. (2020b) demonstrated that alkalis were critical in magmatic-hydrothermal REE transport, although specific complexes have not yet been identified. Si and Al contributions from wall rocks and consumption of K and Na by contamination-triggered formation of alkali silicates may have resulted in reduced REE solubility, and then formation of bastnäsite-(Ce) (Fig. 18b3).

As carbonatitic melt ascended, pronounced factional crystallization of carbonatite melt (F = 0.5–0.6) lead to REE enrichment to significant levels, accompanied by calcite cumulates with pegmatoid texture and super large crystals (carbonatite II). Continuous contamination admixed radiogenic Sr and lowered $\delta^{13}C$ isotope values ($\delta^{13}C$ = –7.5‰ and $^{87}Sr/^{86}Sr$ ratios up to 0.70660) by further interaction and decarbonation CO_2. These CO_2 releases leads to vigorous volumetric expansion that triggers the ubiquitous brecciation observed at Maoniuping, and likely affected calcites so that they exhibit stain-induced deformation, such as bent and segmented thick twinning lamellae in Cal-III (Fig. 18b4). Moreover, repeated interaction between REE-rich carbonatite melts and silicate rocks scavenge more alkalis and volatiles, and triggered formation of a large proportion of the bastnäsite-(Ce), fluorites, baryte, and alkaline silicates (Fig. 18b4). The case studies cited above indicate that this may be a widespread mechanism in P-poor carbonatites.

CONCLUSIONS

The Maoniuping carbonatite-related REE deposit in the southwestern China is characterized by medium- to coarse-grained carbonatites in the lower part of drill core, which transition gradually upward into super coarser-grained carbonatite with pegmatoidal texture. Four well-defined generations of calcite and compositional variation of phlogopite, amphibole and clinopyroxene in two types of carbonatites show a systematic increase of REE contents, but progressively decoupled Sr–C isotopic compositions. Based on petrographic observations and geochemical data, we interpret the pronounced REE enrichment in Maoniuping carbonatites as a result of protracted fractional crystallization of carbonatite magma, whereas more radiogenic Sr and gradually depleted C isotopic compositions are attributed to interaction with silicate rocks and decarbonation of CO_2 loss. These new findings support an integrated model in which REE mineralization could be triggered by contamination-induced interaction between carbonatitic melt and silicate rocks. From this study, we propose that magmatic processes may play a more important role in REE enrichment and mineralization than previously recognized in carbonatites worldwide, which could be a significantly factor in the formation of giant carbonatite-related REE deposits.

ACKNOWLEDGEMENTS

We thank Drs. Di Zhang, Yuan-can Ying, Ju Lu and Zhi-yao Zeng for their assistance during analyses. Wei Chen is acknowledged for insightful discussions on various topics related to this study. We are particularly grateful to Benjamin Walter, Johannes Giebel, Allen Andersen, and editor Andreas Audétat for their kindly reviews, constructive comments and suggestions that improve this manuscript significantly.

FUNDING

This work is financially supported by the National Natural Science Foundation of China (Gran No. 92162216), the Second Tibetan Plateau Scientific Expedition and Research (2021QZKK0304), National Natural Science Foundation of China (Gran No. 42202093), and China Geological Survey Program of the China Geological Survey, Ministry of Natural Resources (Grant DD 20221649). MS acknowledges support from NERC Global Partnerships (Grant NE/V008935/1).

REFERENCES

Andersen, A. K., Clark, J. G., Larson, P. B. & Neill, O. K. (2016). Mineral chemistry and petrogenesis of a HFSE (+HREE) occurrence, peripheral to carbonatites of the Bear Lodge alkaline complex, Wyoming. American Mineralogist 101, 1604–1623.

Anenburg, M. & Mavrogenes, J. A. (2018). Carbonatitic versus hydrothermal origin for fluorapatite REE-Th deposits: Experimental study of REE transport and crustal “antiskarn” metasomatism. American Journal of Science 318, 335–366.

Anenburg, M., Broom-Fendley, S. & Chen, W. (2022). Formation of Rare Earth Deposits in Carbonatites. Element 17, 327–332.

Anenburg, M., Mavrogenes, J. A., & Bennett, V. C. (2020a). The fluorapatite P–REE–Th vein deposit at Nolans Bore: genesis by carbonatite metasomatism. Journal of Petrology 61, egaa003.

Anenburg, M., Mavrogenes, J. A., Frigo, C. & Wall, F. (2020b). Rare earth element mobility in and around carbonatites controlled by sodium, potassium and silica. Science Advances 41, 6570.

Barker, D. S. (2001). Calculated silica activities in carbonatite liquids. Contributions to Mineralogy and Petrology 141, 704–709.

Bau, M. (1996). Controls on the fractionation of isovalent trace elements in magmatic and aqueous systems: evidence from Y/Ho, Zr/Hf, and lanthanide tetrad effect. Contributions to Mineralogy and Petrology 123, 323–333.

Bell, K. & Tilton, G. R. (2002). Probing the mantle: the story from carbonatites. Eos, Transactions American Geophysical Union 83, 273–277.

Bizzarro, M., Simonetti, A., Stevenson, R. K. & Kurszlaukis, S. (2003). In situ $^{87}Sr/^{86}Sr$ investigation of igneous apatites and carbonates using laser-ablation MC-ICP-MS: Geochimica et Cosmochimica Acta 67, 289– 302.

Bottazzi, P., Tiepolo, M., Vannucci, R., Zanetti, A., Brumm, R., Foley, S.F. & Oberti, R. (1999). Distinct site preferences for heavy and light REE in amphibole and the prediction of Amph/LDREE. Contributions to Mineralogy and Petrology 137, 36–45.

Bouabdellah, M., Boukirou, W., Jébrak, M., Bigot, F., Yans, J., Mouttaqi, A., El Gadarri, M., Errami, A., & Levresse, G. (2022). Discovery of antiskarn-hosted strategic metal mineralization in the Upper Cretaceous Twihinate carbonatite intrusion (West African Craton Margin, Moroccan Sahara). Ore Geology Reviews 149, 105105.

Bühn, B. (2008). The role of the volatile phase for REE and Y fractionation in low-silica carbonate magmas: implications from natural carbonatites, Namibia. Mineralogy and Petrology 92, 453–470

Bühn, B., Wall, F. & Le Bas, M. J. (2001). Rare-earth element systematics of carbonatitic fluorapatites, and their significance for carbonatite magma evolution. Contributions to Mineralogy and Petrology 141, 572–591.

Castor, S. B. (2008). The Mountian Pass rare-earth carbonatite and associated ultrapotassic rocks, California. The Canadian Mineralogist 46, 779–806.

Chacko, T., Mayeda, T. K., Clayton, R. N. & Goldsmith, J. R. (1991). Oxygen and carbon isotope fractionations between CO2 and calcite. Geochimica et Cosmochimica Acta 55, 2867–2882.

Chacko, T., Cole, D. R. & Horita, J. (2001). Equilibrium oxygen, hydrogen, and carbon isotope fractionation factors applicable to geologic systems. Reviews in Mineralogy and Geochemistry 43, 1–81.

Chazot, G., Bertrand, H., Mergoil, J. & Sheppard, S. M. F. (2003). Mingling of immiscible dolomite carbonatite and trachyte in tuffs from the Massif Central, France. Journal of Petrology 44, 1917–1936.

1144 Chakhmouradian, A. R. & Wall, F. (2012). Rare Earth Elements: Minerals, Mines,
1145 Magnets (and More). Elements, 8, 333–340.
1146 Chakhmouradian, A. R. & Zaitsev, A. N. (2012). Rare Earth Mineralization in Igneous
1147 Rocks: Sources and Processes. Elements 8, 347–353.
1148 Chakhmouradian, A. R., Reguir, E. P. & Zaitsev, A. N. (2016a). Calcite and dolomite
1149 in intrusive carbonatites. I. Textural variations. Mineralogy and Petrology 110,
1150 333–360.
1151 Chakhmouradian, A. R., Reguir, E. P., Couëslan, C. & Yang, P. (2016b). Calcite and
1152 dolomite in intrusive carbonatites. II. Trace-element variations. Mineralogy and
1153 Petrology 110, 361–377.
1154 Chakhmouradian, A. R., Reguir, E. P., Zaitsev, A. N., Couëslan, C., Xu, C., Kynický,
1155 J., Mumin A. H. & Yang, P. (2017). Apatite in carbonatitic rocks: Compositional
1156 variation, zoning, element partitioning and petrogenetic significance. Lithos
1157 274-275, 188–213.
1158 Chakhmouradian, A. R., Reguir, E. P., Kressall, R. D., Crozier, J., Pisiak, L. K., Sidhu,
1159 R. & Yang, P. (2015). Carbonatite-hosted niobium deposit at Aley, northern
1160 British Columbia (Canada): Mineralogy, geochemistry and petrogenesis. Ore
1161 Geology Reviews 64, 642–666.
1162 Chebotarev, D. A., Veksler, I. V., Wohlgemuth-Ueberwasser, C., Doroshkevich, A. G.
1163 & Koch-Müller, M. (2019). Experimental study of trace element distribution
1164 between calcite, fluorite and carbonatitic melt in the system
1165 $CaCO_3 + CaF_2 + Na_2CO_3 \pm Ca_3(PO_4)_2$ at 100 MPa. Contributions to Mineralogy
1166 and Petrology 171, 4.
1167 Chebotarev, D. A., Wohlgemuth-Ueberwasser, C. & Hou, T. (2022). Partitioning of
1168 REE between calcite and carbonatitic melt containing P, S, Si at 650–900 °C and
1169 100 MPa. Scientific Reports 12, 3320.
1170 Chen, L., Liu, Y. S., Hu, Z. C., Gao, S., Zong, K. Q. & Chen, H. H. (2011). Accurate
1171 determinations of fifty-four major and trace elements in carbonate by LA–
1172 ICP-MS using normalization strategy of bulk components as 100%. Chemical
1173 Geology 284, 283–295.
1174 Chen, W. & Simonetti, A. (2013). In-situ determination of major and trace elements in
1175 calcite and apatite, and U-Pb ages of apatite from the Oka carbonatite complex:
1176 Insights into a complex crystallization history. Chemical Geology 353, 151–172.
1177 Chen, W., Lu J., Jiang, S. Y., Ying, Y. C. & Liu, Y. S. (2018). Radiogenic Pb reservoir
1178 contributes to the rare earth element (REE) enrichment in South Qinling
1179 carbonatites. Chemical Geology 494, 80–95.
1180 Chen, W., Lu, J., Jiang, S. Y., Zhao, K. D. & Duan, D. F. (2017). In situ carbon
1181 isotope analysis by laser ablation MC-ICP-MS. Analytical Chemistry 89, 13145–
1182 13421.
1183 Chiaradia, M. & Caricchi, L. (2017). Stochastic modelling of deep magmatic controls
1184 on porphyry copper deposit endowment. Scientific Reports 7, 44523.

Chmyz, L., Azzone, R. G., & Ruberti, E. (2022). Olivines as probes into assimilation of silicate rocks by carbonatite magmas: unraveling the genesis of reaction rocks from the Jacupiranga alkaline-carbonatite complex, southern brazil. Lithos 416-417, 106647.

Çimen, O., Kuebler, C., Simonetti, S. S., Corcoran, L., Mitchell, R. & Simonetti, A. (2019). Combined boron, radiogenic (Nd, Pb, Sr), stable (C, O) isotopic and geochemical investigations of carbonatites from the Blue River Region, British Columbia (Canada): Implications for mantle sources and recycling of crustal carbon. Chemical Geology 529, 119240.

Deines, P. (1992). Mantle carbon: concentration, mode of occurrence and isotope composition. In: Shidlowski, M., Golubic, S., Kimberley, M.M., McKirdy, D.M., Trudinger, P.A. (Eds.), Early Organic Evolution: Implications for Mineral and Energy Resources. Springer Verlag, Berlin, pp. 133–146.

Deng, J., Wang, Q. F., Gao, L., He, W. Y., Yang, Z. Y., Zhang, S. H., Li, G. J., Sun, X. & Zhou, D. Q. (2021). Differential crustal rotation and its control on giant ore clusters along the eastern margin of Tibet. Geology 49, 428–432.

Deng, J., Wang, Q. F., Li, G. J. & Santosh, M. (2014). Cenozoic tectonomagmatic and metallogenic processes in the Sanjiang region, southwestern China. Earth-Science Reviews 138, 268–299.

Downes, P. J., Demény, A., Czuppon, G., Jaques, A. L., Verrall, M., Sweetapple, M., Adams, D., McNaughton, N. J., Gwalani, L. G. & Griffin, B. J. (2014). Stable H-C-O isotope and trace element geochemistry of the Cummins Range Carbonatite Complex, Kimberley region, Western Australia: implications for hydrothermal REE mineralization, carbonatite evolution and mantle source regions. Mineralium Deposita 49, 905–932.

Elliott, H. A. L., Wall, F., Chakhmouradian, A. R., Siegfried, P. R., Dahlgren, S., Weatherley, S., Finch, A. A., Marks, M. A. W., Dowman, E. & Deady, E. (2018). Fenites associated with carbonatite complexes: A review. Ore Geology Reviews 93, 38–59.

Fan, H. R., Niu, H. C., Li, X. C., Yang, K. F., Yang, Z. F. & Wang, Q. W. (2020). The types, ore genesis and resource perspective of endogenic REE deposits in China. Chinese Science Bull 65, 3778–3793 (In Chinese with English abstract).

Foley, S. F., Yaxley, G. M., Rosenthal, A., Buhre, S., Kiseeva, E. S., Rapp, R. P. & Jacob, D. E. (2009). The composition of near-solidus melts of peridotite in the presence of CO_2 and H_2O between 40 and 60 kbar. Lithos 112, 274–283.

Fomina, E. N. & Kozlov, E. N. (2021). Stable (C, O) and radiogenic (Sr, Nd) isotopic evidence for REE-carbonatite formation processes in Petyayan-Vara (Vuoriyarvi massif, NW Russia). Lithos 398–399, 106282.

Foster, M. D. (1960). Interpretation of the composition of trioctahedral micas. U.S. Geological Survey Professional Paper, 49.

Frost, B. R., Arculus, R. J., Barnes, C. G., Collins, W. J., Ellis, D. J. & Frost, C. D. (2001). A geochemical classification of granitic rock suites: Journal of Petrology 42, 2033–2048.

Gao, L.-G., Chen, Y.-W., Bi, X.-W., Gao, J.-F., Chen, W. T., Dong, S.-H., & Hu, R.-Z. (2021). Genesis of carbonatite and associated U–Nb–REE mineralization at Huayangchuan, central China: Insights from mineral paragenesis, chemical and Sr-Nd-C-O isotopic compositions of calcite. Ore Geology Reviews, 138, 104310.

Gao, Z. Y., Liu, Y., Jing, Y. T., Hou, Z. Q., Liu, H. C., Zheng, X. & Shen, N. P. (2021). Mineralogical characteristics and Sr–Nd–Pb isotopic compositions of banded REE ores in the Bayan Obo deposit, Inner Mongolia, China: Implications for their formation and origin. Ore Geology Reviews 139, 104492.

Giebel, R. J., Gauert, C. D. K., Marks, M. A. W., Costin, G. & Markl, G. (2017). Multi-stage formation of REE minerals in the Palabora Carbonatite Complex, South Africa. American Mineralogist 102, 1218–1233.

Giebel, R. J., Marks, M. A. W., Gauert, C. D. K. & Markl, G. (2019a). A model for the formation of carbonatite-phoscorite assemblages based on the compositional variation of mica and apatite from the Palabora Carbonatite Complex, South Africa. Lithos 324–325, 89–104.

Giebel, R. J., Parsapoor, A., Walter, B. F., Braunger, S., Marks, M. A. W., Wenzel, T. & Markl, G. (2019b). Evidence for magma – wall rock interaction in carbonatites from the Kaiserstuhl Volcanic Complex (Southwest Germany). Journal of Petrology 1–31.

Gittins, J. & Harmer, R. E. (1997). What is ferrocarbonatite? A revised classification. Journal of African Earth Sciences 25, 159–168.

Goodenough, K. M., Deady, E. A., Beard, C. D., Broom-Fendley, S., Elliott, H. A. L., van den Berg, F. & Öztürk, H. (2021). Carbonatites and Alkaline Igneous Rocks in Post-Collisional Settings: Storehouses of Rare Earth Elements. Journal of Earth Science 32, 1332–1358.

Guo, D. & Liu, Y. (2019). Occurrence and geochemistry of bastnäsite in carbonatite-related REE deposits, Mianning–Dechang REE belt, Sichuan Province, SW China. Ore Geology Reviews 107, 266–282.

Guzmics, T., Mitchell, R. H., Szabó, C., Berkesi, M., Milke, R. & Abart, R. (2011). Carbonatite melt inclusions in coexisting magnetite, apatite and monticellite in Kerimasi calciocarbonatite, Tanzania: melt evolution and petrogenesis. Contributions to Mineralogy and Petrology 161, 177–196.

Harmer, R. E. & Gittins, J. (1997). The origin of dolomitic carbonatites: field and experimental constraints. Journal of African Earth Sciences 25, 5–28.

Harper, F., Wiid, G., Siegfried, P., Brown, J., Hall, M., Njowa, G., Vivier, J., Zietsman, R., & Duke, V. (2015). National Instrument 43–101 Independent Technical Report on the Results of a Preliminary Feasibility Study on the Zandkopsdrift Rare Earth Element and Manganese by-Product Project in the Northern Cape

Province of South Africa Independent Pre-Feasibility Study Prepared for Frontier Rare Earths, Limited, Venmyn Deloitte, pp 226.

Hornig-Kjarsgaard, I. (1998). Rare earth elements in sovitic carbonatites and their mineral phases. Journal of Petrology 39, 2105–2121.

Hou, Z. Q. & Cook, N. J. (2009). Metallogenesis of the Tibetan collisional orogen: a review and introduction to the special issue. Ore Geology Reviews 36, 2–24.

Hou, Z. Q., Liu, Y., Tian, S. H., Yang, Z. M. & Xie, Y. L. (2015). Formation of carbonatite-related giant rare-earth-element deposits by the recycling of marine sediments. Scientific Reports 5, 10231.

Hou, Z. Q., Tian, S. H., Yuan, Z. X., Xie, Y. L., Yin, S. P., Yi, L. S., Fei, H. C. & Yang, Z. M. (2006). The Himalayan collision zone carbonatites in western Sichuan, SW China: petrogenesis, mantle source and tectonic implication. Earth and Planetary Science Letters 244, 234–250.

Irber W. (1999) The lanthanide tetrad effect and its correlation with K/Rb, Eu/Eu*, Sr/Eu, Y/Ho, and Zr/Hf of evolving peraluminous granite suites. Geochimica et Cosmochimica Acta 63, 489–508

Jaireth, S., Hoatson, D. M. & Miezitis, Y. (2014). Geological setting and resources of the major rare-earth-element deposits in Australia. Ore Geology Reviews 62, 72–128.

Jochum, K. P., Nohl, U., Herwig, K., Lammel, E., Stoll, B., & Hofmann, A. W. (2005). GeoReM: A New Geochemical Database for Reference Materials and Isotopic Standards. Geostandards and Geoanalytical Research 29, 333–338.

Jones, A. P., Genge, M. & Carmody, L. (2013). Carbonate melts and carbonatites. Reviews in Mineralogy and Geochemistry 75, 289–322.

Kono, Y., Kenney-Benson, C., Hummer, D., Ohfuji, H., Park, C., Shen, G., Wang, Y., Kavner, A. & Manning, C. E. (2014). Ultralow viscosity of carbonate melts at high pressures. Nature Communications 5, 5091.

Krasnova, N., Balaganskaya, E. & Garcia, D. (2004). Kovdor-classic phoscorites and carbonatites. In: Wall, F. & Zaitev, A. N. (eds) Phoscorites and Carbonatites from Mantle to Mine: The Key Example of the Kola Alkaline Province. London, GB: Mineralogical Society of Great Britain and Ireland, pp. 99–132.

Kynický, J., Smith, M. P. & Xu, C. (2012). Diversity of rare earth deposits: the key example of China. Elements 8, 361–367.

Leake, B. E., Woolley, A. R., Arps, C. E. S., Birch, W. D., Gilbert, M. C., Grice, J. D., Hawthorne, F. C., Kato, A., Kisch, H. J., Krivovichev, V. G., Linthout, K. L., Laird, J., Mandarino, J., Maresch, W. V., Nichel, E. H., Rock, N. M. S., Schumacher, J. C., Smith, D. C., Stephenson, N. C. N., Ungaretti, L., Whittaker, E. J. W. & Youzhi, G. (1997). Nomenclature of Amphiboles; Report of the Subcommittee on Amphiboles of the International Mineralogical Association Commission on New Minerals and Mineral Names. Mineralogical Magazine 61, 295–321.

Lee, M., Garcia, D., Moutte, J., Williams, C. & Wall, F. (2004). Carbonatites and phoscorites from the Sokli Complex, Finland. In: Wall, F. & Zaitev, A. N. (eds) Phoscorites and Carbonatites from Mantle to Mine: The Key Example of the Kola Alkaline Province. London, UK: Mineralogical Society, pp. 133–162.

Lin, J., Liu, Y. S., Yang, Y. H. & Hu, Z. C. (2016). Calibration and correction of LA-ICP-MS and LA-MC-ICP-MS analyses for element contents and isotopic ratios. Solid Earth Sciences 1, 5–27.

Ling, X. X., Li, Q. L., Liu, Y., Yang, Y. H., Liu, Y., Tang, G. Q. & Li, X. H. (2016). In situ SIMS Th–Pb dating of bastnaesite: constraint on the mineralization time of the Himalayan Mianning–Dechang rare earth element deposits. Journal of Analytical Atomic Spectrometry 31, 1680–1687.

Linnen, R. L., Samson, I. M., Williams-Jones, A. E. & Chakhmouradian, A.R. (2014). Geochemistry of the rare-earth element, Nb, Ta, Hf, and Zr deposits. In: Holland, H. D. & Turekian, K. K. (Eds.), Treatise on Geochemistry, 2nd edition: Oxford, Elsevier, 13, 543–564.

Liu, Y. & Hou, Z. Q. (2017). A synthesis of mineralization styles with an integrated genetic model of carbonatite-syenite-hosted REE deposits in the Cenozoic Mianning–Dechang REE metallogenic belt, the eastern Tibetan Plateau, southwestern China. Journal of Asian Earth Sciences 137, 35–79.

Liu, Y., Chakhmouradian, A. R., Hou, Z. Q., Song, W. L. & Kynický, J. (2019a). Development of REE mineralization in the giant Maoniuping deposit (Sichuan, China): insights from mineralogy, fluid inclusions, and trace-element geochemistry. Mineralium Deposita 54, 701–718.

Liu, Y., Hou, Z. Q., Tian, S. H., Zhang, Q. C., Zhu, Z. M. & Liu, J. H. (2015). Zircon U–Pb ages of the Mianning–Dechang syenites, Sichuan Province, southwestern China: constraints on the giant REE mineralization belt and its regional geological setting. Ore Geology Reviews 64, 554–568.

Liu, Y., Hou, Z. Q., Zhang, R. Q., Wang, P., Gao, J. F. & Raschke, M. B. (2019b). Zircon Alteration as a Proxy for Rare Earth Element Mineralization Processes in Carbonatite-Nordmarkite Complexes of the Mianning-Dechang Rare Earth Element Belt, China. Economic Geology 114, 719–744.

Liu, Y. S., Hu, Z. C., Gao, S., Günther, D., Xu, J., Gao, C. G. & Chen, H. H. (2008). In situ analysis of major and trace elements of anhydrous minerals by LA-ICP-MS without applying an internal standard. Chemical Geology 257, 0–43.

Lu, J., Chen, W., Zhang, W., Liu, H., Simonetti, A., Hu, Z. C., Liu, Y. S., Zhao, K. D. & Jiang, S. Y. (2022). Determination of carbon isotopes in carbonates (calcite, dolomite, magnesite, and siderite) by femtosecond laser ablation multi-collector ICP-MS. J. Journal of Analytical Atomic Spectrometry 37, 278.

Massuyeau, M., Gardès, E., Morizet, Y. & Gaillard, F. (2015). A model for the activity of silica along the carbonatite–kimberlite–mellilitite–basanite melt compositional joint. Chemical Geology 418, 206–216.

Massuyeau, M., Ritter, X. & Sanchez-Valle, Carmen. (2023). A density model for high-pressure carbonate-rich melts applied to carbonatitic magmatism in the upper mantle. Chemical Geology 622, 121275.

McDonough, W. F. & Sun, S. S. (1995). The composition of the Earth. Chemical Geology 120, 223–253.

Middlemost, E. A. K. (1994). Naming materials in the magma/igneous rock system: Earth-Science Reviews 37, 215–224.

Migdisov, A., Williams-Jones, A. E., Brugger, J. & Caporuscio, F. A. (2016). Hydrothermal transport, deposition, and fractionation of the REE: Experimental data and thermodynamic calculations. Chemical Geology 439, 13–42.

Milani, L., Bolhar, R., Frei, D., Harlov, D. E. & Samuel, V. O. (2017). Light rare earth element systematics as a tool for investigating the petrogenesis of phoscorite-carbonatite associations, as exemplified by the Phalaborwa Complex, South Africa. Mineralium Deposita 52, 1105–1125.

Mitchell, R. H. (2005). Carbonatites and carbonatites and carbonatites. The Canadian Mineralogist 43, 2049–2068.

Mitchell, R., Chudy, T., McFarlane, C. R. M. & Wu, F.-Y. (2017). Trace element and isotopic composition of apatite in carbonatites from the Blue River area (British Columbia, Canada) and mineralogy of associated silicate rocks. Lithos 286-287, 75–91.

Moore, M., Chakhmouradian, A. R., Mariano, A. N. & Sidhu, R. (2015). Evolution of rare-earth mineralization in the Bear Lodge carbonatite, Wyoming: Mineralogical and isotopic evidence. Ore Geology Reviews 64, 499–521.

Munoz, J. L., (1984). F–OH and Cl–OH exchange in micas with applications to hydrothermal ore deposits. Reviews in Mineralogy and Geochemistry 13, 469–493.

Nabyl, Z., Massuyeau, M., Gaillard, F., Tuduri, J., Iacono-Marziano, G., Rogerie, G., Le Trong, E., Di Carlo, I., Melleton, J. & Bailly, L. (2020). A window in the course of alkaline magma differentiation conducive to immiscible REE-rich carbonatites. Geochimica et Cosmochimica Acta, 282, 297–323.

Niu, H.-C., Shan, Q., Chen, X.-M. & Zhang, H.-X. (2002). Relationship between light rare earth deposits and mantle processes in the Panxi rift, China. Science in China Series D: Earth Sciences 46, 41–49.

Panina, L. I. (2005). Multiphase carbonate-salt immiscibility in carbonatite melts: data on melt inclusions from the Krestovskiy massif minerals (Polar Siberia). Contributions to Mineralogy and Petrology 150, 19–36.

Poletti, J. E., Cottle, J. M., Hagen-Peter, G. A. & Lackey, J. S. (2016). Petrochronological Constraints on the Origin of the Mountain Pass Ultrapotassic and Carbonatite Intrusive Suite, California. Journal of Petrology 57, 1555–1598.

Prokopyev, I. R., Borisenko, A. S., Borovikov, A. A., & Pavlova, G. G. (2016). Origin of REE-rich ferrocarbonatites in southern Siberia (Russia): implications based on melt and fluid inclusions. Mineralogy and Petrology 110, 845–859.

Ramos, F. C., Wolff, J. A. & Tollstrup, D. L. (2004). Measuring $^{87}Sr/^{86}Sr$ variation in minerals and groundmass from basalts using LA-MC-ICPMS. Chemical Geology 211, 135–158.

Ray, J. S. & Ramesh, R. (2000). Rayleigh fractionation of stable isotopes from a multicomponent source. Geochimica et Cosmochimica Acta 64, 299–306.

Reguir, E. P., Chakhmouradian, A. R., Pisiak, L., Halden, N. M., Yang, P., Xu, C., Kynický, J. & Couëslan, C. G. (2012). Trace-element composition and zoning in clinopyroxene- and amphibole-group minerals: implications for element partitioning and evolution of carbonatites. Lithos 128, 27–45.

Reguir, E. P., Chakhmouradian, A. R., Halden, N. M., Malkovets, V. G. & Yang, P. (2009). Major- and trace-element compositional variation of phlogopite from kimberlites and carbonatites as a petrogenetic indicator. Lithos 112, 372–384.

Russell, J. K., Porritt, L. A., Lavallée, Y. & Dingwell, D.B. (2012). Kimberlite ascent by assimilation-fuelled buoyancy. Nature 481, 352.

Santos, R. V. & Clayton, R. N. (1995). Variations of oxygen and carbon isotopes in carbonatites: a study of Brazilian alkaline complexes. Geochimica et Cosmochimica Acta 59, 1339–1352.

Scheele, N. & Hoefs J. (1992). Carbon isotope fractionation between calcite, graphite and CO_2: an experimental study. Contributions to Mineralogy and Petrology 112, 35–45.

Schultz, L. N., Dideriksen, K., Müter, D., Hakim, S. S. & Stipp, S. L. S. (2013). Early stage Ostwald ripening of submicrometer calcite. Mineralogical Magazine 77, 2168.

Shu, X. C. & Liu, Y. (2019). Fluid inclusion constrains on the Hydrothermal evolution of the Dalucao Carbonatite-related REE deposit, Sichuan Province, China. Ore Geology Reviews 107, 41–57.

Shu, X., Liu, Y. & Li, D. (2020). Contrasting composition of two biotite generations in the Lizhuang rare-earth element deposit, Sichuan Province, Southwestern China. Geological Journal 2020, 1–21.

Smith, M. P. (2007). Metasomatic silicate chemistry at the Bayan Obo Fe–REE–Nb deposit, Inner Mongolia, China: Contrasting chemistry and evolution of fenitising and mineralising fluids, Lithos, 93, 126–148.

Smith, M. P. & Henderson, P. (2000). Preliminary fluid inclusion constraints on fluid evolution in the Bayan Obo Fe–REE–Nb deposit, Inner Mongolia, China. Economic Geology 95, 1371–1388.

Smith, M. P. Campbell, L.S. & Kynicky, J. (2015). A review of the genesis of the world class Bayan Obo Fe–REE–Nb deposits, Inner Mongolia, China: Multistage processes and outstanding questions, Ore Geol. Rev. 64, 459–476.

Smith, M. P., Moore, K., Kavecsanszki, D., Finch, A. A., Kynický, J. & Wall, F. (2016). From mantle to critical zone: A review of large and giant sized deposits of the rare earth elements. Geoscience Frontiers 7, 315–334.

Song, W.L., Xu, C., Veksler, I.V. & Kynicky, J. (2016). Experimental study of REE, Ba, Sr, Mo and W partitioning between carbonatitic melt and aqueous fluid with implications for rare metal mineralization. Contributions to Mineralogy and Petrology 171, 1–12.

Su, J.-H., Zhao, X.-F., Li, X.-C., Hu, W., Chen, M., & Xiong, Y.-L. (2019). Geological and Geochemical Characteristics of the Miaoya Syenite-Carbonatite Complex, Central China:Implications for the Origin of REE-Nb-enriched Carbonatite. Ore Geology Reviews 113, 103101.

Taylor, H. P., Frechen, J. & Degens, E. T. (1967). Oxygen and carbon isotope studies of carbonatites from the Laacher See district, West Germany and the Alnö district, Sweden. Geochimica et Cosmochimica Acta 31, 407–430.

Valley, J. W. (1986). Stable isotope geochemistry of metamorphic rocks: Reviews in Mineralogy and Geochemistry 16, 445–489.

Veksler, I. V., Petibon, C., Jenner, G. A., Dorfman, A. M. & Dingwell, D. B. (1998). Trace Element Partitioning in Immiscible Silicate-Carbonate Liquid Systems: an Initial Experimental Study Using a Centrifuge Autoclave. Journal of Petrology 39, 2095–2104.

Venter, M., Hall, M., & Siegfried, P. (2010). Amended Report NI 43-101 Resource Estimate and Technical Report on the Zandkopsdrift Rare Earth Element (REE) Project, Located in the Republic of South Africa, Independent Resource Estimate Report Prepared for Frontier Rare Earths, Ltd., The MSA Group, pp 185.

Wall, F. & Pell, R. (2020). Responsible sourcing of rare earths: Exploration-stage intervention including life cycle assessment. Handbook on the Physics and Chemistry of Rare Earths, chaper 317, pp. 155–194.

Walter, B. F., Giebel, J., Marlow, A. G., Siegfried, P. R., Marks, M., Markl, G., Palmer, M. & Kolb, J. (2022). The Kieshöhe carbonatites of southwestern Namibia–the post-magmatic role of silicate xenoliths on REE mobilisation. Communications of the Geological Survey of Namibia 25, 1–31.

Walter, B. F., Giebel, R. J., Siegfried, P. R., Gudelius, D., & Kolb, J. (2023). The eruption interface between carbonatitic dykes and diatremes–The Gross Brukkaros volcanic field Namibia. Chemical Geology 621, 121344.

Walter, B. F., Giebel, R. J., Steele-MacInnis, M., Michael, A. M., Kolb, J. & Markl, G. (2021). Fluids associated with carbonatitic magmatism: A critical review and implications for carbonatite magma ascent. Earth-Science Reviews 215, 103509.

Walter, B. F., Parsapoor, A., Braunger, S., Marks, M. A. W., Wenzel, T., Martin, M., & Markl, G. (2018). Pyrochlore as a monitor for magmatic and hydrothermal processes in carbonatites from the Kaiserstuhl volcanic complex (SW Germany). Chemical Geology 498, 1–16.

Walter, B. F., Steele-MacInnis, M., Giebel, R. J., Marks, M. A. W., & Markl, G. (2020). Complex carbonate-sulfate brines in fluid inclusions from carbonatites: Estimating compositions in the system H_2O-Na-K-CO_3-SO_4-Cl. Geochimica et Cosmochimica Acta 277, 224–242.

Wang, D., Yang, J., Yan, S., Xu, J., Chen, Y., Pu, G. & Luo, Y. (2001). A Special Orogenic-type Rare Earth Element Deposit in Maoniuping, Sichuan, China: Geology and Geochemistry. Resource Geology 51, 177–188.

Wei, C. W., Xu, C., Chakhmouradian, A., Brenna, M., Kynický, J. & Song, W. (2020). Carbon-strontium isotope decoupling in carbonatites from Caotan (Qinling, China): Implications for the origin of calcite carbonatite in orogenic settings: Journal of Petrology 61, egaa024.

Wei, C.-W., Deng, M., Xu, C., Chakhmouradian, A. R., Smith, M. P., Kynický, J., Song, W. L., Chen, W. & Fu, B. (2022). Mineralization of the Bayan Obo Rare Earth Element Deposit by Recrystallization and Decarbonation. Economic Geology 117, 1327–1338.

Weng, Q., Niu, H.-C., Qu, P., Li, N.-B., Shan, Q. & Yang, W.-B. (2022b). Controlling factors of prolonged REE mineralization in the Maoniuping REE deposit: Constraints from alkaline granite in the syenite–carbonatite complex. Ore Geology Reviews 142, 104705.

Weng, Q., Yang, W.-B., Niu, H.-C., Li, N.-B. Qu, P., Shan, Q., Fan, G.-Q., Jiang, Z.-Y., Zhang, Z.-Y., Li, A. & Zhao, X.-C. (2021). B–Sr–Nd–Pb isotopic constraints on the origin of the Maoniuping alkaline syenite–carbonatite complex, SW China. Ore Geology Reviews 135, 104193.

Weidendorfer, D., Schmidt, M. W. & Mattsson, H. B. (2017). A common origin of carbonatite magmas. Geology 45, 507–510.

Weidendorfer, D., Schmidt, M. W., & Mattsson, H. B. (2019). Mineral resorption triggers explosive mixed silicate–carbonatite eruptions. Earth and Planetary Science Letters 510, 219–230.

Weng, Q., Niu, H.-C., Qu, P., Li, N.-B., Shan, Q. & Yang, W.-B. (2022b). Controlling factors of prolonged REE mineralization in the Maoniuping REE deposit: Constraints from alkaline granite in the syenite–carbonatite complex. Ore Geology Reviews 142, 104705.

Weng, Q., Yang, W.-B., Niu, H.-C., Li, N.-B. Qu, P., Shan, Q., Fan, G.-Q., Jiang, Z.-Y., Zhang, Z.-Y., Li, A. & Zhao, X.-C. (2021). B–Sr–Nd–Pb isotopic constraints on the origin of the Maoniuping alkaline syenite–carbonatite complex, SW China. Ore Geology Reviews 135, 104193.

Weng, Q., Yang, W.-B., Niu, H.-C., Li, N.-B., Mitchell, B. H., Zhurevinski, S. & Wu, D. (2022a). Formation of the Maoniuping giant REE deposit: Constraints from mineralogy and in situ bastnäsite U-Pb geochronology. American Mineralogist 107, 282–293.

Weng, Z.H., Jowitt, S.M., Mudd, G.M. & Haque, N. (2015). A detailed assessment of global rare earth element resources: opportunities and challenges. Economic Geology 11, 1925–1952.

Whitley, S., Gertisser, R., Halama, R., Preece, K., Troll, V. R. & Deegan, F. M. (2019). Crustal CO_2 contribution to subduction zone degassing recorded through calc-silicate xenoliths in arc lavas. Scientific Reports 9, 8803.

Williams-Jones, A. E., Migdisov, A. A. & Samson, I.M. (2012). Hydrothermal Mobilisation of the Rare Earth Elements – a Tale of "Ceria" and "Yttria". Elements 8, 355–360.

Woolley, A.R. & Kjarsgaard, B.A. (2008). Carbonatite occurrences of the world: Map and database. Geological Survey of Canada, Open File 5796, pp. 28.

Wyllie, P. J. & Lee, W.-J. (1998). Model system controls on conditions for formation of magnesiocarbonatite and calciocarbonatite magmas from the mantle. Journal of Petrology 39, 1885–1893.

Xie, Y. L., Hou, Z. Q., Yin, S. P., Dominy, S. C., Xu, J. H., Tian, S. H. & Xu, W. Y. (2009). Continuous carbonatitic melt–fluid evolution of a REE mineralization system: evidence from inclusions in the Maoniuping REE Deposit, Western Sichuan, China. Ore Geology Reviews 36, 90–105.

Xie, Y. L., Li, Y. X., Hou, Z. Q., Cooke, D. R., Danyushevsky, L., Dominy, S. C. & Yin, S. P. (2015). A model for carbonatite hosted REE mineralisation — the Mianning-Dechang REE belt, Western Sichuan Province, China. Ore Geology Reviews 70, 595–612.

Xu, C., Huang, Z. L., Liu, C. Q., Qi, L., Li, W. B. & Guan, T. (2003). Carbonatite chemistry of Maoniuping REE deposit in Sichuan province. Science in China Series D: Earth Sciences 46, 246–256.

Xu, C., Wang, L., Song, W. & Wu, M. (2010). Carbonatites in China: A review for genesis and mineralization. Geoscience Frontiers 1105–114.

Yang, K. F., Fan, H. R., Pirajno, F. & Li, X. C. (2019). The Bayan Obo (China) giant REE accumulation conundrum elucidated by intense magmatic differentiation of carbonatite. Geology 47, 1198–1022.

Yang, K.-F., Fan, H.-R., Santosh, M., Hu, F.-F. & Wang, K.-Y. (2011). Mesoproterozoic carbonatitic magmatism in the Bayan Obo deposit, Inner Mongolia, North China: Constraints for the mechanism of super accumulation of rare earth elements. Ore Geology Reviews 40, 122–131.

Yang, X. Y., Sun, W. D., Zhang, Y. X. & Zheng, Y. F. (2009). Geochemical constraints on the genesis of the Bayan Obo Fe–Nb–REE deposit in inner Mongolia, China. Geochimica et Cosmochimica Acta 73, 1417–1435.

Yang, Y.-H., Wu, F.-Y., Yang, J.-H., Chew, D. M., Xie, L.-W., Chu, Z.-Y., Zhang, Y.-B. & Huang, C. (2014). Sr and Nd isotopic compositions of apatite reference materials used in U–Th–Pb geochronology. Chemical Geology 385, 35–55.

Yaxley, G.M., Anenburg, M., Tappe, S., Decree, S. & Guzmics, T. (2022). Carbonatites: Classification, Sources, Evolution, and Emplacement. Annual Review of Earth and Planetary Sciences 28, 211–280.

Ye, H.-M., Li, X.-H. & Lan, Z.-W. (2013). Geochemical and Sr–Nd–Hf–O–C isotopic constraints on the origin of the Neoproterozoic Qieganbulake ultramafic–carbonatite complex from the Tarim Block, Northwest China. Lithos 182-183, 150–164.

Yin, A. & Harrison, T.M. (2000). Geologic evolution of the Himalayan–Tibetan orogen. Annual Review of Earth and Planetary Sciences 28, 211–280.

Ying, Y.-C., Chen, W., Simonetti, A., Jiang, S.-Y. & Zhao, K.-D. (2020). Significance of hydrothermal reworking for REE mineralization associated with carbonatite: Constraints from in situ trace element and C-Sr isotope study of calcite and apatite from the Miaoya carbonatite complex (China). Geochimica et Cosmochimica Acta 280, 340–359.

Yuan, Z. X., Shi, Z. M., Bai, G., Wu, C. Y., Chi, R. A. & Li, X. Y. (1995). The Maoniuping Rare Earth Ore Deposit, Mianning County, Sichuan Province. Seismological Publishing House, Beijing, 150 (in Chinese).

Zeng, X., Li, X. C., Fan, H. R., Lan, T. G., Lan, J., Su, J. H., Zhang, P., Yang, K. F. & Zhao, X. F. (2022). Generation of REE-rich syenite-(carbonatite) complex through lithosphere-asthenosphere interaction: An in-situ Sr–Nd–O isotopic study of the Mesozoic Weishan pluton, Northern China. Journal of Asian Earth Sciences 230, 105191.

Zeng, Z. Y & Liu, Y. (2022). Magmatic–hydrothermal zircons in syenite: A record of Nb–Ta mineralization processes in the Emeishan large igneous province, SW China. Chemical Geology 589, 120675.

Zhang, W., Chen, W. T., Mernaph, T. P. & Zhou, L. (2022). Quantifying the nature of ore-forming fluids in the Dalucao carbonatite-related REE deposit, Southwest China: implication for the transport and deposition of REEs. Mineralium Deposita 57, 935–953

Zhang, W., Hu, Z., & Liu, Y. (2020). Iso-Compass: new freeware software for isotopic data reduction of LA-MC-ICP-MS. Journal of Analytical Atomic Spectrometry, 35, 1087–1096.

Zheng, X. & Liu, Y. (2019). Mechanisms of element precipitation in carbonatite-related rare-earth element deposits: evidence from fluid inclusions in the Maoniuping deposit, Sichuan Province, southwestern China. Ore Geology Reviews 107, 218–238.

Zheng, X., Liu, Y. & Zhang, L. S. (2021). The role of sulfate-, alkali-, and halogen-rich fluids in mobilization and mineralization of rare earth elements: Insights from bulk fluid compositions in the Mianning–Dechang carbonatite-related REE belt, southwestern China. Lithos 386–387, 106008.

1594 **TABLE CAPTIONS**

1595 **Table 1.** Whole-rock chemistry of carbonatite I, II, nordmarkite, and alkali granite

1596 from the HZKS-1 drill core at Maoniuping.

Rock		**Carboantite I**												**Carbonatite II**		
Sample No.		**HZKS-1-3**	**HZKS-1-6**	**HZKS-1-7**	**HZKS-1-17**	**HZKS-1-22**	**HZKS-1-2B**	**HZKS-1-5A**	**HZKS-1-5B**	**HZKS-1-10A**	**HZKS-1-2A**	**HZKS-1-10B**	**HZKS-1-31**	**HZKS-1-4**	**HZKS-1-13**	**HZKS-1-18A**
wt.%																
SiO_2		0.83	0.40	0.82	0.29	0.35	3.09	0.45	0.44	0.78	5.00	####	###	2.32	5.45	9.32
TiO_2		0.00	0.01	0.00	0.00	0.02	0.00	0.01	0.01	0.04	0.10	0.08	0.08	0.09	0.02	0.08
Al_2O_3		0.01	0.22	0.00	0.01	0.04	0.19	0.06	0.06	0.49	1.98	3.38	3.38	0.37	0.07	0.37
TFe_2O_3		0.64	0.77	0.65	0.64	0.87	0.50	0.92	0.92	0.61	0.95	0.61	0.79	1.53	0.56	1.52
FeO		0.43	0.49	0.44	0.43	0.58	0.39	0.69	0.66	0.31	0.50	0.44	0.38	0.32	0.22	0.42
MnO		0.98	0.94	0.98	0.97	0.93	0.55	0.83	0.82	0.44	0.60	0.67	0.81	0.42	0.41	0.42
MgO		0.25	0.69	0.24	0.26	0.65	0.14	0.20	0.20	0.13	0.17	0.18	0.29	0.13	0.21	0.14
CaO		### ##	### ##	### ##	### ##	### ##	### ##	### #	### ##	##### #	### ##	##### #	### #	### ##	### ##	##### #
SrO		1.32	1.50	1.32	1.27	1.78	2.10	1.19	1.16	0.88	1.16	0.96	1.38	1.50	1.02	1.50
BaO		0.83	0.71	0.84	0.13	0.25	1.47	0.22	0.22	3.75	1.38	1.16	0.39	4.50	8.50	4.50
Na_2O		0.02	0.78	0.03	0.10	0.18	0.04	0.05	0.05	0.11	1.39	0.49	0.12	0.17	0.13	0.02
K_2O		0.02	0.23	0.02	0.02	0.20	0.15	0.03	0.03	0.34	0.15	2.45	0.03	0.22	0.05	0.22
P_2		0.0	0.0	0.0	0.01	0.01	0.02	0.02	0.01	0.06	0.11	0.01	0.25	0.1	0.07	0.11

O_5		2	2	2									0		
SO_3		0.68	0.55	0.67	0.15	0.73	0.64	0.73	0.73	3.91	1.50	0.90	0.47	2.58	5.03	2.58
F		0.12	0.80	0.00	0.11	0.30	1.30	0.10	0.10	7.10	0.10	0.10	0.20	#####	9.40	#####
Cl		0.00	0.01	0.00	0.00	0.00	0.00	0.01	0.01	0.01	0.00	0.00	0.01	0.01	0.00	0.01
LOI		#####	#####	#####	#####	#####	#####	####	#####	#####	#####	#####	####	#####	#####	#####
Total		#####	#####	#####	#####	#####	#####	####	#####	#####	#####	#####	####	#####	#####	#####
ppm																
Li		2.40	31.9	2.40	1.10	59.7	0.40	2.10	1.60	1.20	2.9	4.20	4.10	1.70	17.0	19.2
Be		b.d.	b.d.	b.d.	b.d.	b.d.	b.d.	0.42	0.05	0.37	b.d.	b.d.	b.d.	5.21	1.41	3.98
Rb		1.60	75.4	1.70	1.50	19.3	5.50	1.60	1.30	10.0	104	92.6	1.60	8.80	3.40	202
Sr		#####	8750	#####	#####	#####	#####	####	9809	7870	9809	8450	####	#####	8625	#####
Ba		7420	6730	7570	1175	2239	#####	#####	2080	8957	#####	#####	3493	#####	#####	#####
Zn		51.7	123	51.7	52.7	137	32.0	13.0	13.0	409	31.0	33.0	24.0	2010	92.0	225
Sc		0.50	0.70	0.50	0.40	1.20	0.20	0.40	0.40	0.40	0.90	0.50	0.70	0.60	0.50	1.60
Y		207	124	211	239	201	104	124	129	74.0	152	87.0	203	147	356	145
Zr		2.00	97.0	4.00	2.00	4.00	3.00	3.00	3.00	15.0	126	32.0	6.00	23.0	8.00	277
Nb		32.2	197	33.1	3.70	30.2	2.10	6.70	6.70	52.5	36.5	46.3	4.10	272	73.5	283
Sn		0.20	2.00	0.20	0.20	1.00	1.00	1.00	1.00	1.00	5.00	2.00	2.00	1.80	0.00	5.30
La		644	980	655	548	832	980	541	756	1070	780	825	9080	2940	#####	2840
Ce		1350	1401	1365	1315	1540	1470	933	1470	1680	1365	1455	####	3940	#####	4690
Pr		166	126	165	172	160	111	91.7	156	162	141	143.0	1733	352	4801	463
Nd		622	496	628	680	559	338	302	552	529	480	478	308	102	###	1210

													0	5	##	
Sm		108	72.5	108	125	89.6	41.5	36.4	76.3	57.6	70.3	57.6	209	88.5	828	116
Eu		27.8	16.5	28.5	33.1	22.3	13.5	7.77	17.6	12.4	16.8	13.2	45.5	18.5	133	19.8
Gd		77.7	44.3	79.0	94.4	60.7	26.8	19.6	47.0	28.1	46.8	31.8	106	41.7	269	44.8
Tb		9.53	5.38	9.86	11.6	8.06	3.26	2.21	5.66	2.91	6.03	3.80	11.6	4.58	24.2	4.12
Dy		44.4	25.7	45.5	53.5	40.3	15.0	10.0	27.1	12.4	29.3	17.9	45.7	20.4	76.0	14.2
Ho		8.48	4.80	8.70	10.5	7.54	2.91	1.79	5.06	2.19	5.49	3.29	7.67	3.73	11.6	2.33
Er		21.8	12.7	22.3	26.8	19.8	8.23	4.81	13.2	5.47	15.1	8.98	19.5	9.44	28.4	5.49
Tm		3.04	1.81	3.22	3.72	2.87	1.23	0.68	1.89	0.80	2.14	1.29	2.59	1.35	3.56	0.70
Yb		18.4	10.7	18.5	21.6	16.6	7.81	4.22	11.3	4.82	12.8	7.76	15.3	7.98	20.2	4.54
Lu		2.56	1.64	2.58	3.12	2.53	1.21	0.65	1.76	0.78	1.84	1.20	2.05	1.31	2.71	0.65
Hf		0.10	2.80	0.10	0.10	0.10	0.10	0.10	0.10	0.60	3.90	1.00	0.20	0.90	0.20	8.50
Ta		0.07	1.50	0.07	0.05	0.10	0.10	0.10	0.10	0.40	0.90	0.50	0.10	1.20	0.50	2.97
Pb		127	900	126	142	550	1410	###	5380	1400	515	97.5	117	3120	547	830
Th		3.61	12.7	3.57	1.71	140	4.39	3.99	4.19	28.7	14.2	16.0	106	55.8	674	156
U		23.5	3.80	23.2	2.61	3.70	4.00	5.39	5.11	3.68	4.80	3.60	4.30	303	161	251
LREE		2918	3092	2949	2873	3203	2954	####	3027	3511	2853	2972	####	8364	#####	9339
HREE		186	107	190	225	158	66.5	44.0	113	57.4	119	76.0	210	90.5	436	76.8
ΣREE		3104	3198	3139	3098	3361	3020	####	3140	3568	2973	3048	####	8454	#####	9416
LREE/HREE		15.7	28.9	15.6	12.8	20.2	44.4	43.5	26.8	61.1	23.9	39.1	146	92.4	292	122
$(La/Sm)_N$		10.0	9.28	3.78	2.75	2.75	17.8	6.07	6.19	11.6	6.93	8.94	3.78	20.7	40.5	20.1

$(Sm/Yb)_N$	7.18	9.38	6.37	6.27	6.27	5.78	7.41	7.35	13.0	6.00	8.07	6.37	12.1	54.4	12.3
$(La/Yb)_N$	71.8	87.1	24.1	17.2	17.2	103	45.0	45.4	151	41.6	72.2	24.1	250	2202	247
Y/Ho	24.4	25.8	24.3	22.8	26.7	35.7	69.3	25.5	33.8	27.7	26.4	26.5	39.4	30.8	62.0
δEu	0.92	0.89	0.94	0.93	0.92	1.23	0.89	0.90	0.94	0.89	0.94	0.93	0.93	0.86	0.84
δCe	1.00	1.01	1.01	1.04	1.02	1.01	1.01	1.04	0.98	1.00	1.02	1.01	0.94	1.00	0.99
C/CMF (%)	97.3	96.1	97.3	97.3	96.1	98.1	97.2	97.3	98.4	97.8	97.4	96.9	98.4	97.8	97.9
															(continued)

1597 (continued)

1598 **Table 1 continued**

Rock											**Nordmarkite**				
Sample No.		**HZKS-1-18B**	**HZKS-1-21A**	**HZKS-1-21B**	**HZKS-1-27**	**HZKS-1-28**	**HZKS-1-32**	**HZKS-1-37**	**HZKS-1-38**	**HZKS-1-39**	**HZKS-1-19**	**HZKS-1-20**	**HZKS-1-24A**	**HZKS-1-24B**	**HZKS-1-26**
wt.%															
SiO_2		2.51	#####	#####	2.34	1.29	0.93	2.21	0.15	9.02	#####	#####	#####	#####	#####
TiO_2		0.20	0.21	0.20	0.08	0.21	0.01	b.d.	b.d.	b.d.	0.18	0.18	0.08	0.10	0.16
Al_2		0.76	1.81	1.79	0.36	4.93	0.03	0.06	<0.01	2.32	#####	#####	#####	#####	9.11

O_3															
TFe_2O_3		1.04	0.84	0.85	1.50	0.84	1.77	1.06	0.30	0.63	1.68	1.13	2.78	3.17	1.38
FeO		0.33	0.30	0.22	0.27	0.31	0.42	0.40	0.25	0.27	0.33	0.24	0.31	0.25	0.24
MnO		0.10	0.41	0.42	0.42	0.41	0.46	0.72	0.69	0.60	0.03	0.03	0.02	0.02	0.12
MgO		0.90	0.19	0.19	0.13	0.19	0.12	0.33	0.08	0.15	0.04	0.07	0.14	0.15	0.06
CaO		#####	#####	#####	#####	#####	#####	#####	#####	#####	0.22	0.30	0.48	0.45	#####
SrO		0.15	0.61	0.63	1.50	0.61	8.63	1.15	1.01	1.03	0.31	0.02	0.15	0.17	0.11
BaO		4.36	5.23	5.29	4.48	5.01	#####	0.16	0.15	0.34	0.58	0.09	0.14	0.16	0.46
Na_2O		0.59	0.41	0.37	0.17	0.39	0.04	0.30	0.04	0.54	5.68	5.64	5.49	5.48	1.63
K_2O		0.21	1.79	1.78	0.22	0.83	0.03	0.07	0.01	1.61	5.57	6.16	6.23	4.10	4.87
P_2O_5		0.05	0.09	0.09	0.10	0.09	0.02	0.01	<0.01	0.01	0.07	0.02	0.03	0.02	0.02
SO_3		2.87	3.31	3.35	2.56	3.21	#####	0.33	0.23	0.38	0.31	0.05	0.27	0.61	1.27
F		#####	2.00	2.10	#####	#####	0.10	0.20	0.10	0.20	0.00	0.10	0.00	0.00	2.10

Cl		0.01	0.01	0.01	0.01	0.01	0.01	b.d.	b.d.	b.d.	0.02	0.03	0.00	0.00	0.01
LOI		#####	#####	#####	#####	#####	#####	####	#####	#####	1.83	1.24	0.52	0.94	7.16
Total		#####	#####	#####	#####	#####	#####	####	#####	#####	#####	#####	####	#####	#####
ppm															
Li		19.3	18.4	18.0	1.60	18.2	0.80	14.9	0.60	8.80	10.7	11.6	36.2	35.3	0.90
Be		3.89	0.84	0.84	4.91	0.89	0.34	2.95	0.06	1.81	0.22	3.06	6.81	7.65	0.90
Rb		200	157	148	8.60	152	1.80	2.90	0.40	51.6	189	239	213	210	0.15
Sr		1430	7380	7180	#####	7180	#####	>10000	9500	9780	421	240	1310	1545	5930
Ba		#####	#####	#####	#####	#####	#####	####	1295	3000	5880	970	1395	1590	4120
Zn		232	1080	1040	2020	1070	262	64.0	20.0	48.0	31.0	33.0	53.0	33.0	1080
Sc		1.60	0.50	0.50	0.60	0.50	0.10	0.90	0.20	0.40	0.30	2.20	0.40	0.40	0.40
Y		51.6	113	111	142	113	63.1	125	146	124	20.6	45.4	16.7	19.9	151
Zr		266	226	219	20.0	230	16.0	4.00	<2.00	2.00	265	162	171	166	134
Nb		282	252	252	259	248	5.00	0.70	0.20	12.9	56.6	25.9	14.5	16.5	70.6
Sn		5.30	3.00	3.00	1.70	2.80	1.00	0.70	<0.20	0.50	1.00	7.00	1.70	1.50	1.60
La		2830	#####	#####	2830	#####	726	634	654	583	565	56.0	139	143	777
Ce		4690	#####	#####	3780	#####	910	####	1205	1070	588	98.7	214	221	1190
Pr		459	5554	4529	338	3845	84.1	130	130	114	53.8	10.2	####	20.2	124
Nd		1210	7200	7180	973	7170	278	469	471	405	158	34.7	58.0	60.3	429
S		115	433	428	86.2	430	37.0	65.6	66.5	56.0	15.1	7.29	7.60	8.60	66.5

m															
Eu		19.6	64.5	62.8	18.3	62.1	9.33	15.5	16.2	13.8	3.50	1.21	1.63	1.97	17.1
Gd		43.1	119	114	42.2	113	22.0	39.1	41.3	34.9	7.25	6.12	4.39	5.49	44.5
Tb		3.93	11.7	11.1	4.44	10.9	2.63	4.66	5.07	4.30	0.85	1.10	0.61	0.74	5.80
Dy		13.9	32.5	32.8	20.6	32.3	12.5	22.6	24.8	21.2	3.71	6.87	2.98	3.85	29.2
Ho		2.22	4.84	4.70	3.63	4.81	2.31	4.21	4.58	3.98	0.64	1.51	0.55	0.65	5.31
Er		5.13	11.7	11.4	9.36	11.4	6.09	11.7	13.0	11.5	1.70	4.55	1.32	1.52	13.7
Tm		0.74	1.44	1.47	1.35	1.47	0.90	1.62	1.80	1.60	0.22	0.77	0.16	0.19	1.84
Yb		4.20	8.36	8.75	8.23	8.60	5.31	9.36	10.4	9.35	1.26	4.96	0.92	1.09	10.7
Lu		0.62	1.51	1.47	1.27	1.48	0.83	1.31	1.41	1.33	0.19	0.81	0.13	0.15	1.50
Hf		8.00	6.50	6.40	0.80	6.60	0.50	0.30	<0.10	0.20	6.60	6.30	5.70	5.90	3.70
Ta		2.92	1.09	1.09	1.13	1.09	0.20	b.d.	<0.05	0.05	1.00	2.70	0.59	0.69	0.59
Pb		839	825	799	3130	802	8950	207	91.2	194	329	22.2	99.5	58.0	1710
Th		157	361	357	53.6	355	4.07	1.47	1.37	15.8	32.2	29.8	53.2	50.6	9.10
U		249	120	112	303	115	3.37	0.52	0.12	4.52	16.6	6.83	12.0	12.1	62.8
LREE		9324	#####	#####	8025	#####	2044	#####	2543	2241	1383	208	440	455	2603
HREE		73.8	191	186	91.1	184	52.6	94.5	102	88.1	15.8	26.7	11.1	13.7	113
ΣREE		9398	#####	#####	8117	#####	2097	#####	2645	2329	1399	235	451	468	2716
LREE/HREE		126	518	534	88.1	524	38.9	26.5	24.9	25.4	87.4	7.80	39.8	33.2	23.1
$(La/Sm)_N$		15.3	42.7	41.6	20.5	40.5	12.3	40.5	40.5	40.5	23.4	10.3	11.4	10.3	8.51
$(Sm/Yb)_N$		29.9	56.3	53.2	11.4	54.4	7.58	54.4	54.4	54.4	13.0	8.58	8.99	8.58	5.52

$(La/Yb)_N$		458	2404	2211	234	2202	1.00	####	2202	2202	305	88.8	103	88.8	47.0
Y/Ho		23.2	23.3	23.5	39.0	23.4	27.3	29.6	31.9	31.2	32.2	30.1	30.4	30.6	28.3
δEu		0.85	0.87	0.87	0.92	0.86	1.00	0.93	0.94	0.95	1.02	0.55	0.86	0.87	0.96
δCe		1.00	1.05	1.24	0.94	1.33	0.89	1.01	1.00	1.01	0.82	1.00	0.99	1.00	0.93
C/CMF(%)		96.8	97.9	98.0	98.5	98.1	97.4	97.5	98.5	98.1					

1599 (continued)

1600 **Table 1 continued**

Rock		**Alkali granite**									**Altered alkali granite**			
Sample No.		**HZKS-1-8**	**HZKS-1-9**	**HZKS-1-14**	**HZKS-1-16**	**HZKS-1-23**	**HZKS-1-29**	**HZKS-1-30**	**HZKS-1-34**	**HZKS-1-35**	**HZKS-1-15**	**HZKS-1-23A**	**HZKS-1-33**	**HZKS-1-36**
wt.%														
SiO_2		#####	#####	#####	#####	#####	#####	####	#####	#####	#####	######	####	#####
TiO_2		0.11	0.10	0.11	0.16	0.12	0.17	0.17	0.74	0.16	0.21	0.16	0.71	0.35
Al_2O_3		9.63	#####	9.63	#####	#####	#####	####	7.57	9.19	#####	9.19	9.53	#####
TFe_2O_3		4.18	3.17	4.18	1.76	1.40	2.62	2.62	4.55	1.37	0.94	1.37	3.57	4.39
FeO		0.25	0.41	0.41	0.42	0.33	0.26	0.24	0.32	0.31	0.31	0.22	0.25	0.29
MnO		0.11	0.02	0.11	0.01	0.02	0.05	0.05	0.12	0.11	0.28	0.11	0.11	0.10
MgO		0.16	0.15	0.16	0.15	0.17	0.24	0.24	0.05	0.05	0.09	0.05	0.05	0.05
CaO		3.38	0.45	3.38	0.55	0.61	3.48	3.42	0.43	3.85	#####	######	0.32	0.13
SrO		0.43	0.17	0.43	0.02	0.47	0.06	0.06	0.01	0.11	1.75	0.11	0.01	0.00
BaO		0.55	0.16	0.55	0.08	0.17	0.52	0.52	0.04	0.46	3.94	0.46	0.03	0.01
Na_2O		0.30	2.48	0.30	3.65	5.07	2.97	2.94	2.59	1.63	0.69	1.63	3.44	3.57
K_2O		5.67	4.10	5.67	4.90	4.60	5.06	5.04	2.84	4.85	8.24	5.85	3.34	4.30
P_2O		0.09	0.02	0.09	0.02	0.03	0.02	0.02	0.04	0.02	0.07	0.02	0.02	0.02

5														
SO_3		1.40	0.61	1.40	0.05	0.47	1.60	1.60	0.08	1.26	4.97	1.26	0.03	0.03
F		0.80	0.00	0.80	0.00	0.20	0.80	0.70	0.00	3.10	0.00	3.10	0.00	0.00
Cl		0.01	0.00	0.01	0.01	0.01	0.01	0.01	0.01	0.01	0.01	0.01	0.01	0.01
LOI		1.40	0.94	1.40	0.51	1.24	2.81	3.04	2.24	6.57	#####	6.57	2.12	1.76
Total		#####	#####	#####	#####	#####	#####	#####	#####	#####	#####	######	#####	#####
ppm														
Li		2.10	35.3	2.10	16.8	32.4	13.8	13.9	30.4	4.10	2.70	4.10	22.3	51.6
Be		1.98	7.65	1.98	2.77	0.61	4.03	3.89	307	1.78	1.73	1.78	265	253
Rb		256	210	256	0.00	225	250	257	990	0.03	0.25	0.03	964	1225
Sr		3620	1545	3620	122	1620	459	457	115	1020	#####	1020	109	33.4
Ba		4926	1590	4926	876	1690	4910	#####	410	4380	#####	4380	211	125
Zn		1740	33.0	1740	38	67.0	187	194	2950	57	72	57	1790	2790
Sc		1.20	0.40	1.20	1.60	0.80	1.60	1.50	0.10	0.50	0.20	0.50	0.10	0.20
Y		16.4	19.9	16.4	22.8	18.2	42.7	41.6	1590	47.3	57.0	47.3	1995	1100
Zr		175	166	175	124	154	272	266	#####	380	127	380	#####	3100
Nb		58.1	16.5	58.1	37.6	26.0	58.4	57.3	1495	125	245	125	1925	1615
Sn		3.30	1.50	3.30	2.70	2.00	4.40	4.80	325	3.80	3.60	3.80	299	245
La		757	143	757	185	122	185	170	343	278	561	278	452	367
Ce		1175	221	1175	269	208	271	254	1035	428	822	428	1315	1030
Pr		107	20.2	107	25.4	18.8	26.0	25.0	133	43.5	82.2	43.5	196	125
Nd		287	60.3	287	74.6	58.6	84.8	80.6	496	143	264	143	706	423
Sm		23.0	8.60	23.0	8.73	8.49	12.9	12.9	179	20.4	34.3	20.4	254	137
Eu		5.26	1.97	5.26	1.45	1.91	2.31	2.29	1.63	4.07	9.81	4.07	2.31	1.31
Gd		10.0	5.49	10.0	5.69	5.26	8.16	8.27	211	11.6	21.9	11.6	279	163
Tb		1.02	0.74	1.02	0.80	0.73	1.24	1.24	44.9	1.37	2.54	1.37	59.5	35.3
Dy		3.65	3.85	3.65	4.15	3.48	7.18	7.05	293	7.32	11.9	7.32	390	224
Ho		0.65	0.65	0.65	0.79	0.61	1.53	1.43	63.0	1.37	2.31	1.37	82.5	46.2
Er		1.67	1.52	1.67	2.24	1.41	4.43	4.28	181	3.91	5.98	3.91	232	130
Tm		0.25	0.19	0.25	0.33	0.19	0.67	0.63	28.2	0.60	0.87	0.60	34.9	18.2
Yb		1.68	1.09	1.68	2.52	0.99	4.27	4.28	169	4.02	5.63	4.02	202	102
Lu		0.25	0.15	0.25	0.41	0.15	0.70	0.68	24.9	0.66	0.82	0.66	29.9	13.8
Hf		5.20	5.90	5.20	4.30	4.90	8.70	8.60	704	13.9	3.20	13.9	642	80.6
Ta		0.38	0.69	0.38	2.12	0.90	1.72	1.75	110	2.69	1.26	2.69	122	71.8
Pb		5670	58.0	5670	97.0	159	220	219	994	198	239	198	327	416

Th		35.7	50.6	35.7	22.2	52.9	17.4	16.3	746	26.3	20.3	26.3	506	428
U		9.26	12.1	9.26	5.56	11.5	28.4	27.9	201	102	177	102	207	99.8
LREE		2354	455	2354	564	418	582	545	2187	916	1773	916	2925	2083
HREE		19.2	13.7	19.2	16.9	12.8	28.2	27.9	1015	30.9	51.9	30.9	1310	732
ΣREE		2373	468	2373	581	431	610	573	3202	947	1825	947	4235	2815
LREE/HREE		123	33.2	123	33.3	32.6	20.6	19.6	2.15	29.7	34.2	29.7	2.23	2.85
$(La/Sm)_N$		20.6	10.3	20.6	13.2	8.97	8.93	8.26	1.20	8.51	10.2	8.51	1.11	1.67
$(Sm/Yb)_N$		14.9	8.58	14.9	3.77	9.33	3.29	3.27	1.15	5.52	6.63	5.52	1.37	1.46
$(La/Yb)_N$		306	88.8	306	49.9	83.7	29.4	27.0	1.38	47.0	67.7	47.0	1.52	2.44
Y/Ho		25.2	30.6	25.2	28.9	29.8	27.9	29.1	25.2	34.5	24.7	34.5	24.2	23.8
δEu		1.06	0.87	1.06	0.63	0.87	0.69	0.68	0.03	0.81	1.09	0.81	0.03	0.03
δCe		1.00	1.00	1.00	0.95	1.05	0.95	0.94	1.17	0.94	0.93	0.94	1.07	1.16
C/CMF(%)														

b.d. = below detection limit; C/CMF = CaO/(CaO+MgO+FeO+MnO) (in molar proportions)

1611 **Table 2.** Bulk C–O isotopic compositions of calcite in carbonatite I, II, and the

1612 contact zone from the HZKS-1 drill core at Maoniuping.

Sample No.	Generations	$\delta^{13}C_{V\text{-}PDB}$‰	$\delta^{18}O_{V\text{-}SMOW}$‰
HZKS-1-6	Cal-I	-7.0	7.5
HZKS-1-7	Cal-I	-7.0	7.8
HZKS-1-17	Cal-I	-7.1	6.7
HZKS-1-22	Cal-I	-7.1	5.7
HZKS-1-2B	Cal-I	-6.6	5.4
HZKS-1-5A	Cal-II	-7.3	5.7
HZKS-1-5B	Cal-II	-6.9	7.4
HZKS-1-10A	Cal-II	-7.0	6.6
HZKS-1-2A	Cal-II	-6.8	8.4
HZKS-1-4	Cal-III	-6.7	9.2
HZKS-1-13	Cal-III	-6.9	8.4
HZKS-1-13T	Cal-III	-7.1	8.8
HZKS-1-18	Cal-III	-6.8	8.3
HZKS-1-27	Cal-III	-6.2	11.0
HZKS-1-32	Cal-III	-6.5	8.1
HZKS-1-32T	Cal-III	-6.7	9.4
HZKS-1-38	Cal-III	-6.7	10.0
HZKS-1-39	Cal-III	-6.5	9.6
HZKS-1-10B	Cal-IV	-6.9	8.2
HZKS-1-15	Cal-IV	-7.0	7.7
HZKS-1-15T	Cal-IV	-7.1	8.7
HZKS-1-26	Cal-IV	-6.8	7.9
HZKS-1-26T	Cal-IV	-6.6	7.4
HZKS-1-31	Cal-IV	-6.6	8.7

1613

1614

1615

1616

1617

1618 **Table 3.** In-situ Sr isotopic compositions of calcite in carbonatite I, II, and the contact

1619 zone from the HZKS-1 drill core at Maoniuping.

Sample/spot	Mineral	REE (ppm)	Rb (ppm)	Sr(ppm)	Rb/Sr	$^{84}Sr/^{86}Sr$	2σ	$^{87}Sr/^{86}Sr$	2σ	^{88}Sr (V)
HZKS-1-6-1	Cal-I	1051	0.03	7246	######	#####	#####	0.70605	#####	6.0
HZKS-1-6-2	Cal-I	1013	0.02	7171	######	#####	#####	0.70615	#####	6.0
HZKS-1-6-3	Cal-I	840	0.01	7757	######	#####	#####	0.70611	#####	5.9
HZKS-1-6-4	Cal-I	808	0.02	6422	######	#####	#####	0.70611	#####	7.9
HZKS-1-6-5	Cal-I	948	0.06	7991	######	#####	#####	0.70611	#####	6.6
HZKS-1-6-6	Cal-I	949	0.02	9325	######	#####	#####	0.70611	#####	6.2
HZKS-1-7-1	Cal-I	1135	0.06	10617	######	#####	#####	0.70610	#####	6.8
HZKS-1-7-2	Cal-I	881	0.03	9320	######	#####	#####	0.70602	#####	7.2
HZKS-1-7-3	Cal-I	460	0.06	6356	######	#####	#####	0.70615	#####	6.7
HZKS-1-7-5	Cal-I	448	0.13	6031	######	#####	#####	0.70611	#####	5.9
HZKS-1-17-1	Cal-I	994	0.13	6368	######	#####	#####	0.70616	#####	6.5
HZKS-1-17-2	Cal-I	828	0.01	5654	######	#####	#####	0.70614	#####	5.1
HZKS-1-17-3	Cal-I	994	0.13	6368	######	#####	#####	0.70603	#####	7.8
HZKS-1-17-4	Cal-I	612	0.10	7432	######	#####	#####	0.70601	#####	3.7
HZKS-1-17-5	Cal-I	751	0.10	8155	######	#####	#####	0.70619	#####	5.8
HZKS-1-17-6	Cal-I	800	0.05	6105	######	#####	#####	0.70613	#####	5.0
HZKS-1-17-7	Cal-I	1082	0.10	9126	######	#####	#####	0.70623	#####	8.1

HZKS-1-17-8	Cal-I	989	0.03	6909	######	#####	#####	0.7061 0	#####	5.4
HZKS-1-17-9	Cal-I	858	0.02	6295	######	#####	#####	0.7061 9	#####	8.8
HZKS-1-22-1	Cal-I	1052	0.06	7039	######	#####	#####	0.7061 7	#####	6.4
HZKS-1-22-3	Cal-I	850	0.02	6462	######	#####	#####	0.7060 6	#####	5.9
HZKS-1-22-4	Cal-I	791	0.02	6319	######	#####	#####	0.7061 0	#####	6.7
HZKS-1-22-7	Cal-I	904	0.00	6167	######	#####	#####	0.7061 9	#####	9.4
HZKS-1-22-8	Cal-I	1135	0.02	7864	######	#####	#####	0.7061 5	#####	6.4
HZKS-1-22-9	Cal-I	1136	0.02	7486	######	#####	#####	0.7060 7	#####	9.5
HZKS-1-22-11	Cal-I	694	0.05	6168	######	#####	#####	0.7061 1	#####	8.1
HZKS-1-2B-1	Cal-II	1441	b.d.	8659	b.d.	#####	#####	0.7061 5	#####	7.0
HZKS-1-2B-2	Cal-II	1517	0.12	10935	######	#####	#####	0.7060 7	#####	5.9
HZKS-1-2B-3	Cal-II	1566	0.01	11150	######	#####	#####	0.7063 0	#####	4.7
HZKS-1-2B-4	Cal-II	884	b.d.	8530	b.d.	#####	#####	0.7062 3	#####	5.6
HZKS-1-2B-7	Cal-II	1725	0.08	8519	######	#####	#####	0.7063 1	#####	5.2
HZKS-1-2B-8	Cal-II	1271	0.02	7500	######	#####	#####	0.7061 5	#####	6.5
HZKS-1-2B-9	Cal-II	1391	b.d.	7932	b.d.	#####	#####	0.7061 7	#####	7.6
HZKS-1-2B-10	Cal-II	1361	0.02	7897	######	#####	#####	0.7061 7	#####	6.0
HZKS-1-5A-1	Cal-II	1804	0.11	11041	######	#####	#####	0.7061 5	#####	5.4
HZKS-1-5A-2	Cal-II	2145	0.02	12124	######	#####	#####	0.7061 8	#####	6.0
HZKS-1-5A-3	Cal-II	1765	0.03	9869	######	#####	#####	0.7061 4	#####	6.0
HZKS-1-5A-	Cal-II	1363	0.10	8553	######	#####	#####	0.7061	#####	5.8

4					#	#	#	6	#	
HZKS-1-5A-5	Cal-II	1276	0.01	10337	######	#####	#####	0.70613	#####	6.0
HZKS-1-5A-7	Cal-II	1375	0.27	9576	######	#####	#####	0.70616	#####	5.1
HZKS-1-5A-8	Cal-II	943	0.10	7016	######	#####	#####	0.70612	#####	7.2
HZKS-1-5A-9	Cal-II	985	0.24	7359	######	#####	#####	0.70614	#####	7.9
HZKS-1-5A-10	Cal-II	1528	0.05	8885	######	#####	#####	0.70608	#####	8.6
HZKS-1-5B-1	Cal-II	1503	0.18	10003	######	#####	#####	0.70613	#####	6.7
HZKS-1-5B-2	Cal-II	998	0.01	7085	######	#####	#####	0.70637	#####	8.2
HZKS-1-5B-3	Cal-II	969	0.27	8062	######	#####	#####	0.70620	#####	7.9
HZKS-1-5B-4	Cal-II	747	0.05	8075	######	#####	#####	0.70618	#####	7.8
HZKS-1-5B-6	Cal-II	1956	0.13	17728	######	#####	#####	0.70610	#####	8.1
HZKS-1-10A-1	Cal-II	1439	b.d.	8228	b.d.	#####	#####	0.70636	#####	6.3
HZKS-1-10A-2	Cal-II	1001	0.07	7191	######	#####	#####	0.70617	#####	5.2
HZKS-1-10A-3	Cal-II	1288	0.04	8817	######	#####	#####	0.70617	#####	6.5
HZKS-1-10A-4	Cal-II	1183	0.02	8407	######	#####	#####	0.70605	#####	5.4
HZKS-1-10A-5	Cal-II	1414	0.11	8088	######	#####	#####	0.70615	#####	4.8
HZKS-1-10A-6	Cal-II	1589	b.d.	8147	b.d.	#####	#####	0.70612	#####	5.6
HZKS-1-10A-7	Cal-II	865	0.07	6777	######	#####	#####	0.70618	#####	4.9

1620 (continued)

1621 Table 3 continued

Sample/spot	Mineral	REE (ppm)	Rb (ppm)	Sr(ppm)	Rb/Sr	$^{84}Sr/^{86}Sr$	2σ	$^{87}Sr/^{86}Sr$	2σ	^{88}Sr (V)

			m)							
HZKS-1-4-1	Cal-III	2090	0.11	14195	######	#####	#####	0.7064	#####	6.4
HZKS-1-4-2	Cal-III	1768	0.10	13802	######	#####	#####	0.7061	#####	6.0
HZKS-1-4-3	Cal-III	2105	0.48	13391	######	#####	#####	0.7064	#####	5.0
HZKS-1-4-4	Cal-III	1810	0.43	13958	######	#####	#####	0.7066	#####	6.2
HZKS-1-4-5	Cal-III	1563	0.08	8899	######	#####	#####	0.7064	#####	5.9
HZKS-1-13-1	Cal-III	1405	0.06	9823	######	#####	#####	0.7060	#####	6.1
HZKS-1-13-2	Cal-III	1600	0.01	10376	######	#####	#####	0.7062	#####	5.2
HZKS-1-13-4	Cal-III	1485	0.02	9012	######	#####	#####	0.7059	#####	9.8
HZKS-1-13-5	Cal-III	1589	0.07	10188	######	#####	#####	0.7064	#####	9.5
HZKS-18-3	Cal-III	1379	0.01	7158	######	#####	#####	0.7063	#####	6.0
HZKS-18-4	Cal-III	2201	0.26	10909	######	#####	#####	0.7063	#####	6.0
HZKS-18-5	Cal-III	1487	0.01	8103	######	#####	#####	0.7062	#####	6.9
HZKS-1-32-1	Cal-III	2135	0.05	11430	######	#####	#####	0.7062	#####	3.2
HZKS-1-32-3	Cal-III	1704	b.d.	10571	b.d.	#####	#####	0.7062	#####	3.2
HZKS-1-32-4	Cal-III	1358	0.03	8910	######	#####	#####	0.7063	#####	3.2
HZKS-1-38-1	Cal-III	1478	0.03	11669	######	#####	#####	0.7061	#####	6.5
HZKS-1-38-2	Cal-III	1826	0.50	11169	######	#####	#####	0.7067	#####	5.5
HZKS-1-38-3	Cal-III	1805	0.02	7718	######	#####	#####	0.7061	#####	5.8
HZKS-1-38-4	Cal-III	1808	0.26	10088	######	#####	#####	0.7061	#####	6.9
HZKS-1-38-5	Cal-III	1507	0.10	9085	######	#####	#####	0.7062	#####	2.4

HZKS-1-39-1	Cal-III	1996	0.19	10672	######	#####	#####	0.7061	#####	1.5
HZKS-1-39-2	Cal-III	1894	b.d.	14159	b.d.	#####	#####	0.7062	#####	4.9
HZKS-1-39-3	Cal-III	2249	0.13	14931	######	#####	#####	0.7060	#####	6.0
HZKS-1-2A-1	Cal-IV	1082	0.50	9126	######	#####	#####	0.7062	#####	6.5
HZKS-1-2A-2	Cal-IV	1460	0.88	9851	######	#####	#####	0.7061	#####	6.8
HZKS-1-2A-3	Cal-IV	1549	0.05	6105	######	#####	#####	0.7062	#####	3.9
HZKS-1-2A-4	Cal-IV	895	0.00	6264	######	#####	#####	0.7062	#####	4.6
HZKS-1-2A-5	Cal-IV	845	0.00	7698	######	#####	#####	0.7063	#####	4.2
HZKS-1-10B-1	Cal-IV	1166	0.01	9568	######	#####	#####	0.7062	#####	5.6
HZKS-1-10B-2	Cal-IV	1210	0.05	9404	######	#####	#####	0.7063	#####	6.0
HZKS-1-10B-3	Cal-IV	1436	0.00	8639	######	#####	#####	0.7065	#####	5.9
HZKS-1-10B-4	Cal-IV	1416	0.02	10705	######	#####	#####	0.7061	#####	8.6
HZKS-1-10B-5	Cal-IV	818	0.06	6182	######	#####	#####	0.7065	#####	3.0
HZKS-1-10B-6	Cal-IV	845	0.00	6344	######	#####	#####	0.7063	#####	5.1
HZKS-1-15-1	Cal-IV	1851	0.85	10216	######	#####	#####	0.7063	#####	5.1
HZKS-1-15-2	Cal-IV	1334	0.03	7160	######	#####	#####	0.7062	#####	7.0
HZKS-1-15-3	Cal-IV	1744	0.03	5545	######	#####	#####	0.7062	#####	5.4
HZKS-1-15-7	Cal-IV	1627	0.03	8096	######	#####	#####	0.7064	#####	5.1
HZKS-1-15-8	Cal-IV	1288	0.01	7485	######	#####	#####	0.7064	#####	5.8
HZKS-1-26-1	Cal-IV	1242	0.77	10399	######	#####	#####	0.7060	#####	6.1
HZKS-1-26-	Cal-IV	1778	0.08	12348	######	#####	#####	0.7059	#####	6.2

2					#	#	#	4	#	
HZKS-1-26-3	Cal-IV	1727	0.07	12029	######	#####	#####	0.70606	#####	8.3
HZKS-1-26-4	Cal-IV	1247	0.01	10419	######	#####	#####	0.70585	#####	8.1
HZKS-1-26-5	Cal-IV	1413	0.05	8806	######	#####	#####	0.70603	#####	5.9
HZKS-1-31-1	Cal-IV	1591	0.03	14190	######	#####	#####	0.70605	#####	8.9
HZKS-1-31-2	Cal-IV	827	0.23	8403	######	#####	#####	0.70607	#####	7.8
HZKS-1-31-3	Cal-IV	1352	0.48	13035	######	#####	#####	0.70609	#####	7.3
HZKS-1-31-4	Cal-IV	2775	0.63	14242	######	#####	#####	0.70630	#####	7.7
HZKS-1-31-5	Cal-IV	1489	0.35	7244	######	#####	#####	0.70618	#####	6.5
HZKS-1-31-6	Cal-IV	1956	0.50	7432	######	#####	#####	0.70604	#####	7.0
HZKS-1-31-7	Cal-IV	1012	0.19	10858	######	#####	#####	0.70609	#####	7.1
HZKS-1-31-8	Cal-IV	1126	0.02	7282	######	#####	#####	0.70615	#####	6.5
HZKS-1-31-9	Cal-IV	1385	0.10	8155	######	#####	#####	0.70597	#####	5.6
HZKS-1-31-10	Cal-IV	1079	0.13	6929	######	#####	#####	0.70660	#####	6.2
HZKS-1-31-11	Cal-IV	2099	0.05	14643	######	#####	#####	0.70630	#####	6.8
HZKS-1-31-12	Cal-IV	2576	0.06	15274	######	#####	#####	0.70625	#####	6.8

1622 b.d. = below detection limit

1623

1624

1625

1626 **Table 4.** In-situ C isotopic compositions of calcite from carbonatite I, II, and the

1627 contact zone from the HZKS-1 drill core at Maoniuping.

Sample/ spot	Mineral	$^{13}C/^{12}C$ ture	σ	C intensity (V)	$\delta^{13}C_{PBD}$(‰)
HZKS-1-6-1	Cal-I	##########	0.0000016	14.34	-6.70
HZKS-1-6-2	Cal-I	##########	0.0000015	14.50	-6.01
HZKS-1-6-3	Cal-I	##########	0.0000025	14.52	-6.28
HZKS-1-6-4	Cal-I	##########	0.0000033	14.31	-5.46
HZKS-1-6-5	Cal-I	##########	0.0000015	14.17	-3.28
HZKS-1-6-6	Cal-I	##########	0.0000033	14.28	-4.74
HZKS-1-7-1	Cal-I	##########	0.0000012	15.83	-5.61
HZKS-1-7-2	Cal-I	##########	0.0000021	14.68	-5.73
HZKS-1-7-3	Cal-I	##########	0.0000014	15.67	-6.55
HZKS-1-7-5	Cal-I	##########	0.0000014	15.98	-6.05
HZKS-1-17-1	Cal-I	##########	0.0000016	16.87	-5.14
HZKS-1-17-2	Cal-I	##########	0.0000013	16.81	-5.61
HZKS-1-17-3	Cal-I	##########	0.0000015	16.42	-5.69
HZKS-1-17-4	Cal-I	##########	0.0000015	16.34	-5.30
HZKS-1-17-5	Cal-I	##########	0.0000013	16.38	-4.51
HZKS-1-17-6	Cal-I	##########	0.0000011	16.55	-4.07
HZKS-1-17-7	Cal-I	##########	0.0000012	16.18	-5.64

HZKS-1-17-8	Cal-I	##########	0.0000012	16.16	-4.65
HZKS-1-17-9	Cal-I	##########	0.0000018	11.87	-6.55
HZKS-1-22-1	Cal-I	##########	0.0000018	14.78	-6.21
HZKS-1-22-3	Cal-I	##########	0.0000015	14.84	-5.76
HZKS-1-22-4	Cal-I	##########	0.0000020	14.60	-5.36
HZKS-1-22-7	Cal-I	##########	0.0000015	14.58	-6.01
HZKS-1-22-8	Cal-I	##########	0.0000014	14.51	-5.74
HZKS-1-22-9	Cal-I	##########	0.0000019	14.73	-6.16
HZKS-1-22-11	Cal-I	##########	0.0000019	14.45	-5.36
HZKS-1-2B-1	Cal-II	##########	0.0000026	14.23	-6.87
HZKS-1-2B-2	Cal-II	##########	0.0000022	14.25	-5.71
HZKS-1-2B-3	Cal-II	##########	0.0000022	14.34	-6.10
HZKS-1-2B-4	Cal-II	##########	0.0000020	13.46	-6.14
HZKS-1-2B-7	Cal-II	##########	0.0000022	14.13	-7.19
HZKS-1-2B-8	Cal-II	##########	0.0000018	13.56	-6.63
HZKS-1-2B-9	Cal-II	##########	0.0000023	13.94	-6.50
HZKS-1-2B-10	Cal-II	##########	0.0000025	14.05	-7.16
HZKS-1-5A-1	Cal-II	##########	0.0000037	14.27	-7.91
HZKS-1-5A-2	Cal-II	##########	0.0000014	14.28	-4.67
HZKS-1-5A-3	Cal-II	##########	0.0000013	14.35	-5.20
HZKS-1-5A-4	Cal-II	##########		14.29	-5.43

			0.0000019		
HZKS-1-5A-5	Cal-II	##########	0.0000014	16.21	-7.00
HZKS-1-5B-1	Cal-II	##########	0.0000017	10.92	-6.28
HZKS-1-5B-2	Cal-II	##########	0.0000020	10.87	-6.03
HZKS-1-5B-3	Cal-II	##########	0.0000019	10.73	-6.01
HZKS-1-5B-4	Cal-II	##########	0.0000017	10.75	-5.24
HZKS-1-5B-6	Cal-II	##########	0.0000025	9.95	-5.73
HZKS-1-10A-1	Cal-II	##########	0.0000016	16.87	-7.77
HZKS-1-10A-2	Cal-II	##########	0.0000018	17.77	-6.58
HZKS-1-10A-3	Cal-II	##########	0.0000012	16.42	-6.08
HZKS-1-10A-4	Cal-II	##########	0.0000012	16.76	-5.95
HZKS-1-10A-5	Cal-II	##########	0.0000013	16.49	-6.22
HZKS-1-10A-6	Cal-II	##########	0.0000015	16.24	-5.86

1628 (continued)

1629 Table 4 continued

Sample/ spot	**Mineral**	**$^{13}C/^{12}C$ ture**	**σ**	**C intensity (V)**	**$\delta^{13}C_{PBD}$(‰)**
HZKS-1-4-1	Cal-III	##########	0.0000031	14.35	-8.20
HZKS-1-4-2	Cal-III	##########	0.0000015	16.18	-7.94
HZKS-1-4-3	Cal-III	##########	0.0000019	16.04	-7.34
HZKS-1-4-4	Cal-III	##########	0.0000013	16.22	-7.16
HZKS-1-4-5	Cal-III	##########		14.29	-7.93

			0.0000027		
HZKS-1-13-1	Cal-III	##########	0.0000015	17.81	-6.92
HZKS-1-13-2	Cal-III	##########	0.0000016	17.93	-7.32
HZKS-1-13-4	Cal-III	##########	0.0000014	17.39	-7.77
HZKS-1-13-5	Cal-III	##########	0.0000017	17.11	-6.77
HZKS-18-3	Cal-III	##########	0.0000017	17.14	-9.97
HZKS-18-4	Cal-III	##########	0.0000014	16.97	-8.09
HZKS-18-5	Cal-III	##########	0.0000024	8.82	-8.14
HZKS-1-32-1	Cal-III	##########	0.0000011	15.80	-6.91
HZKS-1-32-3	Cal-III	##########	0.0000015	15.63	-7.92
HZKS-1-32-4	Cal-III	##########	0.0000013	15.66	-6.55
HZKS-1-38-1	Cal-III	##########	0.0000012	15.60	-6.92
HZKS-1-38-2	Cal-III	##########	0.0000014	15.90	-5.84
HZKS-1-38-3	Cal-III	##########	0.0000013	15.73	-7.08
HZKS-1-38-4	Cal-III	##########	0.0000014	15.59	-7.05
HZKS-1-38-5	Cal-III	##########	0.0000013	16.30	-6.71
HZKS-1-39-1	Cal-III	##########	0.0000017	16.45	-6.78
HZKS-1-39-2	Cal-III	##########	0.0000017	16.65	-7.25
HZKS-1-39-3	Cal-III	##########	0.0000015	16.42	-7.46
HZKS-1-2A-1	Cal-IV	##########	0.0000028	9.39	-6.38
HZKS-1-2A-2	Cal-IV	##########	0.0000026	9.13	-6.81

HZKS-1-2A-3	Cal-IV	##########	0.0000022	8.91	-7.67
HZKS-1-2A-4	Cal-IV	##########	0.0000032	9.55	-5.14
HZKS-1-10B-1	Cal-IV	##########	0.0000016	16.95	-7.43
HZKS-1-10B-2	Cal-IV	##########	0.0000015	15.52	-7.87
HZKS-1-10B-3	Cal-IV	##########	0.0000017	16.39	-7.44
HZKS-1-10B-4	Cal-IV	##########	0.0000014	17.06	-5.96
HZKS-1-10B-5	Cal-IV	##########	0.0000015	16.38	-6.65
HZKS-1-10B-6	Cal-IV	##########	0.0000015	16.60	-5.87
HZKS-1-15-1	Cal-IV	##########	0.0000016	16.81	-7.17
HZKS-1-15-2	Cal-IV	##########	0.0000021	16.78	-7.03
HZKS-1-15-3	Cal-IV	##########	0.0000014	17.34	-6.72
HZKS-1-26-1	Cal-IV	##########	0.0000016	17.05	-6.18
HZKS-1-26-2	Cal-IV	##########	0.0000017	16.76	-8.61
HZKS-1-26-3	Cal-IV	##########	0.0000016	16.74	-6.32
HZKS-1-26-4	Cal-IV	##########	0.0000015	16.63	-6.73
HZKS-1-31-1	Cal-IV	##########	0.0000014	15.75	-5.55
HZKS-1-31-2	Cal-IV	##########	0.0000015	15.70	-5.95
HZKS-1-31-3	Cal-IV	##########	0.0000018	15.83	-6.35
HZKS-1-31-4	Cal-IV	##########	0.0000012	15.55	-4.78
HZKS-1-31-5	Cal-IV	##########	0.0000015	15.47	-5.64
HZKS-1-31-6	Cal-IV	##########		15.11	-5.35

			0.0000018		
HZKS-1-31-7	Cal-IV	##########	0.0000015	15.12	-6.05
HZKS-1-31-8	Cal-IV	##########	0.0000016	15.64	-6.74
HZKS-1-31-9	Cal-IV	##########	0.0000014	15.34	-6.28
HZKS-1-31-10	Cal-IV	##########	0.0000015	15.46	-5.83
HZKS-1-31-11	Cal-IV	##########	0.0000017	15.33	-5.41
HZKS-1-31-12	Cal-IV	##########	0.0000017	14.80	-6.43

1630

1631

1632

1633

1634

1635

1636

1637

1638

1639

1640

1641

1642

FIGURE CAPTIONS

Fig. 1. Geology and location maps of the Maoniuping deposit. (a) Regional tectonic map of China, showing the eastern Tibetan orogen (outlined red). (b) Simplified tectonic map of eastern Tibetan Orogen (modified after Yin & Harrison, 2000; Hou and Cook, 2009), including the Mianning–Dechang REE belt (yellow square) and the location of the Maoniuping deposit (highlighted in red). (c) Detailed geological map of the Maoniuping deposit displaying an overview of the carbonatite-nordmarkite complexes (modified from Yuan et al., 1995). The Dagudao and Guangtoushan sections are highlighted by dashed blue lines.

Fig. 2. Drill core section of HZKS-1 from 0 to 1100 m showing lithologies, sampling positions, and the distribution of REE mineralization.

Fig. 3. Representative photos of investigated samples from the HZKS-1 drill core. (a) Fresh fine-grained, gray nordmarkite. (b) Altered nordmarkite with fenitization and hematization. (c) Alkaline granite containing quartz, K-feldspar and interstitial clinopyroxene and mica. (d) Contact zone between carbonatites and nordmarkite, including aegirine, arfvedsonite, pseudo-hexagonal phlogopite (Phl-II), K-feldspar as well as bastnäsite-(Ce) aggregates; (e) Reddish and altered granite with carbonation. (f) Nordmarkite crosscut by the carbonatite I. (g and h) Carbonatite I containing calcite (Cal-I) cumulates, disseminated phlogopite (Phl-I) and riebeckite. (i)

1664 Cabonatite I comprising pink calcite (Cal-II) and minor phlogopite (Phl-I). (j)
1665 Nordmarkite crosscut by carbonatite II, which are predominantly calcite cumulates
1666 (Cal-III). (k) Carbonatite II, comprising centimeter-scales calcite (Cal-III), comb-like
1667 phlogopite (Phl-II), purple fluorite, quartz, baryte and bastnäsite-(Ce). Abbreviations:
1668 Aeg = aegirine, Agt = aegirine-augite, Arf = arfvedsonite, Brt = baryte, Bsn =
1669 bastnäsite-(Ce), Cal = calcite, Kfs = K-feldspar, Phl = phlogopite, Py = pyrite, Qtz =
1670 quartz, Rbk = riebeckite.
1671
1672 **Fig. 4. Photomicrographs, optical microscope cathodoluminescence (OP-CL) and**
1673 **backscattered electron (BSE) images of carbonatite I.** (a) Cross-polarized light
1674 image of the fine-grained calcites (Cal-I), showing polygonal mosaic texture. (b)
1675 Plane-polarized light image showing primary phlogopite (Phl-I) with riebeckite
1676 aggregates. (c) Euhedral calcites from a thick section, showing colorful extinction in
1677 cross-polarized light. (d) Plane-polarized light and BSE (yellow square) images of
1678 needle-like molybdenite aggregates with inhomogeneous distribution in calcites. (e)
1679 BSE image of the calcite cumulates. (f) Euhedral riebeckite inclusions enclosed in
1680 primary phlogopite (Phl-I). (g) BSE image of carbonatite I at depth of 929 m, showing
1681 Cal-II hosting bastnäsite-(Ce) inclusions. (h) BSE image showing part of Fig. 6g
1682 where bastnäsite-(Ce) inclusions exhibit cleavage-aligned trails within Cal-II. (i)
1683 Optical CL image of homogeneous calcite grains with bright orange to blood-red

luminescence and slight core-rim zoning. Abbreviations: Fl = fluorite, Mol = molybdenite; others are the same with those Fig. 3.

Fig. 5. Photomicrographs of representative textures and mineral assemblages of the carbonatite II from the HZKS-1 drill core. (a) Plane-polarized image of coarse-grained calcites (Cal-III) that occur with elliptic purple fluorite and contain baryte along fractures. (b) Plane-polarized image of coarse-grained fluorite and porous baryte distributed with anhedral calcites, both of which are intergrown with comb-like bastnäsite-(Ce) aggregates. (c) Plane-polarized image showing euhedral needle-like arfvedsonite and patchy aegirine associated with coarse-grained calcites (Cal-III). (d) Plane-polarized image of inequigranular texture of the carbonatite II, showing deformation in the brittle-ductile transition regime. (e) Cross-polarized image of interstitial phlogopite crystals along amoeboid calcite grain boundaries. (f) Cross-polarized image of elongated calcite crystals extending over 2 mm in certain orientations. (g) Cross-polarized image showing a curved boundary between coarse-grained calcites (Cal-III) that exhibit bent and thick-twinned lamellae. (h) BSE image of gray fluorite and calcite crosscut by late baryte. (i) BSE image of acicular arfvedsonite, Cal-III and patchy aegirine and anhedral quartz with large pores and intergrown with baryte and bastnäsite-(Ce). (j) Parisite-(Ce) and bastnäsite-(Ce) with patchy zoning under BSE image. (k) Coarse-grained calcites showing flame-like core

fading to dark orange rim under OP-CL. Abbreviations as in Fig. 3; Fl = fluorite, par = parisite-(Ce).

Fig. 6. Representative photomicrographs (plane-, and cross-polarized light) and BSE images of the contact zones. (a) Characteristic carbonatite-wall rock contact with large proportion of silicate minerals (phlogopite, aegirine, arfvedsonite, microcline) and REE mineralization. (b) Euhedral core-rim zoned phlogopite (Phl-II) enclosed in calcite (Cal-IV) matrix. (c) Part of Fig. 6g where pseudo-hexagonal aegirine is surrounded by arfvedsonite aggregates and less-porous baryte. (d) Local area of Fig. 6b showing phlogopite with dark gray to light gray core-to-rim zoning, arfvedsonite inclusions, and surrounding euhedral arfvedsonite aggregates. (e) Euhedral laths of bastnäsite-(Ce) showing planar boundary with calcites. (f) Porous baryte and patchy aegirine distributed along margin of bastnäsite-(Ce) crystals. (g) Phlogopite, quartz, and aegirine in proximity to bastnäsite-(Ce) and surrounded by porous baryte. Abbreviations as shown in Fig. 3, and Mc = microcline.

Fig. 7. Chondrite-normalized whole-rock REE patterns for the carbonatite I and II, nordmarkite, and alkali granite (chondrite values from McDonough & Sun, 1995).

Fig. 8. Major compositions of the four generations of calcites in carbonatite I, II and the contact zone as box plot diagrams. The star symbols represent outliers.

Fig. 9. Chemical variations of the four generations of calcites in carbonatite I, II and the contact zone. R^2 means the linear correlation coefficient.

Fig. 10. Trace element compositions of calcites from carbonatite I, II and the contact zone as determined by LA-ICP-MS. (a) Chondrite-normalized REE patterns of four calcite generations (green dashed outline is REE patterns of Cal-IV; chondrite values from McDonough & Sun, 1995). (b) $(La/Sm)_N$ versus Y/Ho scatter diagrams (CHARAC field from Bau, 1996).

Fig. 11. Compositional variation of micas from carbonatite I, nordmarkite and the contact zone. (a) Binary of Mg + Si versus $^{IV}Al + {}^{VI}Al$ (tetrahedral and octahedral occupancy in a.p.f.u.). Dashed line representing phlogopite–eastonite substitution trend. (b) and (c) Fe / (Fe + Mg) (molar ratios) and Al versus Ti, respectively. (d) to (f) Ti, Na, Mn versus Mg#, respectively. (g) and (h) Na versus K and F, respectively. (i) Mg# versus IV(F).

Fig. 12. Bulk C and O isotopic compositions of calcite from carbonatite I, II, and the contact zone from the HZKS-1 drill core. (a) $\delta^{13}C$ versus $\delta^{18}O$ plots of calcite

showing a comparison between Maoniuping and other carbonatites. Typical trend 1, 2 and 3 for magmatic fluid-carbonate interaction, magma fluid-carbonate interaction plus minor decarbonation, and pure decarbonation, respectively (Whitley et al., 2019). (b) $\delta^{13}C$ versus $\delta^{18}O$ plots of calcite from Maoniuping carbonatites (PIC (Primary Igneous Carbonatite) and mantle fields from Taylor et al., 1967 and Deines, 1992, respectively). Comparative C–O isotopic data including Mianning-Dechang belt (e.g., Maoniuping (Yang et al., 1998; Niu et al., 2002; Xu et al., 2003; Hou et al., 2006, 2015), Dalucao and Lizhuang (Liu & Hou, 2017), Miaoya (Xu et al., 2014; Ying et al., 2020), Bayan Obo (Yang et al., 2009), and Qieganbulake (Ye et al., 2013) carbonatites.

Fig. 13. The in-situ Sr isotopic variation of the four calcite generations at Maoniuping. The ranges of whole-rock $^{87}Sr/^{86}Sr$ ratios for nordmarkite and carbonatite from Wang et al. (2001), Xu et al. (2003), and Hou et al. (2006, 2015).

Fig. 14. Modal calculations of equilibrium and fractional crystallization showing differentiation degree of carbonatitic magma. (a) Equilibrium crystallization modeling trends. (b) to (d) Fractional crystallization modeling with variable calcite:amphibole:fluorite ratios and differentiation increments (ΔF) of 0.01, 0.05 and 0.1. Whole-rock compositions based on samples HZKS-1-22 (orange curve), HZKS-1-17 (purple curve), and HZKS-1-6 (black curve). F is degree of fractional

crystallization of carbonatite melt. Stars represent calculated results. All other symbols represent measured data of the four calcite generations.

Fig. 15. The schematic chemical variation of trace element compositions of calcite in carbonatite I, II and the contact zone from the HZKS-1 drill core. (a) δEu versus δCe. (b and c) Chondrite-normalized diagrams of REE versus $(La/Yb)_N$ and $(La/Yb)_N$ versus Y/Ho, respectively (chondrite values from McDonough and Sun, 1995). (d) Sr/Y versus Y/Y*. Trace-element compositions of calcites for comparison are selected from Oka (Chen & Simonetti, 2013), Miaoya (Ying et al., 2020), Dalucao (Liu & Hou, 2017), and Muluozhai (Zheng et al., 2021). Other calcite data of global carbonatites and typical trend for magma fractionation, hydrothermal reworking and supergene oxidation in are compilated from Chakhmouradian et al. (2016b).

Fig. 16. Monte Carlo simulations of Sr isotopic compositions and relationship to Sr and REE concentrations, indicating more radiogenic $^{87}Sr/^{86}Sr$ ratios in calcites from carbonatite II and contact zone requires the ~40% contamination with nodrmarkite. In modal calculation, randomly input selecting values set 4×10^8. The initial $^{87}Sr/^{86}Sr$ ratios of are 0.70605 for carbonatites according to our analyses of Cal-I and 0.70686–0.70700 for nordmarkite (Xu et al., 2003; Hou et al., 2006). Based on the whole-rock results of this study and previous research, Sr contents are selected from 8000 to 25000 ppm for carbonatites (Hou et al., 2015) and 500 to 3000 ppm for

nordmarite (Wang et al., 2001); initial REE contents are set from 1000 to 3000 ppm for carbonatites (Wang et al., 2001; Hou et al., 2006) and 200 to 800 ppm for nordmarkite (Xu et al., 2003; Hou et al., 2015).

Fig. 17. The schematic variation of in-situ Sr–C isotopic compositions of calcites. (a) REE versus $^{87}Sr/^{86}Sr$. (b) C–Sr isotopic decoupling trend from initial early-crystalizing to late calcite. (c) REE versus $\delta^{13}C$. (d) An intergrade comparison of $\delta^{13}C$ values among four calcite generations (in-situ), calcite (bulk), bastnäsite-(Ce), carbonatites at Maoniung. The results of bulk C isotopic compositions for calcite are from this study (red) and previous studies (purple; Niu et al., 2002; Xu et al., 2003; Hou et al., 2006, 2015; $\delta^{13}C$ values of bastnäsite-(Ce) and mantle values are from Liu & Hou, 2017, and Deines, 1992, respectively). (e) Chondrite-normalized $(La/Yb)_N$ versus $\delta^{13}C$ (chondrite values from McDonough & Sun, 1995). (f) Raleigh decarbonation modeling illustrating relationship between F_{CO_2} (the mole fraction of C remaining in the melt after decarbonation, Valley, 1986) and C isotopic composition of evolved carbonatitic melt. The initial $\delta^{13}C$ values of carbonatitic melt is taken from the average Cal-I value of –5.3‰ (pink circle).

Fig. 18. A schematic evolutionary model of carbonatitic magma illustrating chemical variation and mineral assemblages during process of fractional crystallization and contamination of carbonatitic melt by silicate wall rock. (a) A

schematic diagram show carbonatite magma ascent (modified from Walter et al., 2021), with carbonatite melt fractional crystallization and contamination by nordmarkite at shallow crust. (b1) Incipient magmatic texture and primary mineral assemblages of carbonatite I that derived from a low degree (F = ~0.9) of fractional crystallization of carbonatitic melt. (b2) Ascent and further fractional crystallization (F = 0.8–0.7) of carbonatite melt cause primary bastnäsite-(Ce) crystallization along cleavage-aligned trails within Cal-II. (b3) Contamination-induced interaction between carbonatite melt and nordmarkite counterparts leads to scavenging of Na, K, and F from carbonatite melt and incorporation of Si and Al from wallrocks by formation of phlogopite, clinopyroxene, microcline, fluorite and bastnäsite-(Ce). (b4) Protracted fractional crystallization (F = 0.6–0.5) and repeated contamination result in huge REE accumulation, decarbonation-triggered carbonatite magma ascent, crystallization of super coarse-grained calcite (Cal-IV) with silicates, and textural deformation of carbonatite II.

Fig. 1.

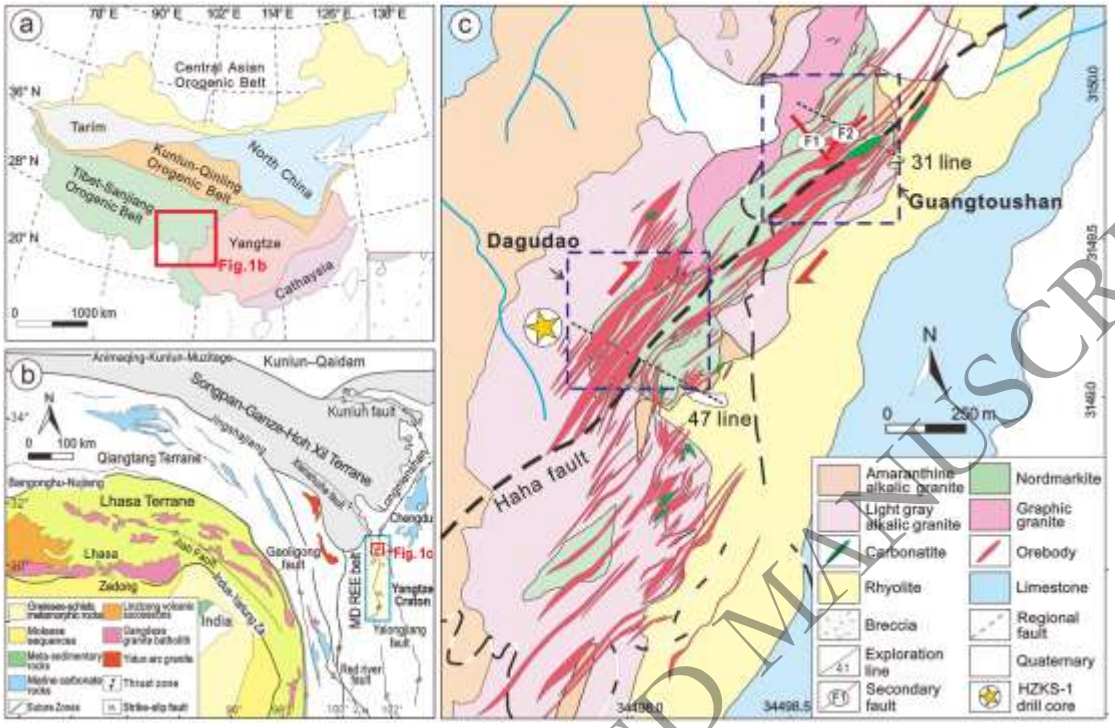

1843 **Fig. 2.**

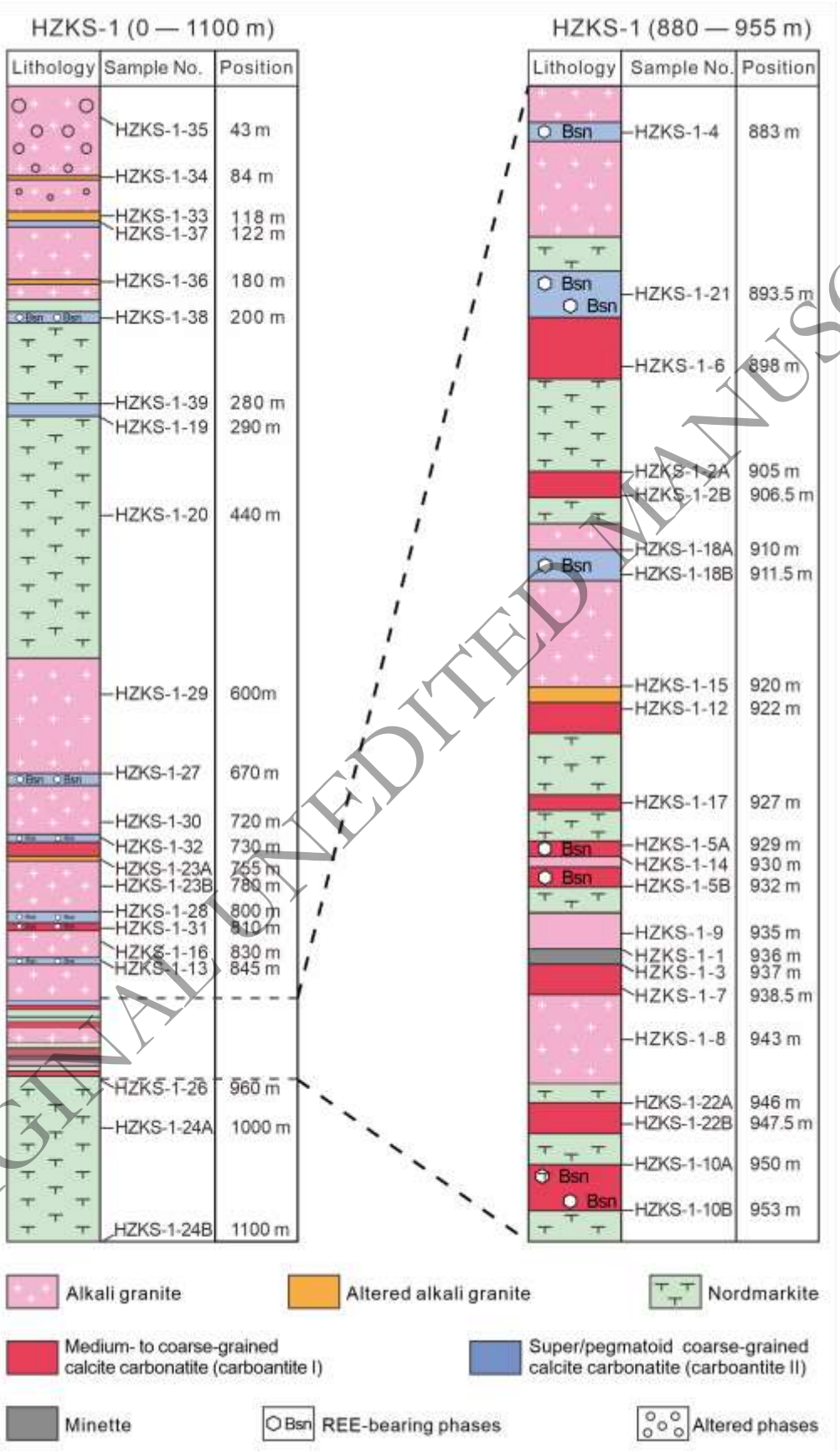

1844

Fig. 3.

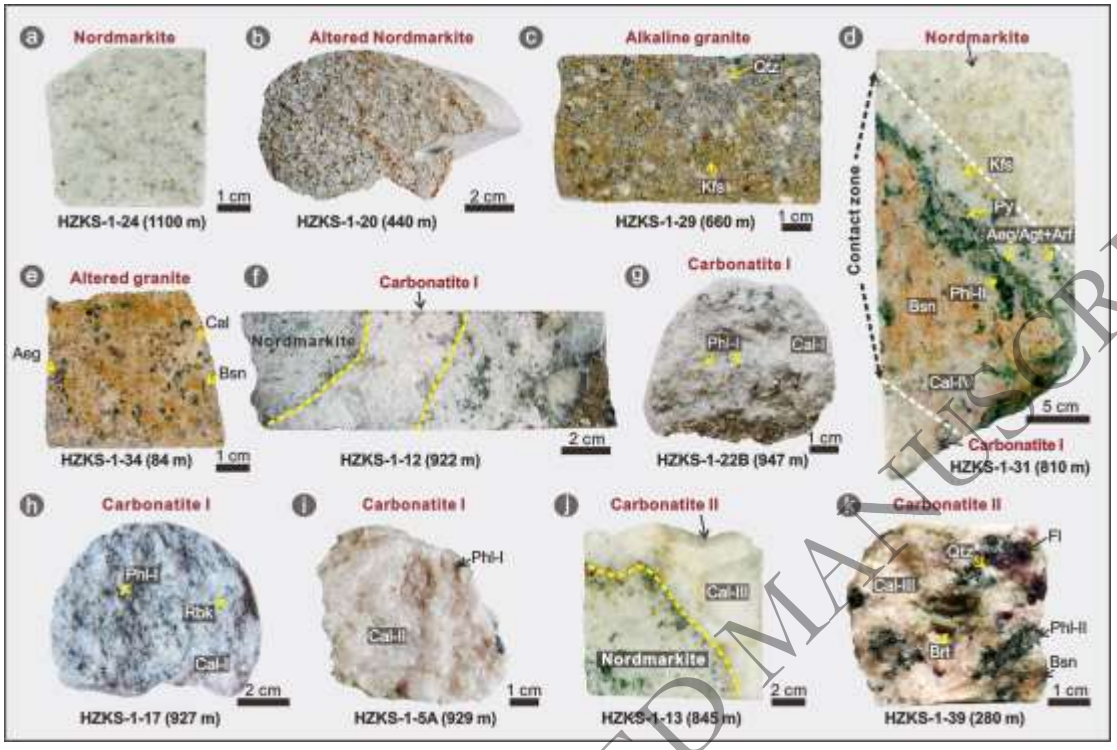

Fig. 4.

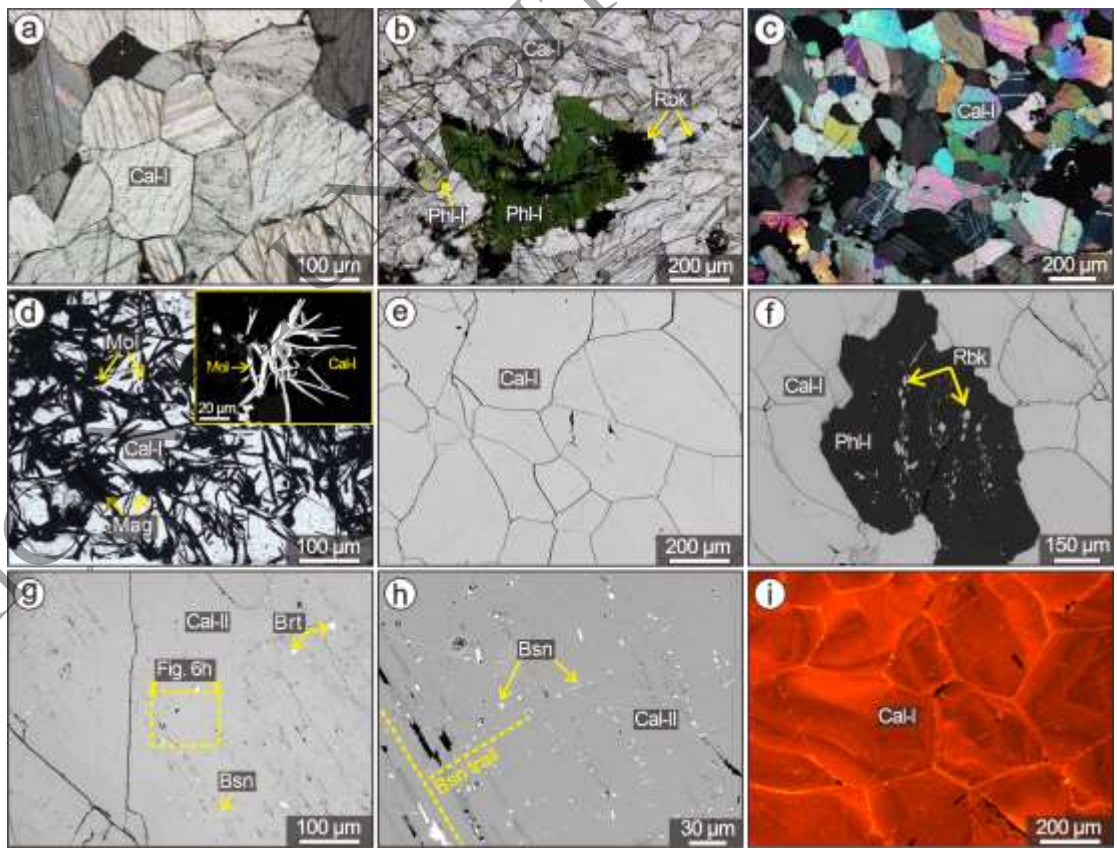

Fig. 5.

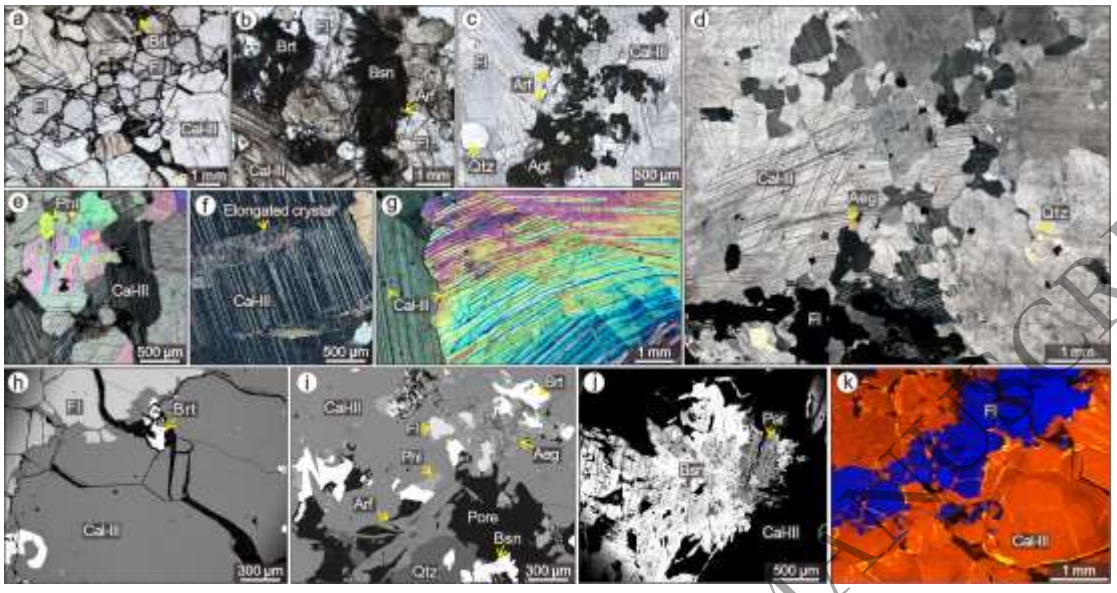

Fig. 6.

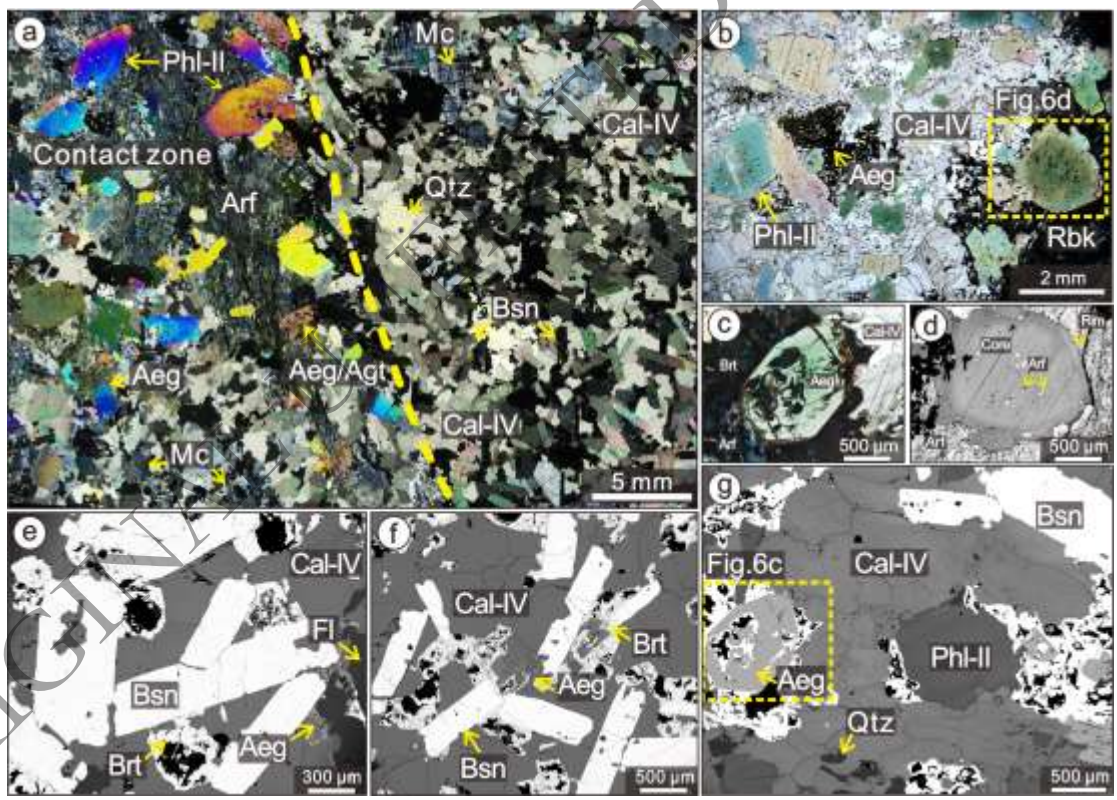

Fig. 7.

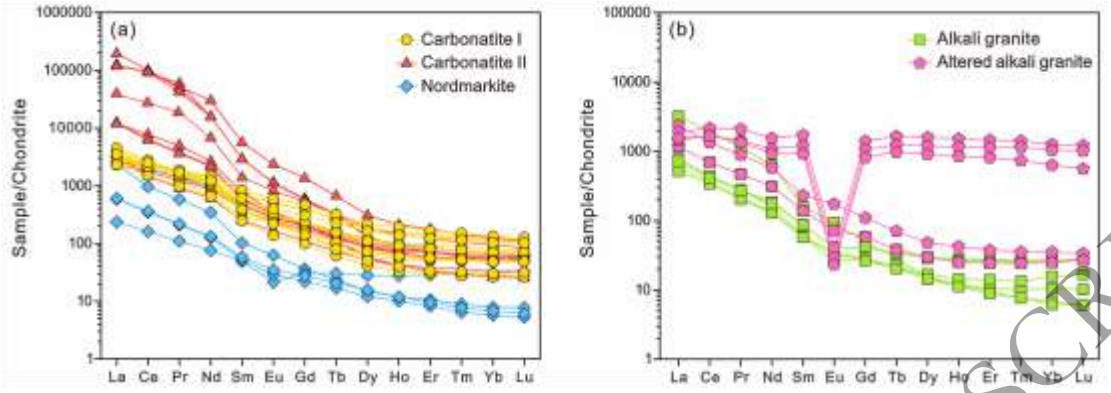

1875 **Fig. 8.**

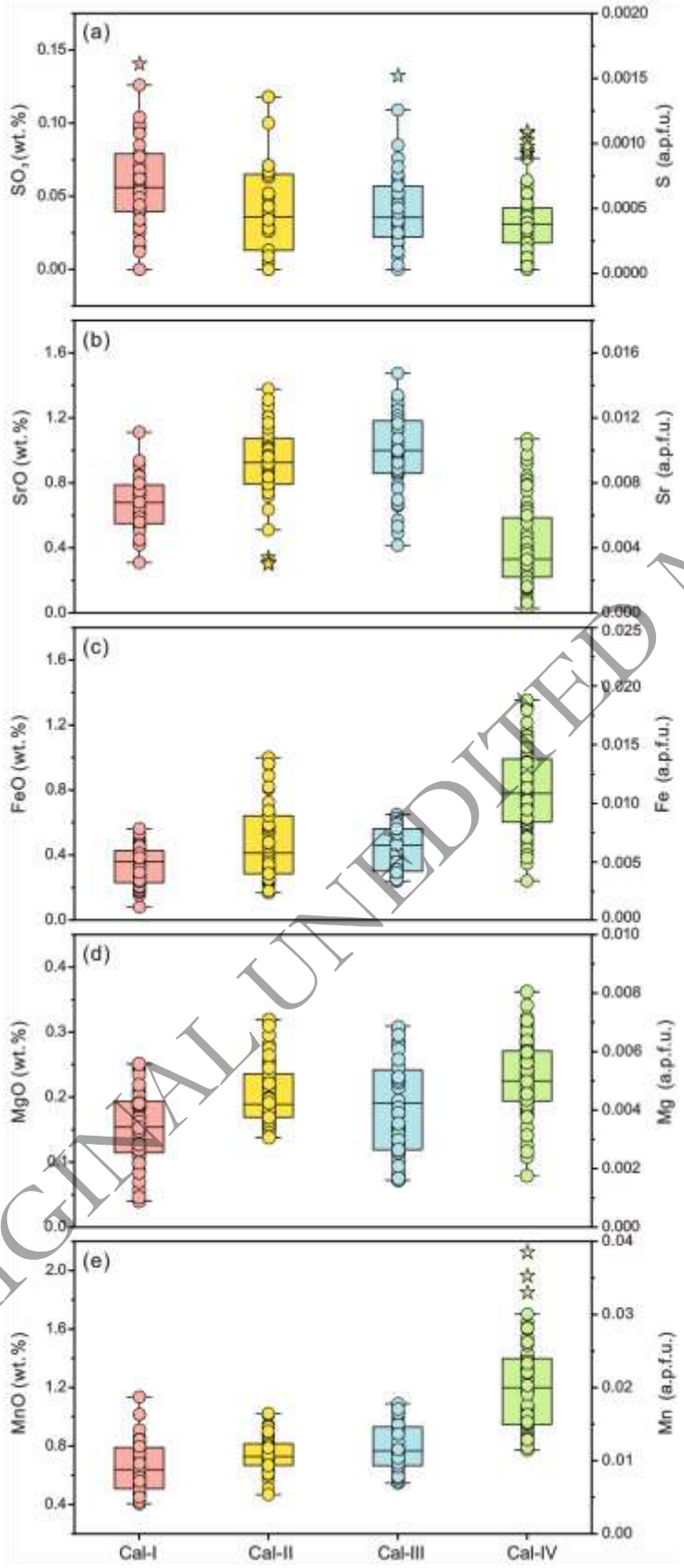

1876

1877 **Fig. 9.**

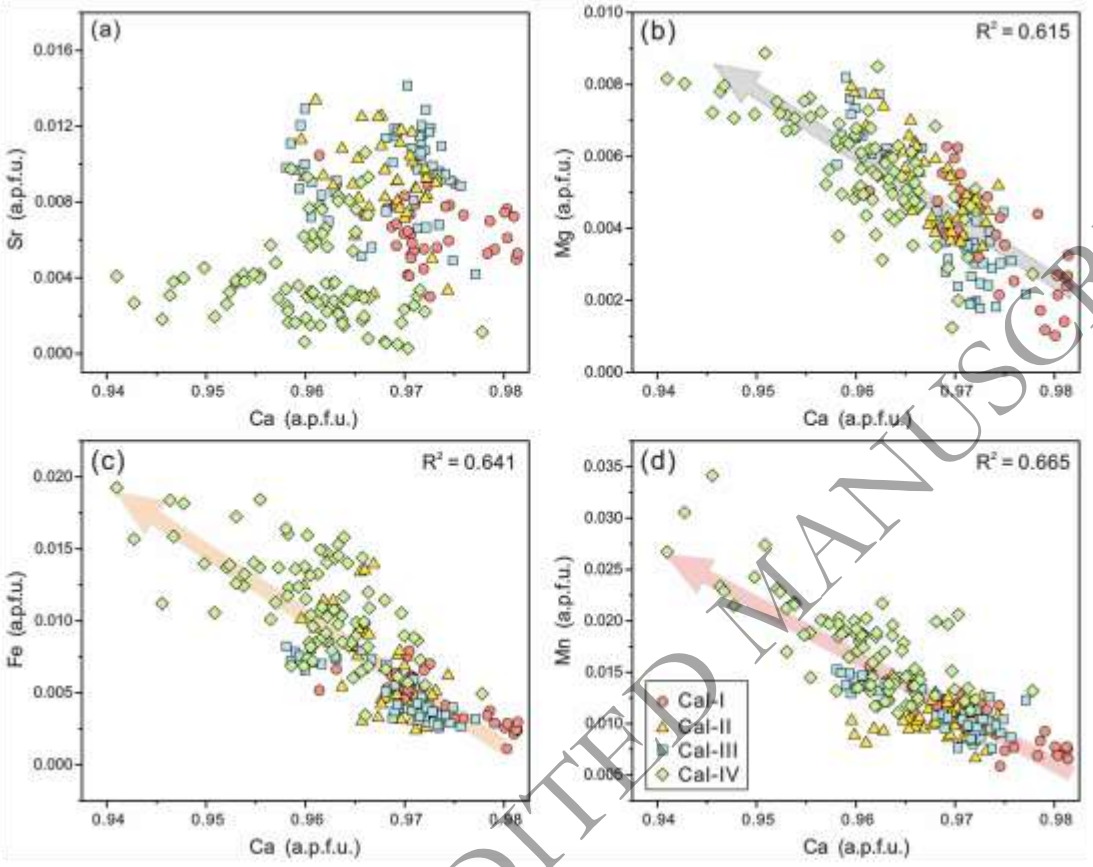

1878

1879

1880

1881

1882

1883

1884

1885

1886

1887

1888

1889 **Fig. 10.**

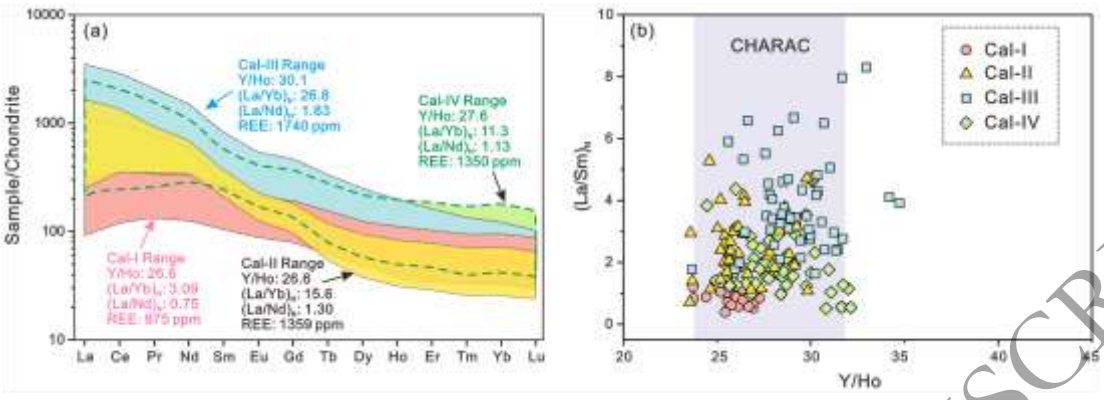

1890

1891

1892 **Fig. 11.**

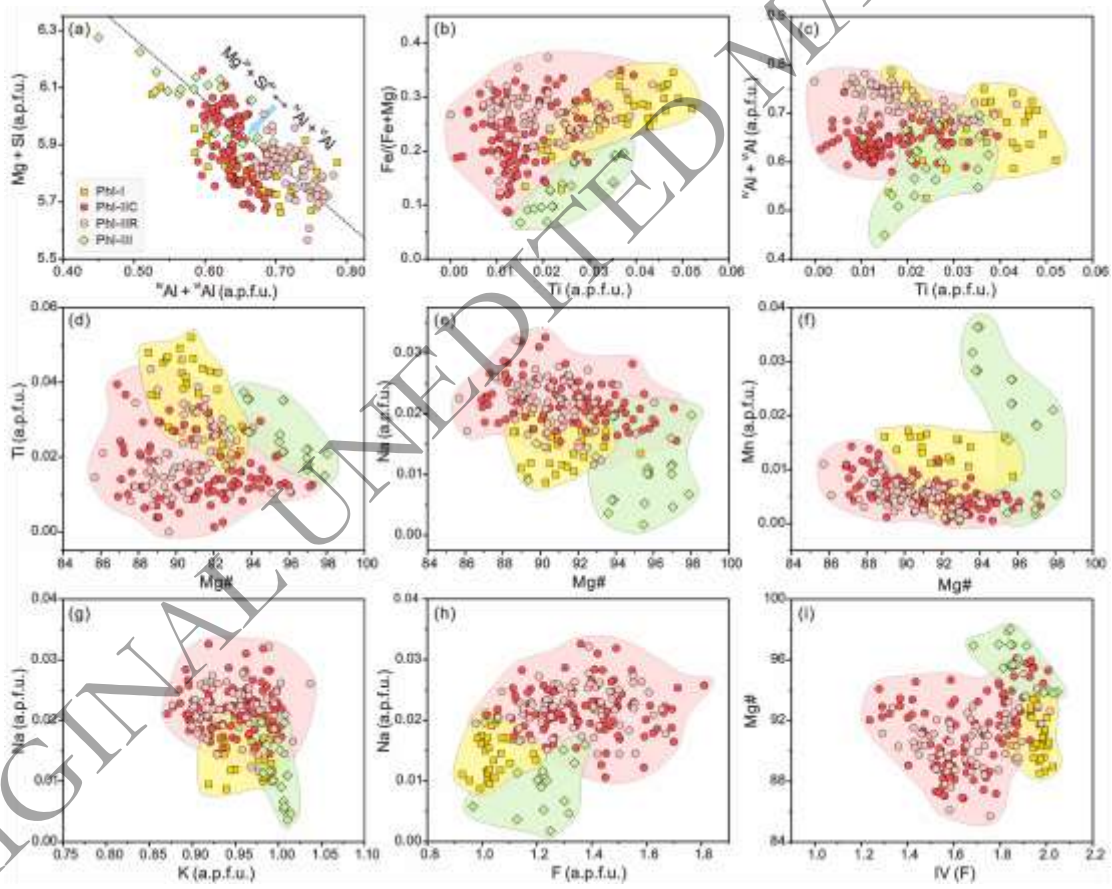

1893

1894

1895

1896

1897 **Fig. 12.**

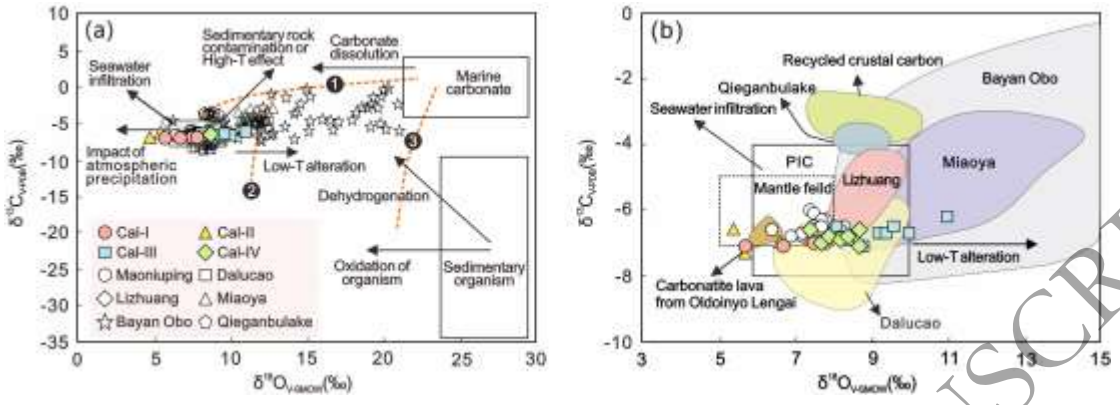

1898

1899

1900 **Fig. 13.**

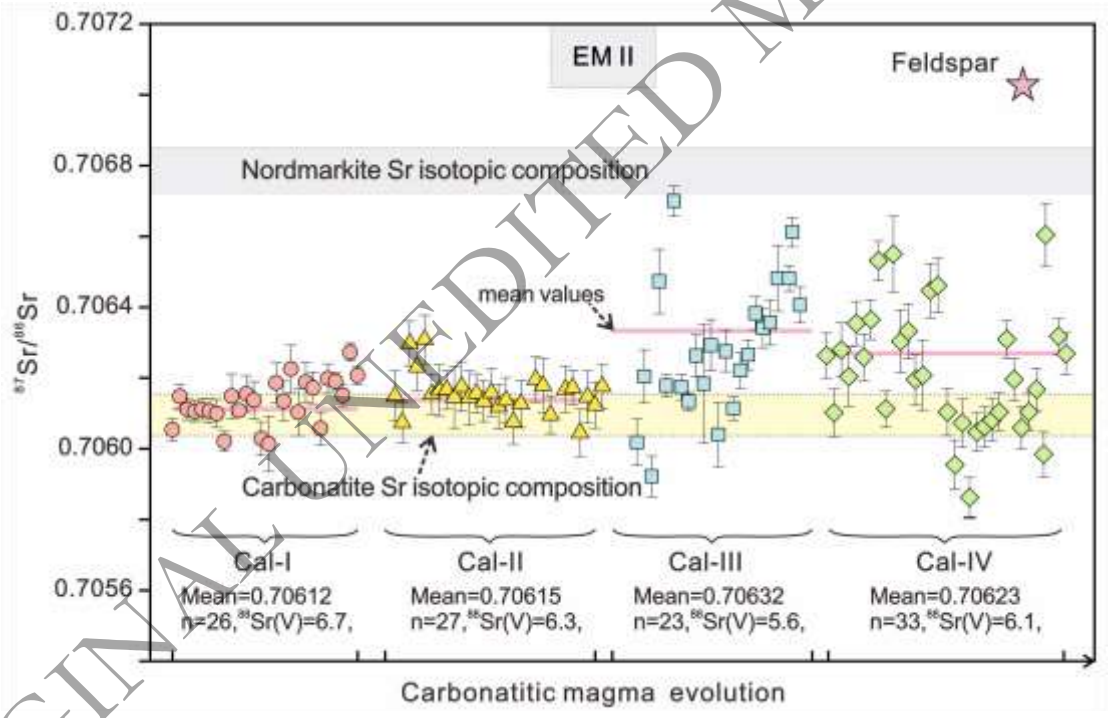

1901

1902

1903

1904

1905

1906

Fig. 14.

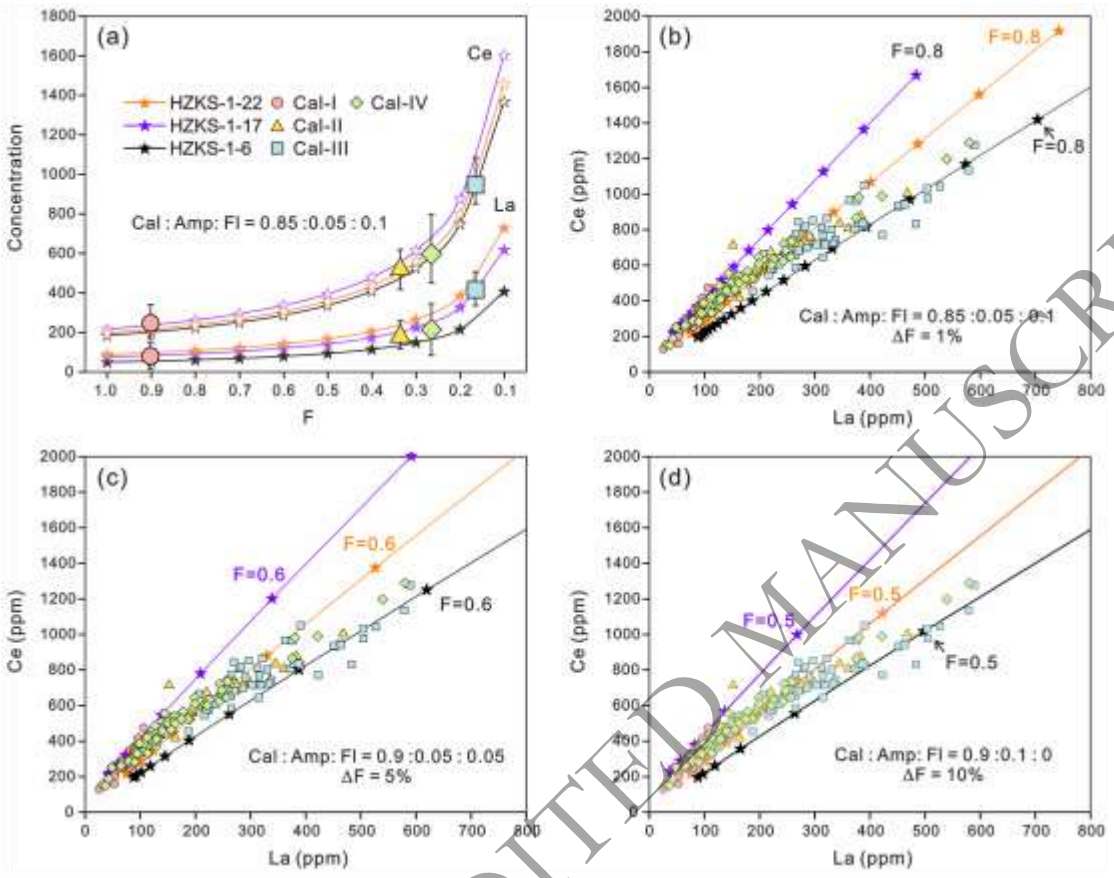

Fig. 15.

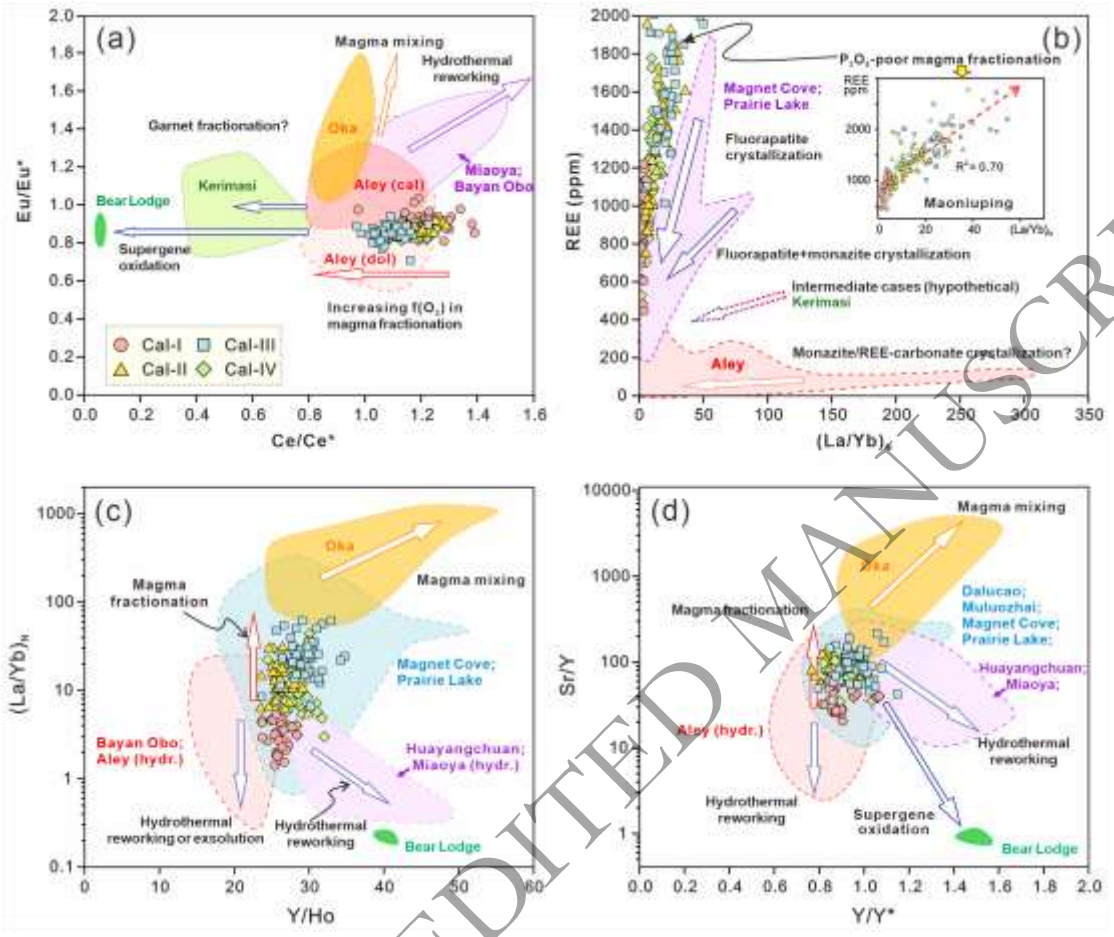

Fig. 16.

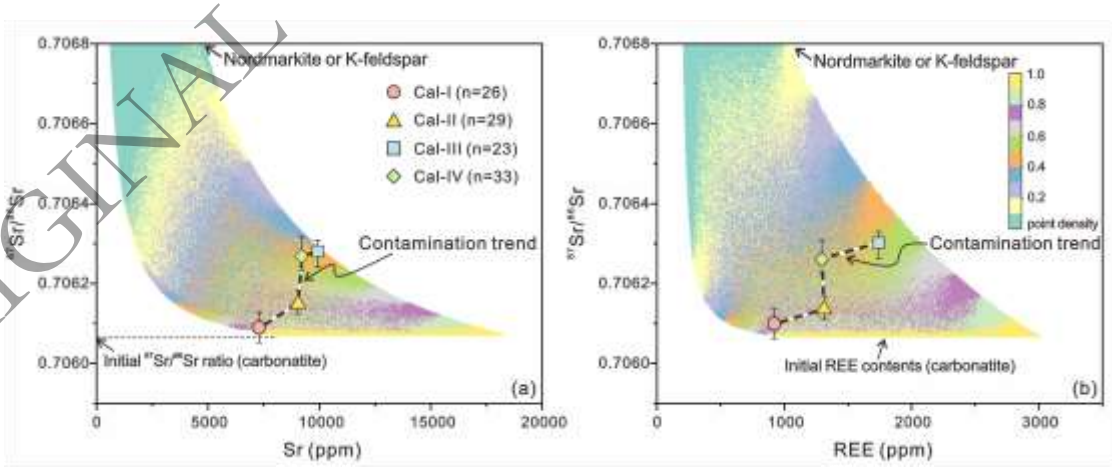

1926 **Fig. 17.**

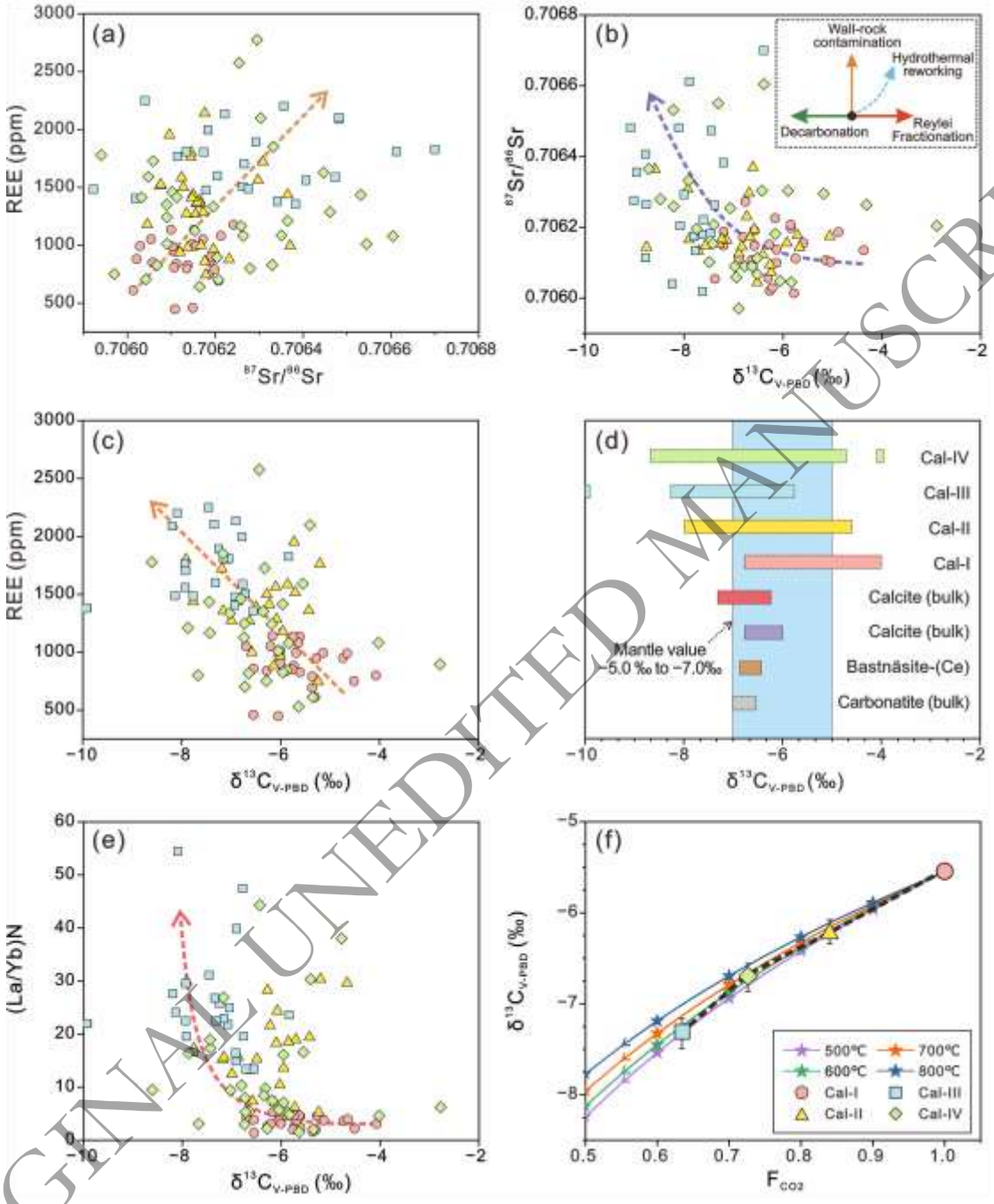

1927

1928

1929

1930

1931

1932 **Fig. 18.**

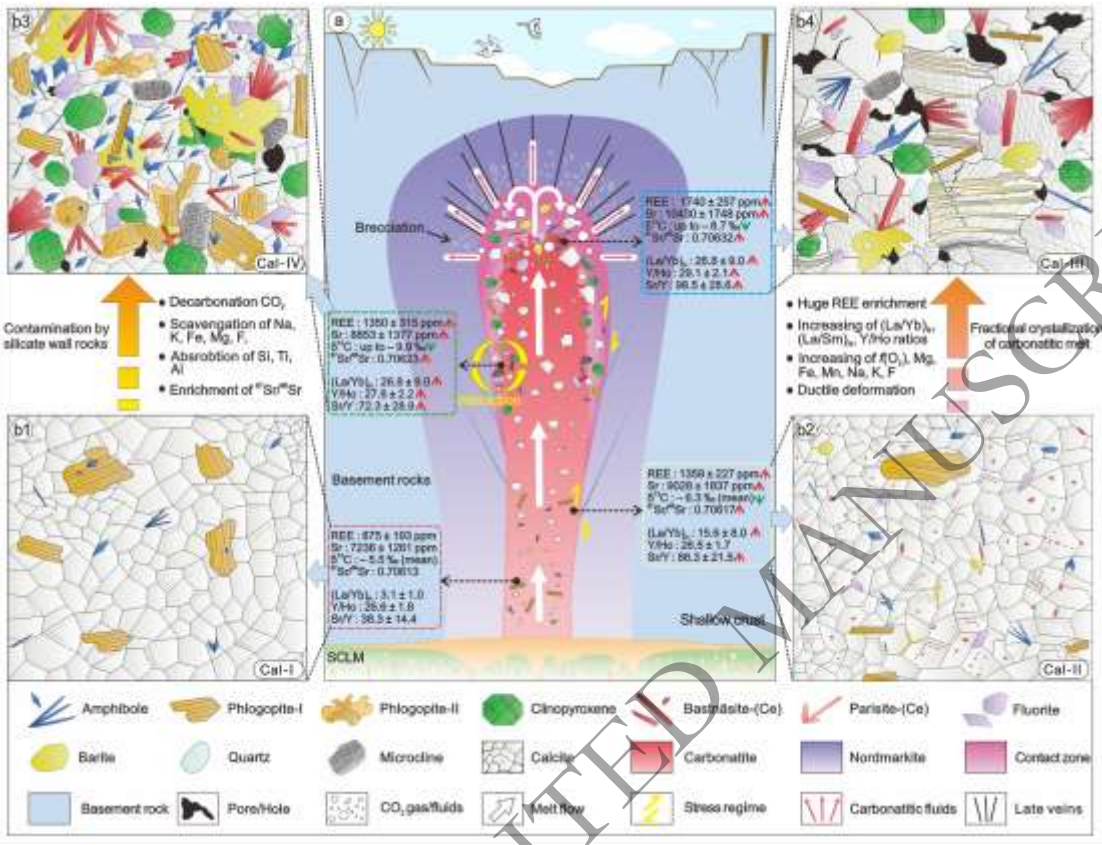

1933

1934

1935

1936

1937

1938